A HIGH RESOLUTION STUDY OF PROTON RESONANCES IN ^{65}Ga and ^{67}Ga

by

KENNETH BOYD SALES

A thesis submitted to the Graduate Faculty of
North Carolina State University at Raleigh
in partial fulfillment of the
requirements for the Degree of
Doctor of Philosophy

DEPARTMENT OF PHYSICS

RALEIGH

1 9 8 0

APPROVED BY:

_____ _____

_____ _____

Chairman of Advisory Committee

ABSTRACT

SALES, KENNETH BOYD. A High Resolution Study of Proton Resonances in ^{65}Ga and ^{67}Ga. (Under the direction of Gary E. Mitchell.)

Differential cross sections were measured for ^{64}Zn(p,p) from 2.50 to 3.24 MeV and for ^{66}Zn(p,p) from 2.60 to 3.26 MeV at laboratory angles of 90°, 105°, 135°, and 160°. These experiments were performed with the Triangle Universities Nuclear Laboratory 3 MV Van de Graaff accelerator and associated electrostatic analyzer-homogenizer system. The total overall energy resolution was 420 to 525 eV for ^{64}Zn(p,p) and 360 to 405 eV for ^{66}Zn(p,p).

Resonances observed in the excitation functions were analyzed with a multilevel R-Matrix formalism. Resonance energies, spins, parities, and elastic widths were extracted for 39 resonances in ^{65}Ga and 148 resonances in ^{67}Ga.

The l=0 proton strength functions were calculated for ^{64}Zn and ^{66}Zn. The s-wave strength function shows an increase for A=66, which is consistent with earlier results from (p,n) cross section studies.

Statistical properties of the 1/2+ resonances in ^{65}Ga and ^{67}Ga were examined. The spacing and reduced width distributions were compared with the Wigner and Porter-

Thomas distributions, respectively. This comparison indicates that 50% of the 1/2+ resonances were missed in ^{65}Ga and that 70% of the 1/2+ resonances were missed in ^{67}Ga. The observed s-wave level densities in ^{65}Ga and ^{67}Ga are compared with predictions from conventional level density models.

The analogs of the 0.867 MeV, the 0.910 MeV, and the 1.370 MeV states of ^{65}Zn are observed in ^{65}Ga; the analogs of the 0.093 MeV and the 0.394 MeV states of ^{67}Zn are observed in ^{67}Ga. The analog states in ^{65}Ga were fragmented into only two or three resonances, while the two analog states in ^{67}Ga were highly fragmented. Fits to the fine structure distributions of these two analogs were obtained and the resulting parameters compared with the Robson model. Coulomb energies were extracted for these five analogs. The spectroscopic factors were calculated for each analog and compared with the parent state spectroscopic factors obtained in (d,p) studies. Most of the values obtained in the direct reaction measurements were approximately a factor of two larger than those from the present analog studies.

BIOGRAPHY

KENNETH BOYD SALES

Personal: Born June 24, 1953, Burlington, North Carolina

Education: B.S. in Physics, North Carolina State University, Raleigh, North Carolina, 1975

Positions: Teaching Assistant, N.C.S.U., 1975 to 1977

Research Assistant, N.C.S.U., 1977 to present

Membership: Society of Physics Students

Sigma Pi Sigma

Phi Kappa Phi

Phi Eta Sigma

ACKNOWLEDGEMENTS

I would like to express my appreciation to my advisor, Dr. G. E. Mitchell for his guidance and support and for his time and understanding during all phases of this research project. The support of the other members of my committee, Drs. E. E. Burniston, A. W. Jenkins, and D. R. Tilley is also appreciated. Sincere appreciation is also extended to Dr. F. G. Bilpuch for his support during the course of these experiments and to Dr. N. R. Roberson for his support and advice.

I owe special thanks to C. R. Westerfeldt for his invaluable assistance and unfailing support in all phases of these experiments. I am also grateful to B. H. Choo for her continual help and support. The assistance of Dr. J. R. Chandler, R. O. Nelson, W. A. Watson, and K. M. Whatley in taking portions of these data is appreciated.

The assistance of Mr. S. E. Edwards, Mr. R. Rummel, and Mr. A. W. Lovette in maintaining the equipment used in these experiments is appreciated. I owe special thanks to Mrs. Joseph Bailey for her careful preparation of the figures in this dissertation.

I would like to express my deepest appreciation to my parents for their unfailing support and encouragement throughout my life.

This work was supported in part by the United States Department of Energy. Some of the data analysis was

performed at Triangle Universities Computation Center, which is supported in part by the National Science Foundation.

Table of Contents

LIST OF FIGURES vii

LIST OF TABLES x

1. INTRODUCTION 1

2. EXPERIMENTAL EQUIPMENT AND PROCEDURES 8

2.1 3 MV Van de Graaff System 8
2.2 Scattering Chamber 17
2.3 Electronics and Computer 27
2.4 Targets 32

3. PRELIMINARY ANALYSIS AND DATA PRESENTATION . . . 35

3.1 Data Reduction 35
3.2 Preliminary Analysis 37
3.3 Presentation and Discussion of Data 42
3.4 R-Matrix Theory 58

4. ANALYSIS AND DISCUSSION OF RESULTS 61

4.1 Strength Functions 61
4.2 Spacing Distributions 76
4.3 Reduced Width Distributions 100
4.4 Level Densities 121
4.5 Analog States 125
4.5.1 Theory of Analog States 125
4.5.2 Identification of Analog States . . . 131
4.5.3 Coulomb Energies 137
4.5.4 Spectroscopic Factors 139
4.5.5 Fine Structure Distributions 144

5. SUMMARY 151

6. APPENDIX 153

6.1 Resonance Parameters 153
6.2 Glow Discharge System 164

7. BIBLIOGRAPHY 171

LIST OF FIGURES

		Page
2.1	Floor Plan of the 3 MV Van de Graaff Accelerator Laboratory	10
2.2	Block Diagram of the Present Electrostatic Analyzer-Homogenizer Circuitry	13
2.3	Proton Spectrum for ^{66}Zn(p,p) at 3.221 MeV	20
2.4	Detector Collimation System for 105°	22
2.5	Top View of the Proton Scattering Chamber and Last Collimator Assembly	25
2.6	Block Diagram of Data Acquisition Electronics	29
3.1	The ^{64}Zn(p,p)^{64}Zn Differential Cross Section from 3.10 to 3.24 MeV for Four Angles	44
3.2	The ^{64}Zn(p,p) Differential Cross Section from 2.50 to 2.88 MeV for 160°	47
3.3	The ^{64}Zn(p,p) Differential Cross Section from 2.88 to 3.24 MeV for 160°	49
3.4	The ^{66}Zn(p,p)^{66}Zn Differential Cross Section from 3.06 to 3.20 MeV for Four Angles	52
3.5	The ^{66}Zn(p,p) Differential Cross Section from 2.60 to 2.94 MeV for 160°	55
3.6	The ^{66}Zn(p,p) Differential Cross Section from 2.94 to 3.26 MeV for 160°	57
4.1	The s-wave Strength Function for Masses between A=25 and 70	65
4.2	Differential and Integral Plots of the 1/2$^+$ Reduced Widths in ^{65}Ga	69

4.3 Differential and Integral Plots of the 1/2+ Reduced Widths in ^{67}Ga 71

4.4 Cumulative Sum of the Number of Resonances in ^{65}Ga and ^{67}Ga 73

4.5 Spacing Distribution for ^{65}Ga 79

4.6 Uncorrected Spacing Distribution for ^{67}Ga 82

4.7 Corrected Spacing Distribution for ^{67}Ga 84

4.8 Uncorrected and Corrected Spacing Distributions for the Upper 51 Resonances in ^{67}Ga 86

4.9 Simulation of the Effects of Missing 0% to 15% of the Resonances on the Wigner Distribution 90

4.10 Simulation of the Effects of Missing 20% to 35% of the Resonances on the Wigner Distribution 92

4.11 Simulation of the Effects of Missing 40% to 55% of the Resonances on the Wigner Distribution 94

4.12 Simulation of the Effects of Missing 60% to 75% of the Resonances on the Wigner Distribution 96

4.13 Simulation of the Effects of Missing 80% to 95% of the Resonances on the Wigner Distribution 98

4.14 Reduced Width Distribution for ^{65}Ga 102

4.15 Reduced Width Distribution for ^{67}Ga 105

4.16 Reduced Width Distribution for the Upper 51 1/2+ Resonances in ^{67}Ga 107

4.17 Simulation of the Effects of Missing 0% to 15% of the Resonances on the Porter-Thomas Distribution 110

4.18 Simulation of the Effects of Missing 20% to 35% of the Resonances on the

Porter-Thomas Distribution 112

4.19 Simulation of the Effects of Missing 40% to 55% of the Resonances on the Porter-Thomas Distribution 114

4.20 Simulation of the Effects of Missing 60% to 75% of the Resonances on the Porter-Thomas Distribution 116

4.21 Simulation of the Effects of Missing 80% to 95% of the Resonances on the Porter-Thomas Distribution 118

4.22 Energy Level Diagram Showing the Relationship Between the Analog State and the Parent State 128

4.23 The ^{65}Zn - ^{65}Ga Isobaric Pair 133

4.24 The ^{67}Zn - ^{67}Ga Isobaric Pair 136

4.25 Theoretical Fit to the Fine Structure Distribution of the $3/2^-$ Analog State at 3.1452 MeV in ^{67}Ga 146

4.26 Theoretical Fit to the Fine Structure Distribution of the $1/2^-$ Analog State at 2.8280 MeV in ^{67}Ga 149

6.1 Schematic of Glow Discharge System 168

LIST OF TABLES

Page

4.1 1/2+ Level Densities for ^{65}Ga and ^{67}Ga 122

4.2 Coulomb Energy Differences 138

4.3 Spectroscopic Factors 142

4.4 Single Particle Widths 143

6.1 ^{65}Ga Resonance Parameters 154

6.2 ^{67}Ga Resonance Parameters 156

Chapter 1

Introduction

Resonance reactions have proven a powerful tool for studying nuclear forces and interactions. In 1935, Bethe outlined the single particle model in which the incident particle is assumed to move in an average attractive real potential with no interactions between the incident particle and the individual nucleons of the nucleus. This model predicted broad, widely spaced resonances. However, in 1936 these predictions were contradicted by the experimental evidence. Narrow resonances were measured in the neutron cross section on a variety of targets, instead of the expected broad and widely spaced resonances. To explain these narrow resonances Bohr (1936) formulated the compound nucleus model. In this model, the incident neutron interacts strongly with the nucleus and therefore quickly shares its energy with the individual nucleons. This compound nuclear system is so complicated that a large number of collisions and energy exchanges occur before a single nucleon can acquire sufficent energy to escape from the nucleus. The time required for a single nucleon to escape from the nucleus is several orders of

magnitude longer then the nuclear transit time. By the uncertainty principle a long lifetime implies a narrow width. In this model, if the incident projectile penetrates the nucleus, then the compound nucleus is always formed.

The discovery of "giant" or "size" resonances in the neutron cross section (Barshall, 1952, Miller et al., 1952) similar to those resonances predicted by the single particle model demonstrated the necessity for an intermediate model. (In nuclear physics, the term "giant resonance" is used to refer to many different phenomena. In this dissertation, giant resonance refers to a single particle resonance.) Feshbach, Porter, and Weisskopf (1954) postulated a model with a real three-dimensional potential to describe the broad resonances and with an imaginary potential to describe the absorption effects. This model is called the optical model since the complex potential is analogous to a complex optical index of refraction. The optical model predicts that a single particle state will be spread into a giant resonance with its width proportional to the imaginary part of the potential. This model predicts only average behavior or gross structure and does not describe the observed sharp or "fine-structure" resonances.

In 1955, Lane, Thomas, and Wigner explained the fragmentation of giant resonances into fine structure

resonances in terms of the intermediate coupling model. In this model, the residual interaction (the difference between the actual Hamiltonian of the system and a pure single particle Hamiltonian) mixes the "strength" of the single particle state with other nuclear states of the same spin and parity. This phenomemon is referred to as "line broadening"; the single particle state is observed experimentally as many fine structure states. The intermediate model also predicts that the distribution of the strengths will be Lorentzian about the original single particle energy. In other words, the strengths exhibit resonance behavior at the single particle energies. This resonance behavior will be reflected in the strength function, $S = \langle\gamma^2\rangle/\langle D\rangle$, where γ^2 is the reduced width (or strength) of a resonance (see Section 3.4), $\langle\gamma^2\rangle$ is the average reduced width over a finite energy range, and $\langle D\rangle$ is the average level spacing. One of the main objectives of the experiments described in this dissertation was to measure the s-wave strength function for A=64 and A=66. From measurements on the (p,n) reaction cross section, the peak of the 3s giant resonance is expected to be located near A=70.

While the intermediate model does predict the resonance behavior at single particle energies, the model does not predict the fluctuations of the reduced widths about the Lorentzian distribution. The intermediate model

accounts for the average behavior of nuclear interactions but cannot describe individual compound nuclear states. Therefore, statistical theories are used to describe the behavior of the compound nuclear states. In 1956, Porter and Thomas postulated that the reduced widths for a single channel should obey a chi-squared distribution of one degree of freedom. This distribution describes the fluctuations of the reduced widths about the Lorentzian distribution of the single particle strength. Another property of compound nuclear states which should obey a statistical distribution is the level spacing. In 1956, Wigner obtained a theoretical form for the nearest neighbor spacing distribution. The distribution is linear for small spacings, reaches a maximum near the average level spacing, and then decreases very rapidly for larger spacings. The reduced width and spacing distributions are discussed in Sections 4.2 and 4.3, respectively.

An additional aspect of line broadening is the phenomenon of isobaric analog states. Analog states were discovered through the (p,n) reaction by Anderson and Wong(1961) and were discovered in the compound nucleus by Fox, Moore, and Robson (1964) through proton elastic scattering and the (p,n) reaction on ^{88}Sr and ^{89}Yr. The excited states in the compound nucleus were identified as analogs of low-lying states of ^{89}Sr and ^{90}Yr, respectively. In 1964, Richard et al. partially resolved

the fine structure of an analog state in ^{93}Tc. The fine structure distribution was first explained by Robson (1965) as the result of the mixing of the analog strength through the Coulomb interaction with the ordinary background states of the same spin and parity. This spreading of the analog strength has some similarities to the spreading of the single particle resonances. However, the mixing of the analog state with the background states is much weaker than is the mixing of the single particle state, since the Coulomb force is much weaker than the nuclear force. The Robson theory also predicts that the distribution of the reduced widths of the fragmented analog state should be asymmetric, with the widths below the analog state enhanced more than the widths above the analog state.

The fine structure of an analog state was first resolved at Duke University by Keyworth and Bilpuch (1966) through proton elastic scattering on ^{40}Ar with the high resolution beam of the 3 MV Van de Graaff accelerator. Interest in analog states continued with a systematic program to study analog states in the mass region $40 \leq A \leq 70$ with proton elastic scattering. The excellent beam energy resolution of these experiments also allowed the study of statistical properties of the compound nucleus. With a high resolution proton beam, resonances were studied over a wide energy range and for different total

angular momentum values.

The experiments described in this dissertation are a continuation of this systematic study. The differential cross sections were measured for ^{64}Zn(p,p) from 2.50 to 3.24 MeV and for ^{66}Zn(p,p) from 2.60 to 3.26 MeV at laboratory angles of 90°, 105°, 135°, and 160° with the Triangle Universities Nuclear Laboratory (T.U.N.L.) 3 MV Van de Graaff accelerator and the associated analyzer-homogenizer system. Only the elastic channel was studied since the inelastic channel was strongly inhibited by the low penetrabilities due to the Coulomb barrier.

In Chapter two, a description is given of the experimental equipment and procedures. A description of the data reduction procedures and the data presentation is given in Chapter three. A short discussion of the R-Matrix theory which was used to extract the resonance parameters is also presented in Chapter three. Statistical and non-statistical properties of the resonance parameters are discussed in Chapter four. These statistical properties include the s-wave strength function, reduced width distributions, spacing distributions, and level densities. The remainder of Chapter four is devoted to a discussion of the analog states observed in these experiments. A summary of these experiments is given in Chapter five and the resonance parameters are listed in Appendix 6.1. A discussion of

the glow dischage method used in fabricating the ^{66}Zn targets is given in Appendix 6.2.

Chapter 2

EXPERIMENTAL EQUIPMENT AND PROCEDURES

2.1 3 MV Van de Graaff System

These experiments were performed with the high-resolution system on the 3 MV Van de Graaff accelerator at Triangle Universities Nuclear Laboratory.

A schematic of the accelerator and its associated analyzer-homogenizer system is shown in Figure 2.1. The r-f ion source in the terminal of the accelerator produces an H^+ and an HH^+ beam of ions. Upon emerging from the accelerator, the proton (H^+) beam is separated from the molecular (HH^+) beam by an analyzing magnet. The proton beam is steered into the scattering chamber and used to perform the experiments. The molecular beam passes through the corona control slits and then into an electrostatic analyzer. A correction signal obtained from the difference in current between the corona slits is amplified by the corona control circuitry and applied to the terminal of the accelerator. Due to the insulating gas between the tank and terminal, there is a finite drift

Figure 2.1 Floor Plan of the 3 MV Van de Graaff Accelerator Laboratory.

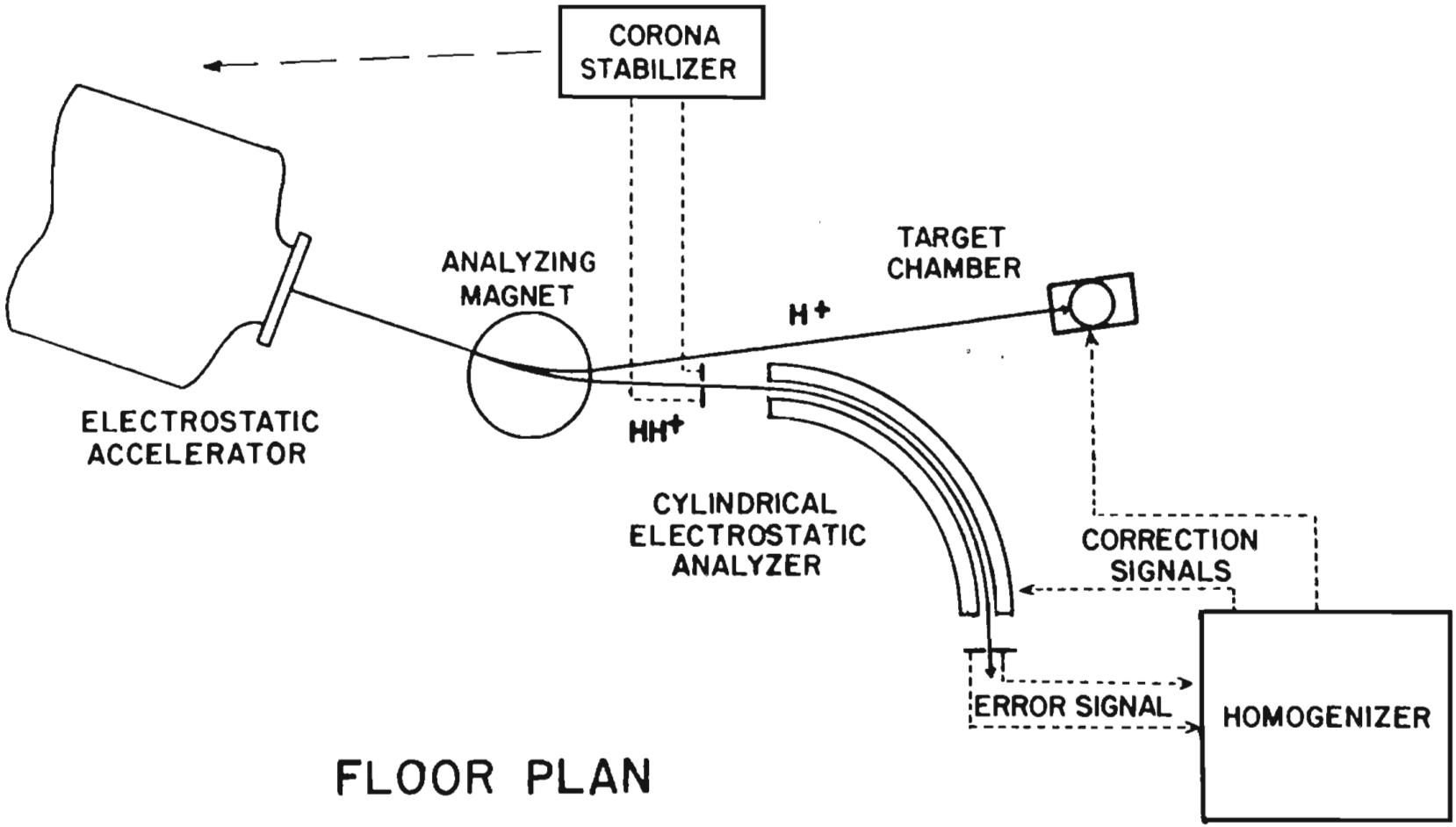
CORONA
STABILIZER
ANALYZING
MAGNET
TARGET
CHAMBER
H+
ELECTROSTATIC
ACCELERATOR
HH+
CYLINDRICAL
ELECTROSTATIC
ANALYZER
CORRECTION
SIGNALS
ERROR SIGNAL
HOMOGENIZER

FLOOR PLAN

time for the corona current traveling from the corona needles to the dome of the terminal. This finite drift time and the large capacitance between the dome and the tank allows only very low frequency fluctuations to be removed from the terminal voltage. The high frequency cutoff of the corona control system is around 10 Hz. Therefore, in order to remove higher frequency fluctuations, a correction signal is applied to the target. This correction is performed by the analyzer-homogenizer system.

The analyzer-homogenizer system is shown schematically in Figure 2.2. The electrostatic analyzer consists of two concentric quarter-circle plates with a mean radius of one meter. The separation between the plates is 0.19". A very well regulated negative voltage is applied to the inner plate to steer the beam through the analyzer. This voltage is supplied by a r-f power supply recently acquired from Bertan Associates, Inc. The r-f power supply was purchased since the previous inner plate power suppy was unreliable and difficult to maintain. Only recently have advances in r-f power supply technology enabled the development of a r-f power supply with the necessary output voltage and current for use as the inner plate power supply.

Should the inner plate supply drift, a signal is obtained from a precision resistance stack connected

Figure 2.2 Block Diagram of the Present Electrostatic Analyzer-Homogenizer Circuitry.

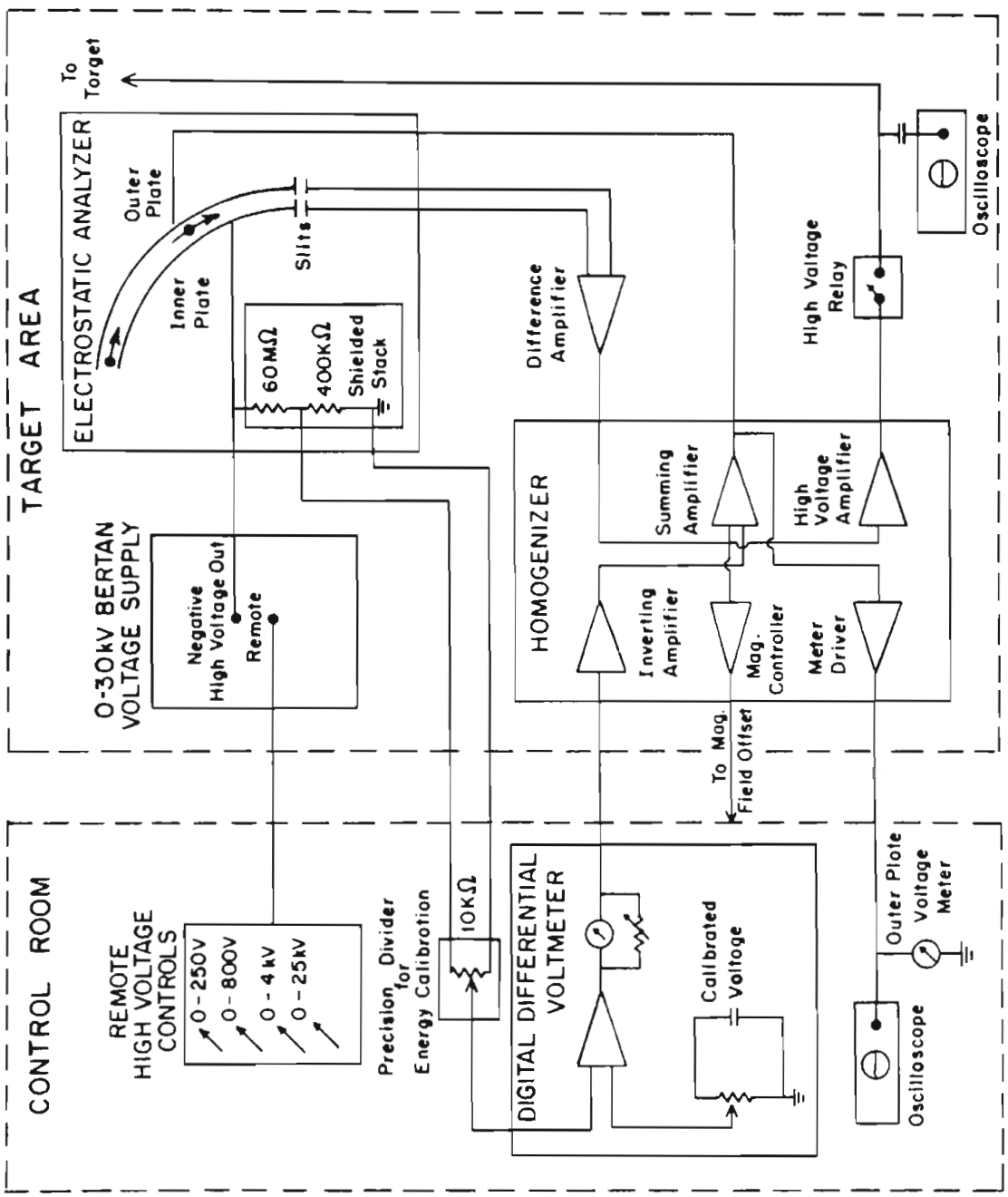
TARGET AREA
ELECTROSTATIC ANALYZER
To Target
Outer Plate
Inner Plate
Slits
60MΩ
400KΩ
Shielded Stack
Difference Amplifier
High Voltage Relay
Oscilloscope
0-30kV BERTAN VOLTAGE SUPPLY
Negative High Voltage Out
Remote
HOMOGENIZER
Summing Amplifier
High Voltage Amplifier
Inverting Amplifier
Mag. Controller
Meter Driver
To Mag. Field Offset
CONTROL ROOM
REMOTE HIGH VOLTAGE CONTROLS
0-250V
0-800V
0-4kV
0-25kV
Precision Divider for Energy Calibration
10KΩ
DIGITAL DIFFERENTIAL VOLTMETER
Calibrated Voltage
Outer Plate Voltage Meter
Oscilloscope

between the inner plate power supply and ground. This signal is sent to the input of a differential voltmeter (DVM). The DVM compares the voltage from the resistance stack to the reference voltage set on the DVM. Any difference in voltage is sent to the homogenizer. The homogenizer then applies a voltage to the outer plate to counteract the drift in the inner plate voltage. Therefore, if the inner plate power supply drifts and steers the molecular beam from center on the analyzer slits, a outer plate voltage is automatically applied in order to recenter the beam.

The energy fluctuations common to the proton beam and molecular beam are transformed into position fluctuations on the output analyzer slits by the electrostatic analyzer. The signals from these slits are fed into a Princeton Applied Research (PAR) Model 113 difference amplifier. The difference signal from the PAR is then sent to the homogenizer. The homogenizer sums the PAR difference signal with the inverted output of the DVM. This summed signal is amplified and sent to the outer plate to recenter the beam. The summed signal also goes to a high voltage amplifier and then is sent to the target rod. The high voltage amplifier DC bias is +4 kV with a output swing of ±3 kV.

If the beam emerging from the accelerator increases in energy, a difference signal is obtained by the PAR.

This signal is then used by the homogenizer to recenter the beam on the output analyzer slits. In addition, the target rod bias is increased in order to maintain a constant reaction energy. Similarly, if the beam from the accelerator decreases in energy, the target rod bias is decreased. The feedback electronics of the homogenizer system was recently redesigned and rebuilt by Wells (1978), resulting in greater reliablity and simplified operation.

However, it is very difficult or impossible to directly measure the energy resolution of the proton beam with the present system. The experimental resolution function is determined by many factors: the remaining energy spread of the proton beam after correction, energy straggling due to the finite target thickness, and energy spread from the Doppler effect due to motion of the target nuclei. The experimental resolution function is the sum in quadrature of all of these factors, and is therefore only a upper bound on the actual beam energy resolution. The width of the overall resolution function for the ^{64}Zn(p,p) experiment was between 420 and 525 eV (FWHM), and for the ^{66}Zn(p,p) experiment, the width of the resolution function was between 360 and 405 eV (FWHM). With an earlier version of this system, Keyworth (1968) was able to obtain 110 eV resolution using a cryogenically cooled gas target, which indicates that these additional

factors (other than the beam energy resolution) are very significant.

At the present time, an energy correction system similar to the system installed by Block et al. (1967) is being designed and built. This system should allow the beam energy resolution to be determined more directly and may result in better energy resolution. The correction signal will be sent to the terminal of the accelerator instead of applying a correction signal to the target rod. The signal will first drive a light emitting diode (LED) at the base of the accelerator and then be transmitted to a photomultiplier tube in the terminal by several strands of Crofon, which is a fiber optics material manufactured by DuPont. The signal from the photomultiplier tube will be amplified by a high voltage amplifier and the signal will be applied between the r-f ion source and the dome of the terminal. Since the energy correction will be performed at the terminal of the accelerator, the difference signal from the output analyzer slits will be proportional to the beam energy resolution. This system will be installed and tested in the near future.

2.2 Scattering Chamber

The charged particle scattering chamber used in these experiments was originally designed by Browne (1969). The detector collimators and the last collimator assembly were recently redesigned in order to reduce the point scatter in the experimental data. The vacuum in the scattering chamber was maintained at better than 10^{-6} Torr, in order to reduce target deterioration due to the build up of silicon and carbon deposits from pump oil vapors present in the vacuum system.

Elastically scattered protons were detected by Ortec surface barrier detectors located at laboratory angles of 90°, 105°, 135°, and 160°. The detectors were biased at approximately 100 volts to provide a depletion depth necessary to stop a 3.3 MeV proton. The detector resolution was between 15 and 20 keV. This resolution is necessary to distinguish the zinc peak from any contaminant peaks. For the ^{64}Zn(p,p) experiment, there were no contaminant peaks near the ^{64}Zn peak. However, in the ^{66}Zn(p,p) experiment, a tantalum contaminant was near the ^{66}Zn peak. The tantalum contaminant was only observed in the ^{66}Zn experiment since different methods were used

to fabricate the ^{64}Zn and ^{66}Zn targets. A typical elastic spectrum of $^{66}Zn(p,p)$ is shown in Figure 2.3. The tantalum contaminant and the ^{66}Zn peaks were resolved at angles 135° and 160°, but not at angles 90° and 105°. The procedure used to subtract the contaminant peak at 90° and 105° is discussed in Section 3.1.

The detector collimators were redesigned in order to minimize the effects of the beam movement over a non-uniform target. The geometry of the new detector collimators can be understood by examining a side view of the detector collimators and of the target. This side view is shown schematically in Figure 2.4. L2 is the distance from the beam spot on the target to the first collimator, while L1 is the distance between the first and second collimators. D1 and D2 are the diameters of the first and second collimators, and D3 is the diameter of the beam spot. As can be seen from the side view of the detector collimators, the diameters (D1, D2, and D3) and the lengths (L1 and L2) were chosen to form a trapezoid. These dimensions are related by,

$$L2 = L1 * (D1 - D3)/(D1 - D2)$$

where the derivation of this equation requires only plane geometry and trigonometry.

In previous experiments, the detector collimator

Figure 2.3 Proton Spectrum for $^{66}Zn(p,p)$ at 3.221 MeV. The ^{12}C peak has been gated out of the spectrum although its relative position is shown. The solid line is a guide to the eye.

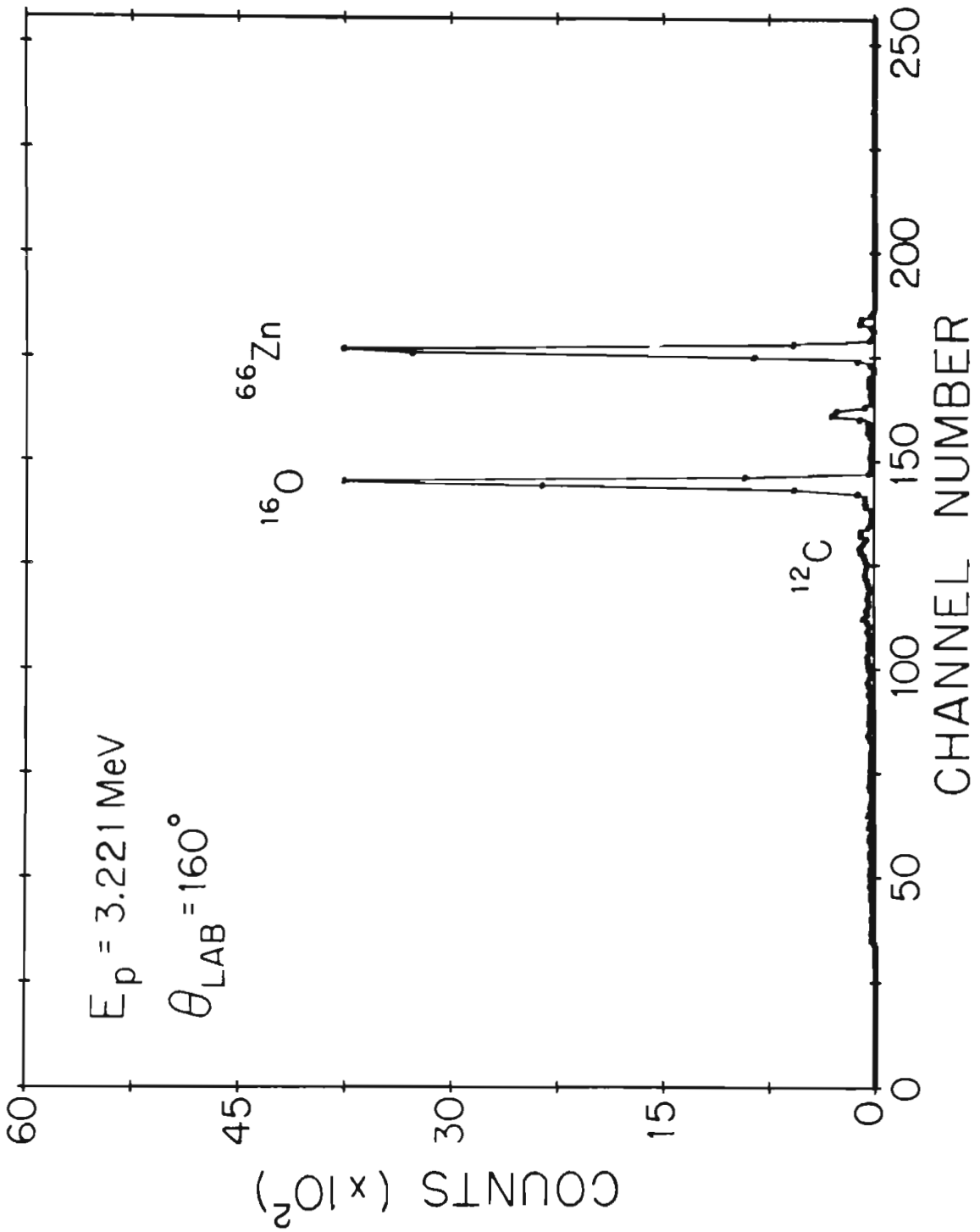
E_p = 3.221 MeV
θ_{LAB} = 160°
^{66}Zn
^{16}O
^{12}C
COUNTS (x 10^2)
CHANNEL NUMBER
0
15
30
45
60
0
50
100
150
200
250

Figure 2.4 Detector Collimation System for 105°.

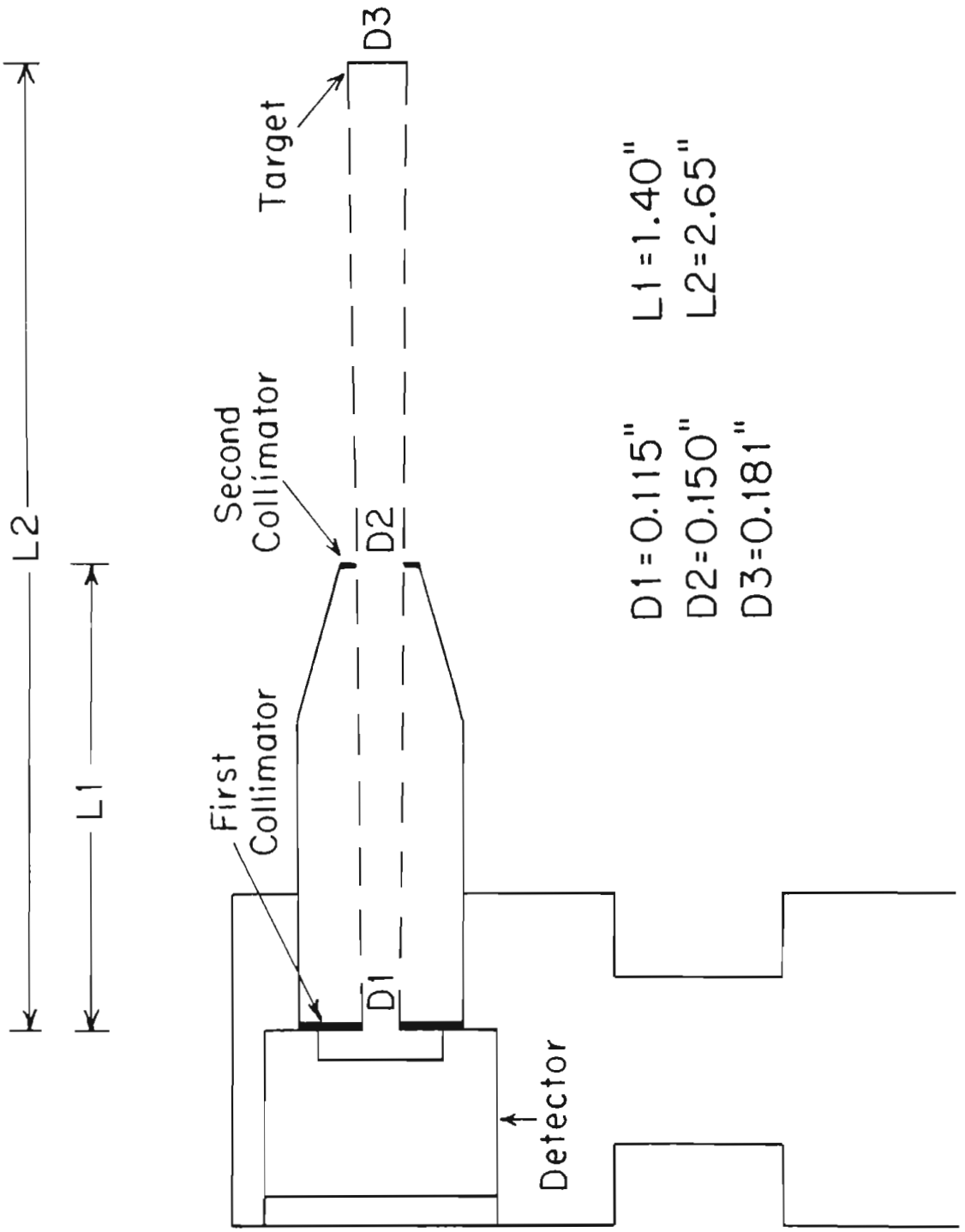
L2
L1
First Collimator
Second Collimator
Target
D1
D2
D3
Detector
D1=0.115"
D2=0.150"
D3=0.181"
L1=1.40"
L2=2.65"

geometry was such that any movement of the beam spot would result in a yield change in the spectra. The magnitude of this yield change is further enhanced if the targets are non-uniform. This change in the yield for different data points results in point scatter which obscures small resonances.

In practice, only the size of the first collimator D1 and the length L2 could be varied. The length L1 was fixed for all four detectors and the diameter D2 was as large as possible. The values for the collimator D1 and the length L2 for each detector were determined by arranging the four detectors such that their counting rates were approximately equal. This normalization to the Rutherford background was accomplished by moving the back angle detectors radially inward and the forward angle detector radially outward. However, the dimensions of the scattering chamber constrained the values for the length L2. A schematic of the scattering chamber and the last collimator assembly is shown in Figure 2.5. The 90° detector was moved radially outward as far as possible and the 135° and 160° detectors were moved radially inward as far as possible without intersecting the proton beam.

The collimators in the last collimator assembly were also redesigned. The first three collimators were changed from 0.0625" to 0.125" I.D. and the last collimator was changed from 0.0937" to 0.1875" I.D.. These changes were

Figure 2.5 Top View of the Proton Scattering Chamber and Last Collimator Assembly.

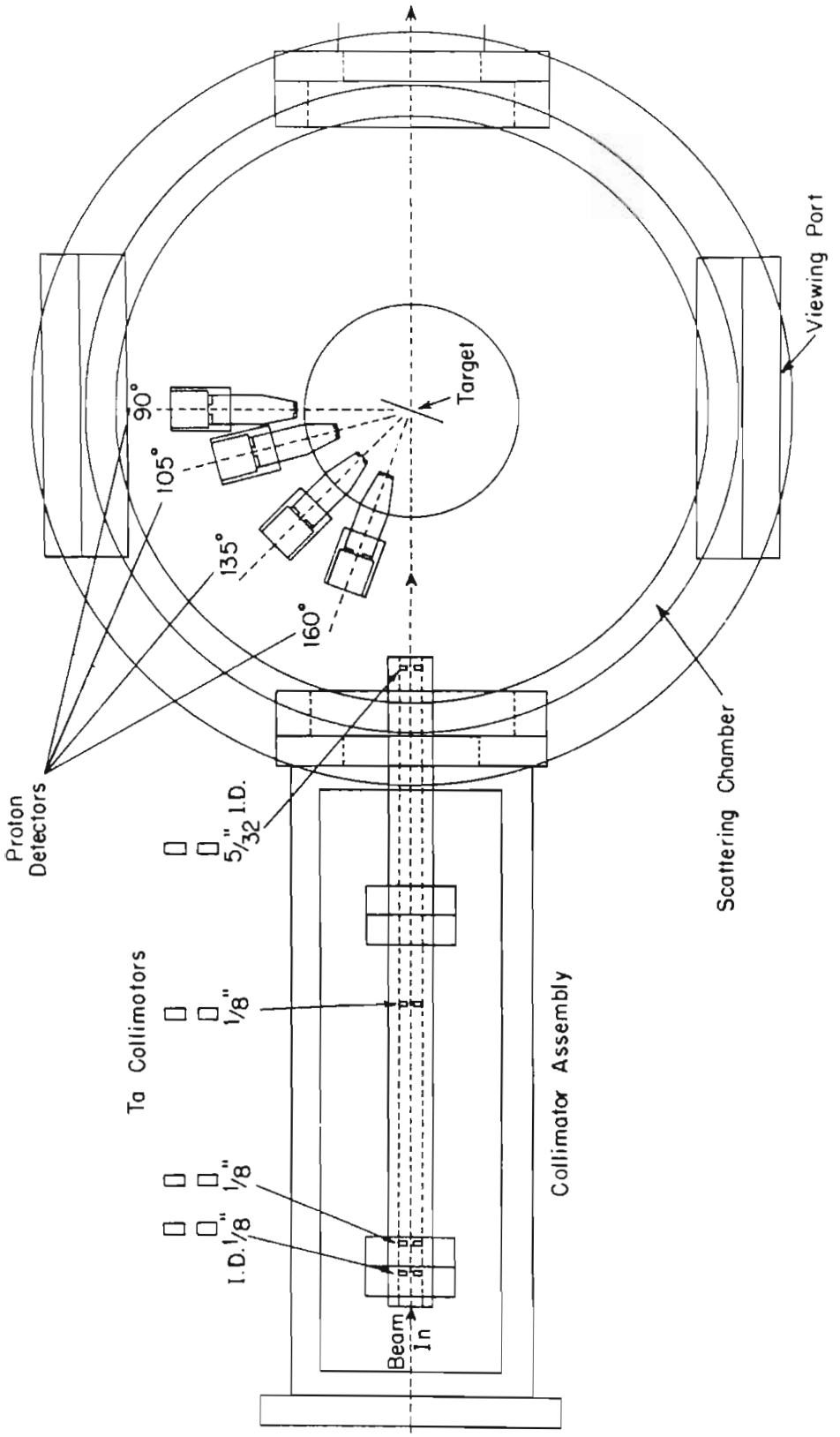
Viewing Port
Target
90°
105°
135°
160°
Proton Detectors
5/32" I.D.
Scattering Chamber
Ta Collimators
1/8"
Collimator Assembly
I.D. 1/8"
1/8"
Beam In

made in order to obtain a larger beam spot on the target.

The detector solid angles used in the ^{64}Zn(p,p) experiment were different from the solid angles employed in the ^{66}Zn(p,p) experiment, since the ^{64}Zn experiment was performed before these improvements were made to the scattering chamber and the last collimator assembly. The detector solid angles used in the ^{64}Zn(p,p) experiment were: 90° -- 1.37 milli steradians (msr), 105° -- 2.27 msr, 135° -- 3.08 msr, and 160° -- 4.44 msr. Similarly, the solid angles used in the ^{66}Zn(p,p) experiment were: 90° -- 0.98 msr, 105° -- 1.48 msr, 135° -- 2.43 msr, and 160° -- 2.75 msr.

In summary, both the changes to the detector collimators and to the collimator assembly were carried out to reduce the point scatter in the data. By increasing the diameter of the collimators in the last collimator assembly, a larger beam spot was obtained. This larger beam spot intersects the target over a area large enough to average out the non-uniformities in the target. Also, the detectors needed to "see" this bigger beam spot, which required the change in the detector collimator geometry.

2.3 Electronics and Computer

A block diagram of the data acquisition electronics is shown in Figure 2.6. The data for these experiments were taken at four different angles. Therefore, four different sets of the data acquisition electronics were needed, except for the computer and computer interface which were shared by the four systems.

When a proton is scattered from the target into a surface barrier detector, a small output voltage pulse is generated in the detector with the voltage pulse proportional to the energy of the scattered proton. This voltage pulse is sent to an Ortec model 109A preamplifier with a gain of 10. The signal from the preamplifier is sent to a (Tennelec 203) spectroscopy amplifier. The spectroscopy amplifier has one unipolar and one bipolar output signal. The unipolar signals from each spectroscopy amplifier are sent to a (Ortec 433) Dual Sum and Invert module. This summed linear signal is sent to a Northern Scientific (model 621) ADC (analog to digital converter). Each bipolar signal from the spectroscopy amplifier is sent to a (Ortec 420A) timing single channel analyzer (SCA). Also, the bipolar signal is sent through

Figure 2.6 Block Diagram of Data Acquisition Electronics.

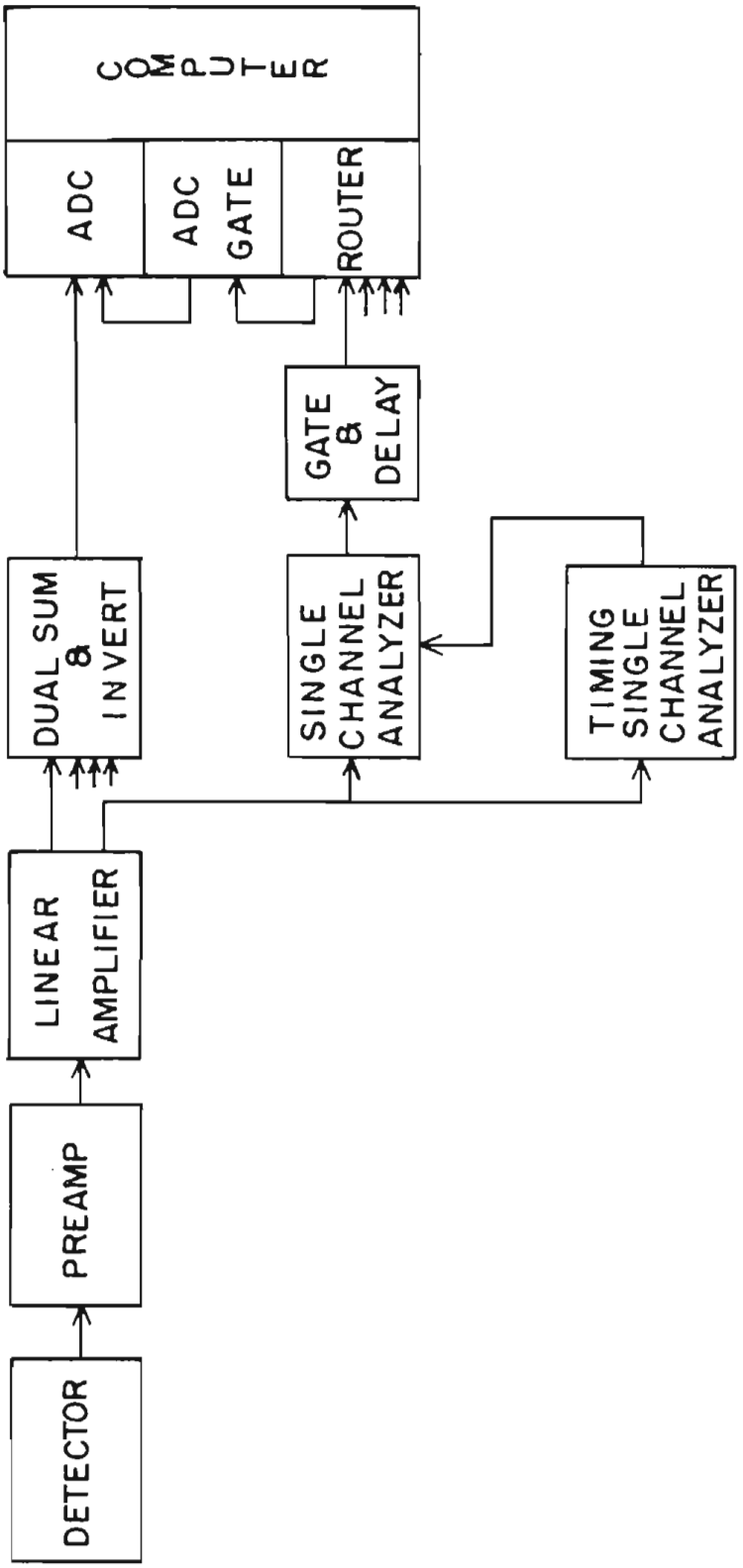
COMPUTER
ADC
ADC GATE
ROUTER
GATE & DELAY
DUAL SUM & INVERT
SINGLE CHANNEL ANALYZER
TIMING SINGLE CHANNEL ANALYZER
LINEAR AMPLIFIER
PREAMP
DETECTOR

a delay line of 0.7 μs and then into a (Hewlett Packard 588A) single channel analyzer. The timing SCA is used to set an electronic window around the carbon pulses. The Hewlett Packard SCA uses the output from the timing SCA to gate out the carbon pulses. The carbon pulses are gated out in order to decrease the dead time of the data acquisition system. The output from the Hewlett Packard SCA is sent to an (Ortec 416A) gate and delay generator which shapes and delays the signal. The output of the gate and delay generator is sent to one of the inputs of an eight input router. By using this method of gating out the carbon pulses, a router signal is never sent to the computer for the carbon pulses.

The router functions as a decimal to binary decoder by constructing a four bit word corresponding to which input received a signal. The router also outputs a gate and a busy signal. The router gate is used by the ADC to gate on the linear signal from the Dual Sum and Invert. When the ADC receives the router gate, it digitizes the linear signal into a 12 bit word. The 4 bit router word and 12 bit ADC word are sent to a Bi Ra model 2322 dual input register. The input register resides in a slot in a CAMAC crate. CAMAC is a standardized instrumentation system developed by the ESONE committee of European laboratories. The input register sends the data and router information to a Bi Ra model 1310 type A-1 crate

controller located in the CAMAC crate. The crate controller sends the information to a Bi Ra model 1260 branch driver. The branch driver interrupts the Prime 300 computer which stores the information in a data matrix in memory. The data matrix is written onto magnetic tape at the end of each counting time. The computer software and hardware for this system is described in greater detail by Chandler (1978). This system has been very reliable and easy to use for on-line data acquisition and for off-line data analysis.

The counting time for each data point was controlled by a Ortec model 439 current digitizer. The function of the current digitizer was to digitize the beam current collected by a Faraday cup after the beam had interacted with the target. The output from the current digitizer was sent to a preset scalar which was preset for between 100 to 400 μC. The router busy signal was used to gate the current digitizer on or off in order to correct for the system dead time.

2.4 Targets

The fabrication of the targets proved to be the major obstacle in the execution of these experiments. In order to overcome this obstacle, three different methods of target preparation were tried. The first method involved evaporating the zinc isotope onto 5 $\mu g/cm^2$ carbon foils, which were mounted on standard target rings. Unfortunately, the zinc would not condense onto the carbon backing. Instead, the zinc would condense onto the bell jar and any other cool surface. Due to this failure, other methods were used to prepare the targets. For the $^{64}Zn(p,p)$ experiment, the target backings were cooled to approximately the temperature of liquid nitrogen (77° K) before evaporation. For the $^{66}Zn(p,p)$ experiment, the target backings were cleaned by a glow-discharge before the evaporation of the isotope. Although more difficult to use, the glow-discharge method proved more sucessful for fabricating the zinc targets. A detailed discussion of the glow-discharge method is presented in Appendix 6.2.

The carbon backings for the $^{64}Zn(p,p)$ experiment were cooled by placing a heat sink in contact with the glass slide holding the carbon backing. The heat sink was a

block of aluminum which had been placed in a dewar of liquid nitrogen. The aluminum block was removed from the dewar and quickly placed on top of the glass slide. A vacuum was then obtained as quickly as possible in the evaporator. As soon as an acceptable vacuum was reached, the zinc isotope was evaporated onto the carbon foils. In this case the zinc isotope condensed very easily onto the cold carbon backings. However, when the zinc targets were placed in the path of the proton beam, the targets evaporated due to the heat dissipated by the proton beam. The zinc also migrated into the carbon backings, which caused a deterioration of the energy resolution due to increased straggling.

Targets which were prepared with the glow-discharge system also evaporated when placed in the proton beam, but at a much slower rate. With these targets much better energy resolution was achieved. A possible explanation for the better energy resolution is that since the carbon backings were clean, the zinc isotope made a stronger bond to the carbon. This stronger bond may have reduced the amount of migration into the carbon backing and therefore reduced the effects of energy straggling.

In all three methods, the ZnO compound was first chemically reduced to release the oxygen and leave only the zinc for evaporation. Tantalum powder was used as the reducing agent. The ZnO and tantalum powder were mixed

together and placed inside a tantalum boat. The boat was made from 0.25" O.D. tantalum tubing and was approximately 2" long. The ends of the boat were tightly crimped to prevent the loss of the target material. The crimped ends were also used to connect the boat to the high current evaporator leads. A 0.0625" hole was drilled into the middle of the boat in order to obtain an approximate point source for the evaporation.

The enriched isotopes were obtained from Oak Ridge National Laboratory in the chemical form ZnO. The isotopic enrichment for ^{64}Zn was 99.66% and for ^{66}Zn, 98.80%. The thickness of the zinc on the targets was typically 1.5 - 2.5 $\mu g/cm^2$. This thickness was a compromise value since thicker targets lead to increased counting rates, but also to increased energy straggling and worse energy resolution.

Chapter 3

Preliminary Analysis and Data Presentation

3.1 Data Reduction

Data from these experiments were processed in three different stages. In the first stage, a yield curve generating program was used to obtain the unnormalized excitation function for all four angles. This program reads the spectra for all four angles from a data tape and then sums the area under each zinc peak. The program also provides different methods of background subtraction for each angle. These areas, along with the corresponding energy of the incident proton, are stored in computer memory. After all the spectra have been processed, this yield curve information is first stored on magnetic tape, and later transferred to computer cards for further analysis.

In the ^{64}Zn(p,p) experiment the areas were summed without any background correction to the spectra.

Instead, the background correction was made in the third stage of the preliminary analysis.

For the $^{66}Zn(p,p)$ experiment, a recently rewritten version of this code on the Prime 300 computer was used. A background correction was needed only for the tantalum contaminant (see Section 2.2). Since the tantalum contaminant and the ^{66}Zn peaks were resolved at angles 135° and 160° but not at angles 90° and 105°, the following procedure was used to subtract the contaminant peak at 90° and 105°. First, the yield curve for the tantalum peak was generated for 135° and 160° over a short energy range for each target used in the experiment. Next, the background corrections were calculated for 90° and 105° taking into account the differences in yield for each angle due to Rutherford scattering, and the differences in solid angle between the different angles. Finally, these background corrections were subtracted from 90° and 105°.

3.2 Preliminary Analysis

In the second stage of the analysis, preliminary values for the resonance energy, laboratory width, and angular momentum and parity of the resonances were obtained. The program (MULT-EYE) was used to obtain these initial fits. This program uses the theory and notation of Blatt and Biedenharn (1952).

For the ^{66}Zn experiment, this program was recently implemented on the Prime 300 computer. This program calculates the proton elastic cross section as a function of incident proton energy, and can handle a maximum of 250 resonances and total angular momentum values up to 9/2. The calculated cross section was averaged with a Gaussian resolution function, with an optional Lorentzian on the low energy side to reproduce the effects of straggling in the target. An exponential decay in the target thickness may be corrected by renormalizing the yield curve. In practice, the preliminary fits using the newer version of MULT-EYE were of excellent quality and considerably reduced the amount of effort in the third stage of the analysis. The most important aspect of this program is that it is interactive. The user is able to change many different parameters and see the results very quickly. The computation time required by MULT-EYE to fit a single

resonance is only a few seconds with the time increasing to approximately 30 seconds for simultaneously fitting several resonances. In all cases, contributions from resonances far away in energy are included.

The earlier version of MULT-EYE used to fit the ^{64}Zn(p,p) data was not as successful in providing good fits to the data. The primary reason for these difficulties was the inaccurate function used to average the data. The symmetric resolution function used to average the data neglected the effects of straggling. With this resolution function only approximate resonance energies and total angular momentum values were obtained, with the laboratory widths particularly uncertain. As a result much more extensive analysis was performed in the third stage than in the analysis of the ^{66}Zn(p,p) data.

In the third and final stage of the preliminary analysis, final fits to the data were obtained with a multi-level, multi-channel computer program (MULTI) based on the R-Matrix theory of Lane and Thomas (1958). A short discussion of R-Matrix theory is given in Section 3.4. This stage of the analysis was performed using the computing facilities at the Triangle Universities Computation Center (TUCC).

Both preliminary and final fits to the data were obtained by varying the input parameters into the programs; MULT-EYE and MULTI. These parameters are the

resonance energy, laboratory width, total angular momentum and parity, and the resolution function. The total angular momentum values are determined by the shape analysis of the resonances at different angles. A s-wave resonance and a d-wave resonance are distinguished from a p-wave resonance by the cross section at 90°. A s-wave resonance and a d-wave resonance will have a dip, while a p-wave resonance will have a small peak in the cross section. At 160°, both s-wave resonances and p-wave resonances look similar but are very different from a d-wave resonance. A s-wave resonance and a p-wave resonance dip down and then up, while a d-wave resonance goes up and then dips down in the cross section.

Since shape analysis can uniquely determine only the l-values, there is an ambiguity in the total angular momentum value for p-wave resonances and d-wave resonances. In the ^{64}Zn(p,p) experiment, the p-wave resonances and d-wave resonances were fragmented analog states and the total angular momentum values were determined by the parent state total angular momentum value. In the ^{66}Zn(p,p) experiment, only s-wave resonances and p-wave resonances were observed. Most of the p-wave resonances were fragments of analog states; for the remaining p-wave resonances the total angular momentum value is uncertain.

The resonance energies are also determined by shape

analysis of the cross section. The lowest point in the dip at 90° for s-wave resonances and d-wave resonances is the resonance energy. Similarly, the highest point on the peak at 90° for a p-wave resonance is the resonance energy. The laboratory width is determined by the size or strength of the resonance.

The resolution function is much more difficult to obtain. Normally, one would fit a small f-wave resonance to determine the resolution function, since the width of an f-wave resonance is usually much less than the resolution function and an f-wave resonance exhibits a very sharp symmetric peak in the cross section. However, no f-wave resonances were observed in either experiment. Therefore, the resolution function was determined by fitting small resonances over a narrow energy range; the remaining larger resonances in this region were fit with this resolution function. The resolution function was changed only when a good fit to several consecutive resonances could not be obtained.

As a check on the final parameters, the resonance energies were changed by ± 100 eV and the cross section calculated. Similarly, the laboratory widths were varied by approximately 5% and the cross section calculated. In either case, if one of the new fits to the data was a better fit, the resonance parameters were changed to the new values and the above process repeated until the best

fits were obtained.

The remaining step of the third stage of the analysis involved correcting the experimental resonance energies. These corrections were needed for several reasons: First, since the target rod was biased at +4 kV, the resonance energies are 4 keV below the proton beam energy. Second, relativistic effects on the order of 2 keV must be included. Third, since the inner plate was negatively biased, the molecular beam was accelerated into the electrostatic analyzer.

Also, the experimental resonance energies were calibrated in order to obtain absolute resonance energies. This calibration was accomplished by comparing the experimental resonance energies to a previously calibrated resonance in ^{44}Ca, which serves as a secondary standard. This resonance in ^{44}Ca at 1.984 MeV had previously been measured and calibrated with the $^{7}Li(p,n)$ threshold at 1.8806 MeV by Wimpey (1974). The equations used to obtain these corrections were first derived by Outlaw (1976) and are documented by Westerfeldt (1977). A program (ECALI) was also written by Westerfeldt (1977) using these equations to correct the experimental resonance energies.

Upon completion of the third stage of the preliminary analysis, all of the information or parameters have been extracted from the raw data. Therefore, further analysis need only consider these parameters. The resonance

parameters for the $^{64}Zn(p,p)$ and $^{66}Zn(p,p)$ experiments are listed in Table 6.1 and Table 6.2 in Appendix 6.1.

3.3 Presentation and Discussion of Data

Analysis of the $^{64}Zn(p,p)^{64}Zn$ differential cross section from 2.50 to 3.24 MeV yields 32 $1/2^+$ resonances, 3 $1/2^-$ resonances, 2 $3/2^-$ resonances, and 2 $5/2^+$ resonances. The $1/2^-$, $3/2^-$, and $5/2^+$ resonances belong to fragmented analog states. The data and fit for all four angles between 3.10 to 3.24 MeV are shown in Figure 3.1. In this region, there are 9 $1/2^+$ resonances and 2 $5/2^+$ resonances. The strong interference effects between resonances are clearly shown in Figure 3.1, especially for the two $5/2^+$ resonances which are located at 3.21 MeV. This figure also illustrates the quality of the fit at all four angles, particularly for the $5/2^+$ states. The laboratory widths of the two $5/2^+$ resonances are 280 eV and 80 eV, and the laboratory widths for the $1/2^+$ resonances range from 40 eV to 300 eV. For the energy scales in Figures 3.1 to 3.6, uncorrected laboratory energies are used. It should also be noted that the $^{64}Zn(p,p)$ differential cross section exhibits 5% to 10% point scatter. This point scatter has several origins: statistical fluctuations,

Figure 3.1 The $^{64}Zn(p,p)^{64}Zn$ Differential Cross Section from 3.10 to 3.24 MeV for Four Angles. The solid line is the multi-level R-Matrix fit to the data.

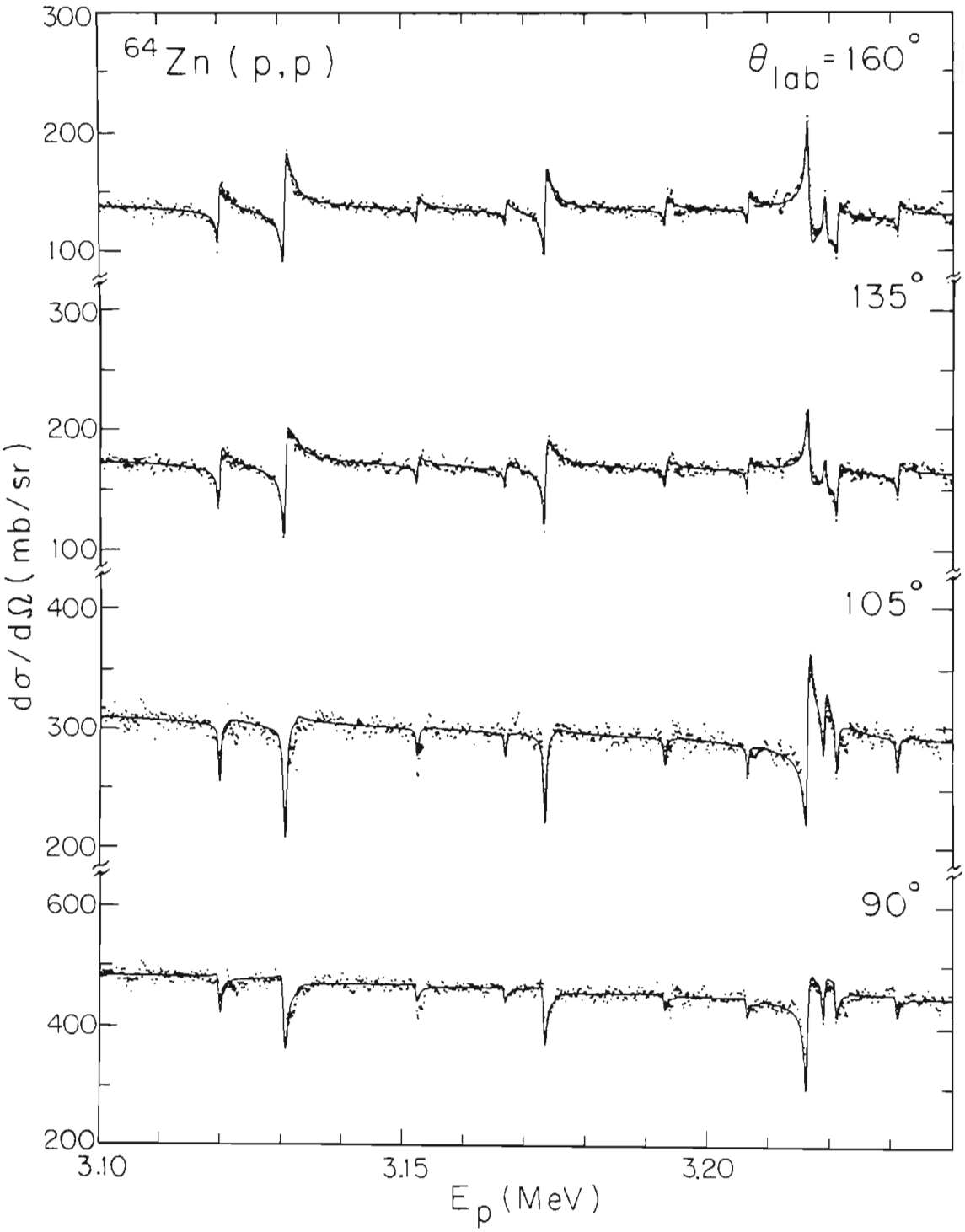
^{64}Zn (p,p)
θ_{lab} = 160°
135°
105°
90°
300
200
100
400
600
dσ/dΩ (mb/sr)
3.10
3.15
3.20
E_p (MeV)

variations in yield due to movement of the beam spot over a non-uniform target, and real variations in cross section due to very small resonances which were not completely resolved.

In Figure 3.2, the data and fit from 2.50 to 2.88 MeV are shown for angle 160°. This region includes 15 1/2+ resonances, 3 1/2− resonances, and 2 3/2− resonances. The 1/2− resonances are located at 2.74, 2.77, and 2.78 MeV and the 3/2− resonances are located at 2.81 and 2.82 MeV. The laboratory widths of the 1/2− resonances are 50, 240, and 70 eV, and the 3/2− resonances are each 40 eV. The laboratory widths of the 1/2+ resonances range from 25 to 150 eV. One interesting feature of this region is the interference effect between the 3/2− resonances and a 1/2+ resonance at 2.816 MeV. If these l=1 resonances are assumed to have j=1/2, a satisfactory fit can not be obtained, due to the interference between the s-wave resonance and the p-wave resonances. In this case the interference effect removed the usual j value ambiguity. This result is also consistent with the j value obtained from identifying the resonances as fragments of the 3/2− analog state.

Figure 3.3 shows the data and fit from 2.88 to 3.24 MeV for angle 160°. There are 17 1/2+ resonances and 2 5/2+ resonances in this region. The laboratory widths for the 1/2+ resonances range from 40 to 300 eV.

Figure 3.2 The $^{64}Zn(p,p)$ Differential Cross Section from 2.50 to 2.88 MeV for 160°. The solid line is the multi-level R-Matrix fit to the data.

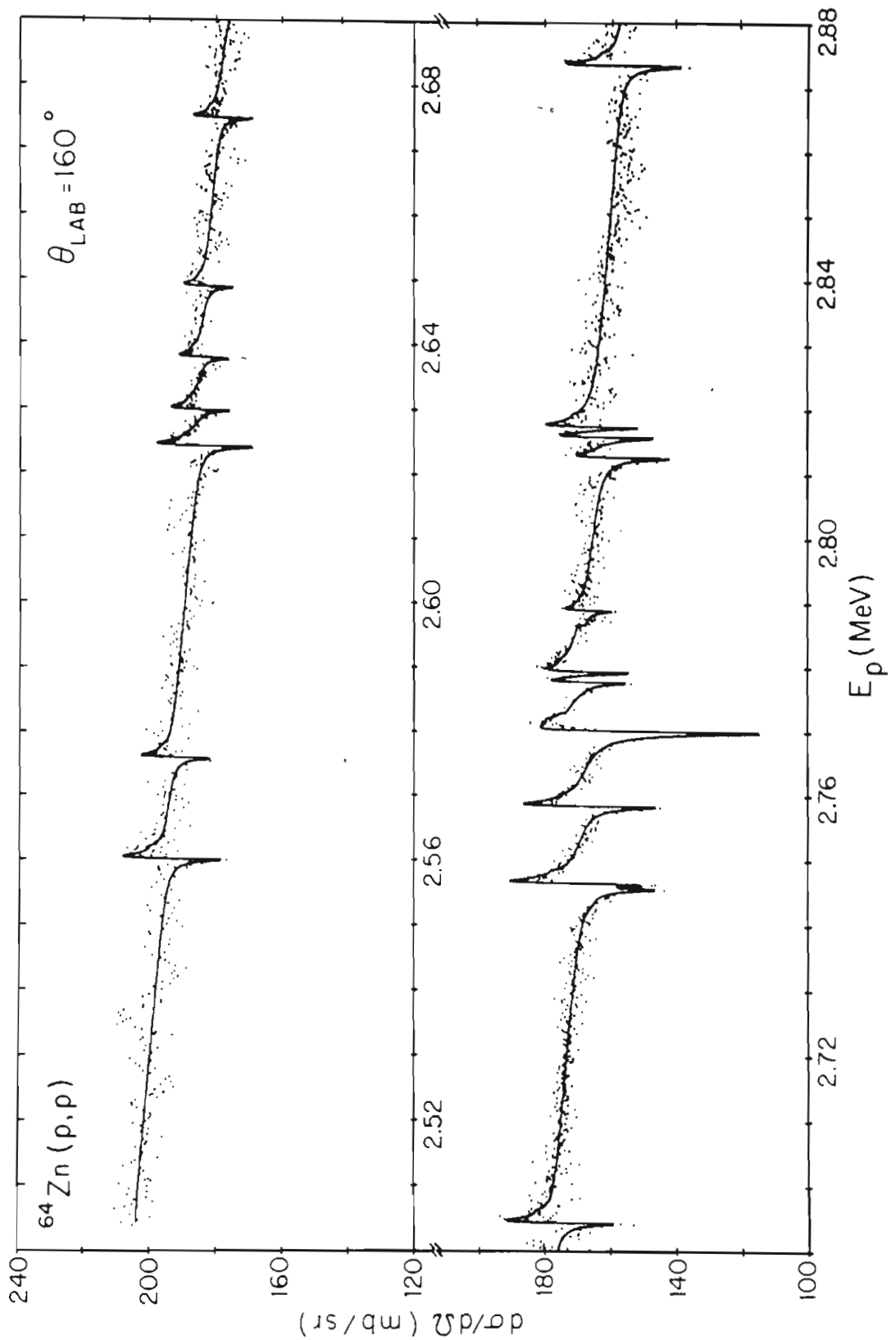
^{64}Zn (p,p)
θ_{LAB} = 160°
dσ/dΩ (mb/sr)
E_p (MeV)
240
200
160
120
180
140
100
2.52
2.56
2.60
2.64
2.68
2.72
2.76
2.80
2.84
2.88

Figure 3.3 The $^{64}Zn(p,p)$ Differential Cross Section from 2.88 to 3.24 MeV for 160°. The solid line is the multi-level R-Matrix fit to the data.

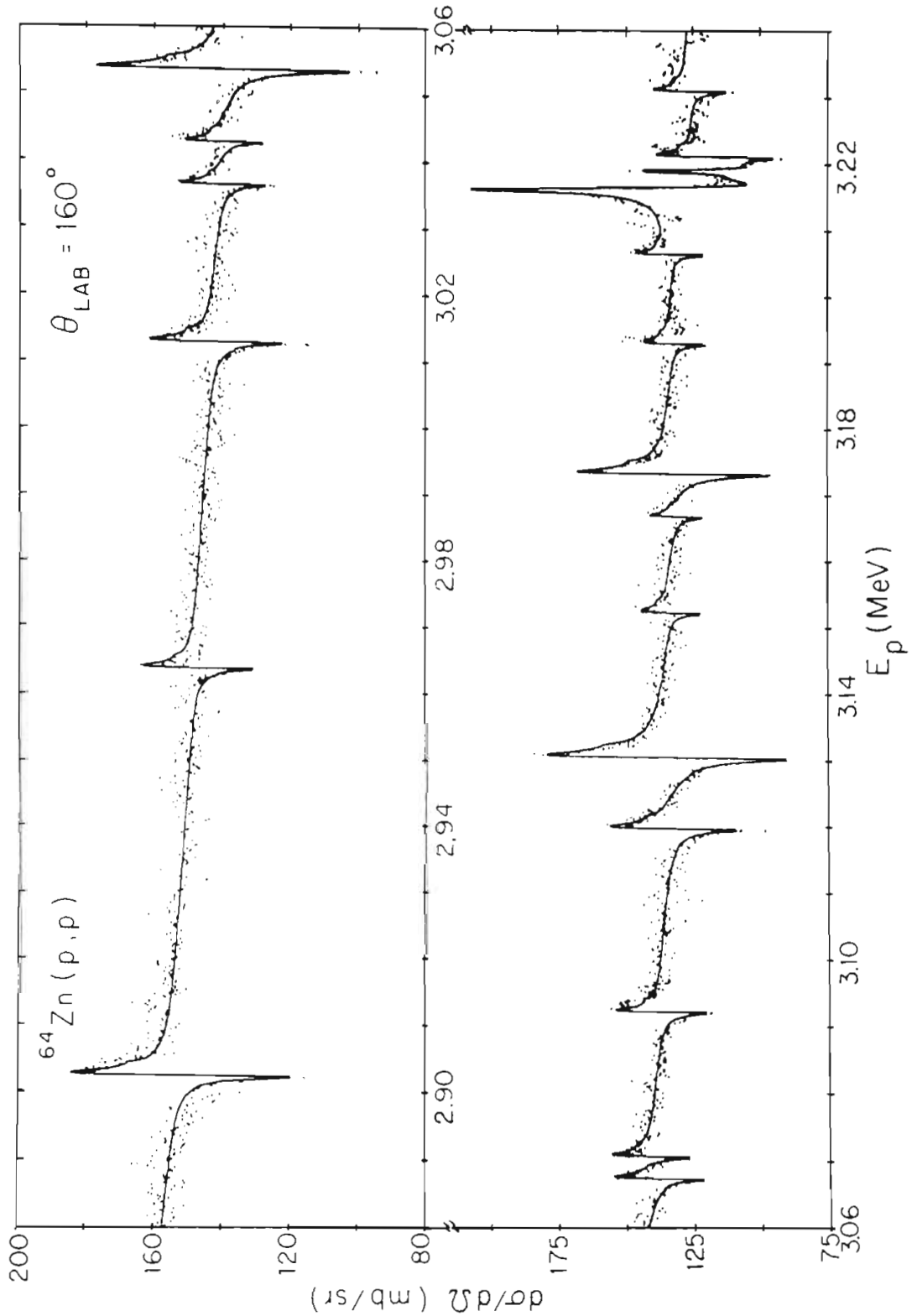
$^{64}Zn(p,p)$
$\theta_{LAB} = 160^{\circ}$
dσ/dΩ (mb/sr)
E_p (MeV)
200
160
120
80
175
125
75
2.90
2.94
2.98
3.02
3.06
3.06
3.10
3.14
3.18
3.22

Analysis of the $^{66}Zn(p,p)^{66}Zn$ differential cross section from 2.60 to 3.26 MeV yields 102 $1/2^+$, 11 $1/2^-$, and 35 $3/2^-$ resonances. The $1/2^-$ resonances were identified as a fragmented analog state and 21 of the $3/2^-$ resonances were identified as a fragmented analog state. For the remaining 14 l=1 resonances, the l-value is known, but the total angular momentum is uncertain. For definiteness, all of these resonances were assumed to have j=3/2. The differential cross section for ^{67}Ga exhibits point scatter of 2% to 3%. The point scatter in ^{67}Ga is due to many of the same effects as the point scatter in ^{65}Ga. The point scatter is smaller in ^{67}Ga since improvements were made to the detector collimators and collimator assembly before this experiment was performed (see Section 2.2).

The data and fit for all four angles in the energy range from 3.06 to 3.20 MeV are shown in Figure 3.4. In this region, there are 32 $1/2^+$ and 25 $3/2^-$ resonances. The effects of the $3/2^-$ analog state can easily be seen in Figure 3.4, especially the gross structure of the analog over a broad energy range. If the experiment had been performed with poor resolution, the individual fine structure of the analog state would have been averaged out and only this gross structure observed. The laboratory widths for the $3/2^-$ resonances range from 8 to 155 eV, and the laboratory widths for the $1/2^+$ resonances range from 8

Figure 3.4 The $^{66}Zn(p,p)^{66}Zn$ Differential Cross Section from 3.06 to 3.20 MeV for Four Angles. The solid line is the multi-level R-Matrix fit to the data.

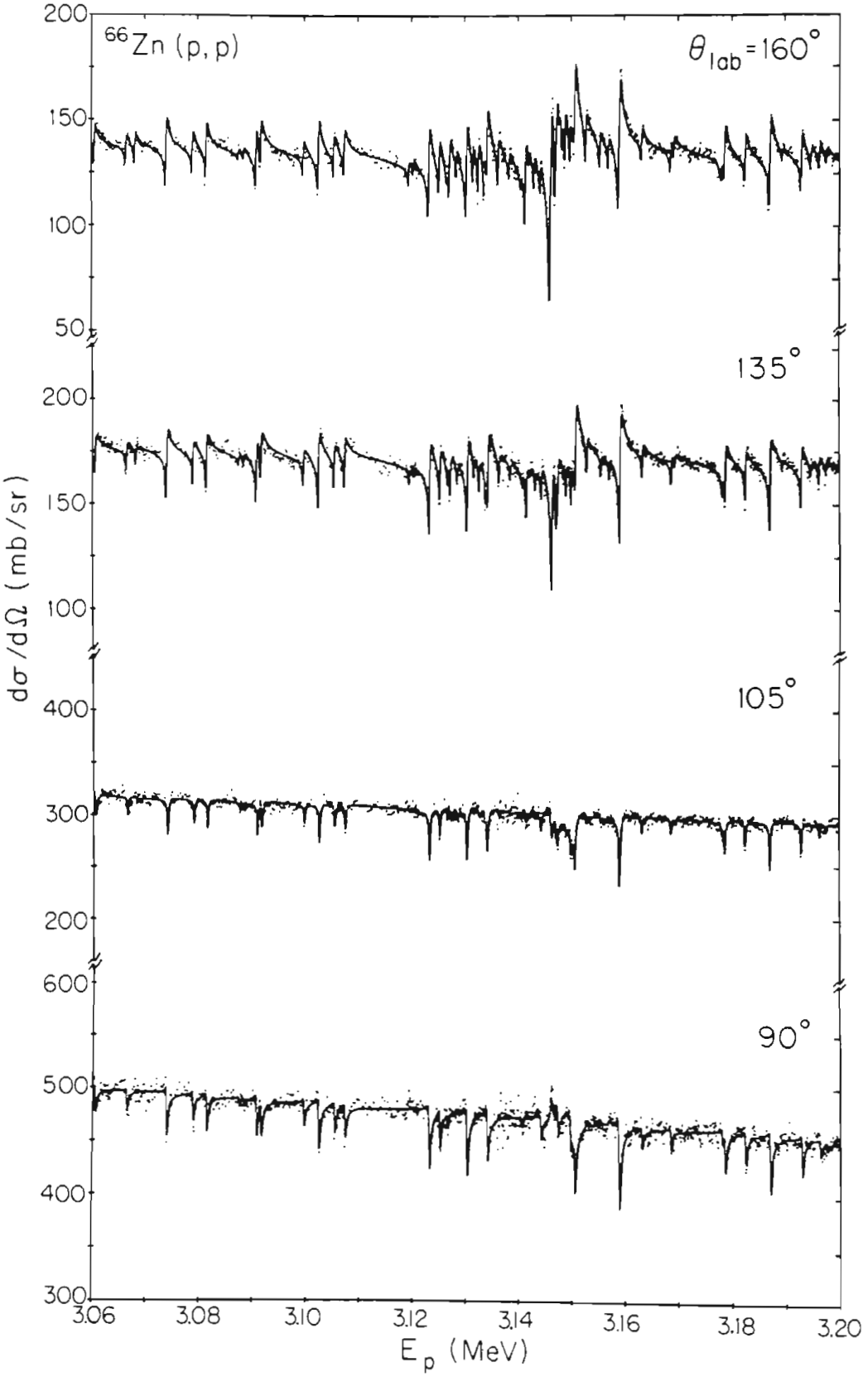
^{66}Zn (p, p)
θ_{lab} = 160°
135°
105°
90°
dσ/dΩ (mb/sr)
200
150
100
50
200
150
100
400
300
200
600
500
400
300
3.06
3.08
3.10
3.12
3.14
3.16
3.18
3.20
E_p (MeV)

to 115 eV.

Figure 3.5 shows the data and fit for 160° for the energy range 2.60 to 2.94 MeV. There are 36 $1/2^+$, 11 $1/2^-$, and 1 $3/2^-$ resonances in this region. The 11 $1/2^-$ resonances belong to a fragmented analog state. Although the gross structure of this analog is not as readily apparent as in the case of the $3/2^-$ analog, this gross structure can still be observed centered near 2.83 MeV. The laboratory widths of the $1/2^-$ resonances varied from 16 to 110 eV. The laboratory width of the $3/2^-$ resonance was 7 eV, and for the $1/2^+$ resonances, the laboratory widths varied from 10 to 85 eV.

In Figure 3.6, the data and fit for laboratory energy 2.94 to 3.26 MeV for angle 160° are shown. There are 66 $1/2^+$ and 34 $3/2^-$ resonances in this region. As noted previously, 21 of these $3/2^-$ resonances form a fragmented analog state. The laboratory widths of the $1/2^+$ and $3/2^-$ resonances range from 7 to 115 eV and 8 to 155 eV, respectively.

Figure 3.5 The $^{66}Zn(p,p)$ Differential Cross Section from 2.60 to 2.94 MeV for 160°. The solid line is the multi-level R-Matrix fit to the data.

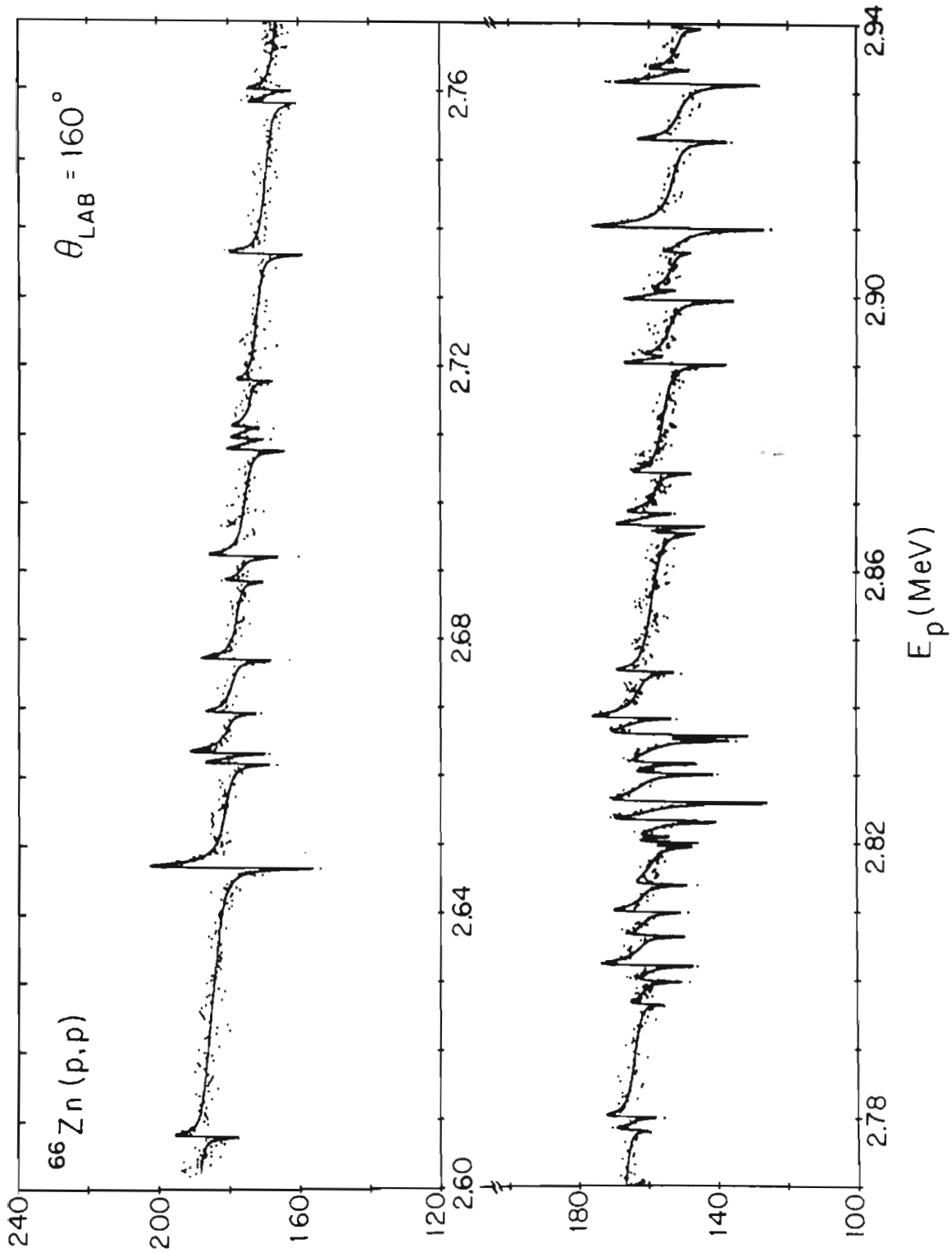
^{66}Zn (p,p)
θ_{LAB} = 160°
dσ / dΩ (mb/sr)
E_p (MeV)
240
200
160
120
180
140
100
2.60
2.64
2.68
2.72
2.76
2.78
2.82
2.86
2.90
2.94

Figure 3.6 The $^{66}Zn(p,p)$ Differential Cross Section from 2.94 to 3.26 MeV for 160°. The solid line is the multi-level R-Matrix fit to the data.

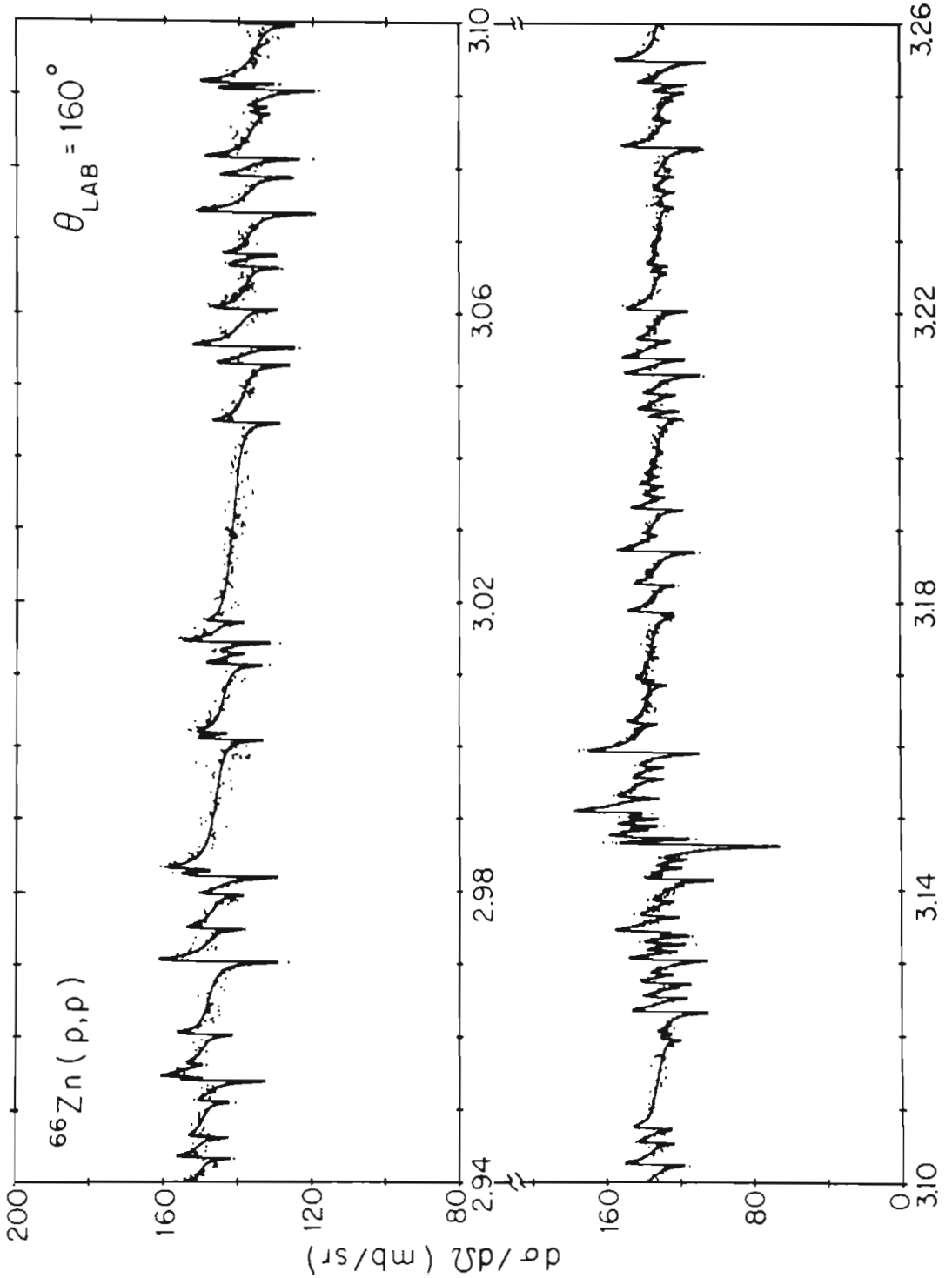
$^{66}Zn(p,p)$
$\theta_{LAB} = 160°$
$d\sigma/d\Omega$ (mb/sr)
200
160
120
80
2.94
2.98
3.02
3.06
3.10
160
80
0
3.10
3.14
3.18
3.22
3.26
E_p (MeV)

3.4 R-Matrix Theory

R-Matrix theory is a rigorous theory of nuclear reactions which is not dependent upon any particular physical picture such as the compound nucleus model. This theory was first formulated by Wigner and Eisenbud (1947). The review article by Lane and Thomas (1958) gives an extensive discussion of R-Matrix theory and its applications; the notation of this review is almost universally adopted.

In R-Matrix theory, radial space is partitioned into two different regions in order to solve the Schroedinger equation. The boundary between these two regions is defined by the channel radius, a_c, which is the separation beyond which the projectile and target feel no mutual nuclear interaction. The Schroedinger equation can be solved exactly in the external region ($r>a_c$) since only the Coulomb force is present. The solution of this equation yields the well known confluent hypergeometric functions, F and G. Appropriate linear combinations of these solutions represent incoming and outgoing waves. The wave function in the external region can be expressed

as a function of these incoming and outgoing spherical waves.

The next step would normally be to solve the Schroedinger equation in the internal region and then match the logarithmic derivative of the internal and external wave functions at the boundary ($r=a_c$). However, this method requires a functional form for the nuclear potential. The method of R-Matrix theory is to postulate a complete set of wave functions which are solutions or eigenstates of the Hamiltonian in the internal region. The wave function in the internal region can be expressed in terms of this complete set of wave functions. Next, the logarithmic derivatives of the internal and external wave functions are matched at $r=a_c$. Since the differential cross section is easily expressed in terms of the external wave functions, and the internal and external wave functions are matched at the boundary ($r=a_c$), the differential cross section can be expressed in terms of the internal wave functions.

One attractive feature of R-Matrix theory is that the reduced widths, γ^2, are proportional to the square of the amplitudes of the internal wave functions. The reduced widths are related to the observed laboratory width, Γ, by $\Gamma=2P\gamma^2$, where P is the penetrability through the Coulomb barrier. Also, the eigenvalues associated with each internal wave function are proportional to the resonance

energies. Therefore, by determining the laboratory energies and laboratory widths of the resonances in the fitting procedure, the eigenvalues and the square of the amplitudes of the internal wave functions are determined.

Chapter 4

Analysis and Discussion of Results

4.1 Strength Functions

One of the major purposes of these experiments was to determine the s-wave strength function for ^{64}Zn and ^{66}Zn. The s-wave strength function is defined as

$$S = \langle \gamma^2 \rangle / \langle D \rangle$$

where $\langle \gamma^2 \rangle$ is the observed average reduced width and $\langle D \rangle$ is the observed level spacing. The s-wave strength function provides information on the average characteristics of nuclear resonance levels. These average characteristics of nuclear resonances are predicted by the optical potential model. Of particular interest here is the location of the 3s single particle giant or size resonance. The 3s giant resonance was predicted to show a maximum at A=68 by Margolis and Weisskopf (1957), who used a square-well proton nuclear potential plus a Coulomb potential. It should be noted that almost all experimental information on strength functions has come from neutron experiments.

Measurements by Schiffer et al. (1957) and Johnson et al. (1957) seem to indicate the maximum of the s-wave strength function near A=70. Johnson measured the (p,n) reaction cross section for twelve thick targets ranging in atomic weight from 37 to 93. Schiffer measured the (p,n) reaction cross section for thick targets of thirty-one elements ranging in atomic weight from 37 to 133 with incident proton energies between 2.0 and 4.0 MeV. The reaction yields were divided by a penetrability factor to yield a "reduced cross section" which is related to the proton strength function. The (p,n) reaction cross section is averaged over many hundreds of levels in the compound nucleus and includes the contributions from all l values.

However, in an experiment by Jones(1959), it was shown that the (p,n) reaction does not always provide a reliable measure of the proton reaction cross section, thereby suggesting that the energy dependence of the giant resonances was not as well known as previously thought. In other words, although Schiffer and Johnson measured a peak in the (p,n) cross section near A=70, it is less clear that these measurements definitively locate the 3s giant resonance.

A more direct measurement of the s-wave strength function was needed. It should be noted that increasing energy is equivalent to increasing atomic mass. As was

mentioned in the Introduction, a systematic study of proton resonances has been undertaken at TUNL; the present experiments are part of this overall study. The excellent energy resolution of these experiments allow the individual resonances to be resolved. The s-wave strength function is easily calculated from the reduced widths and resonance energies.

The s-wave strength function for the ^{64}Zn(p,p) experiment was determined to be 0.051 with a fractional error of 25%. This value included 32 s-wave resonances in the energy range 2.50 to 3.24 MeV. The fractional statistical error for a Porter-Thomas distribution is $\sqrt{2/n}$, where n is the number of levels. The s-wave strength function for the ^{66}Zn(p,p) experiment was determined to be 0.078 with a fractional error of 20%, and included 51 s-wave resonances in the energy range 3.05 to 3.26 MeV. An explanation for using only the upper 51 1/2+ resonances is given later in this Section.

The observed s-wave strength function versus atomic mass number, A, is shown in Figure 4.1. This figure contains the results from previous work performed at TUNL(Bilpuch et al., 1976) and present results for the ^{64}Zn(p,p) experiment and the ^{66}Zn(p,p) experiment. The s-wave strength function shows an increase for A=66 consistent with past results from the (p,n) cross section data, if one assumes that A=66 is on the lower edge of the

Figure 4.1 The s-wave Strength Function for Masses between A=25 and 70.

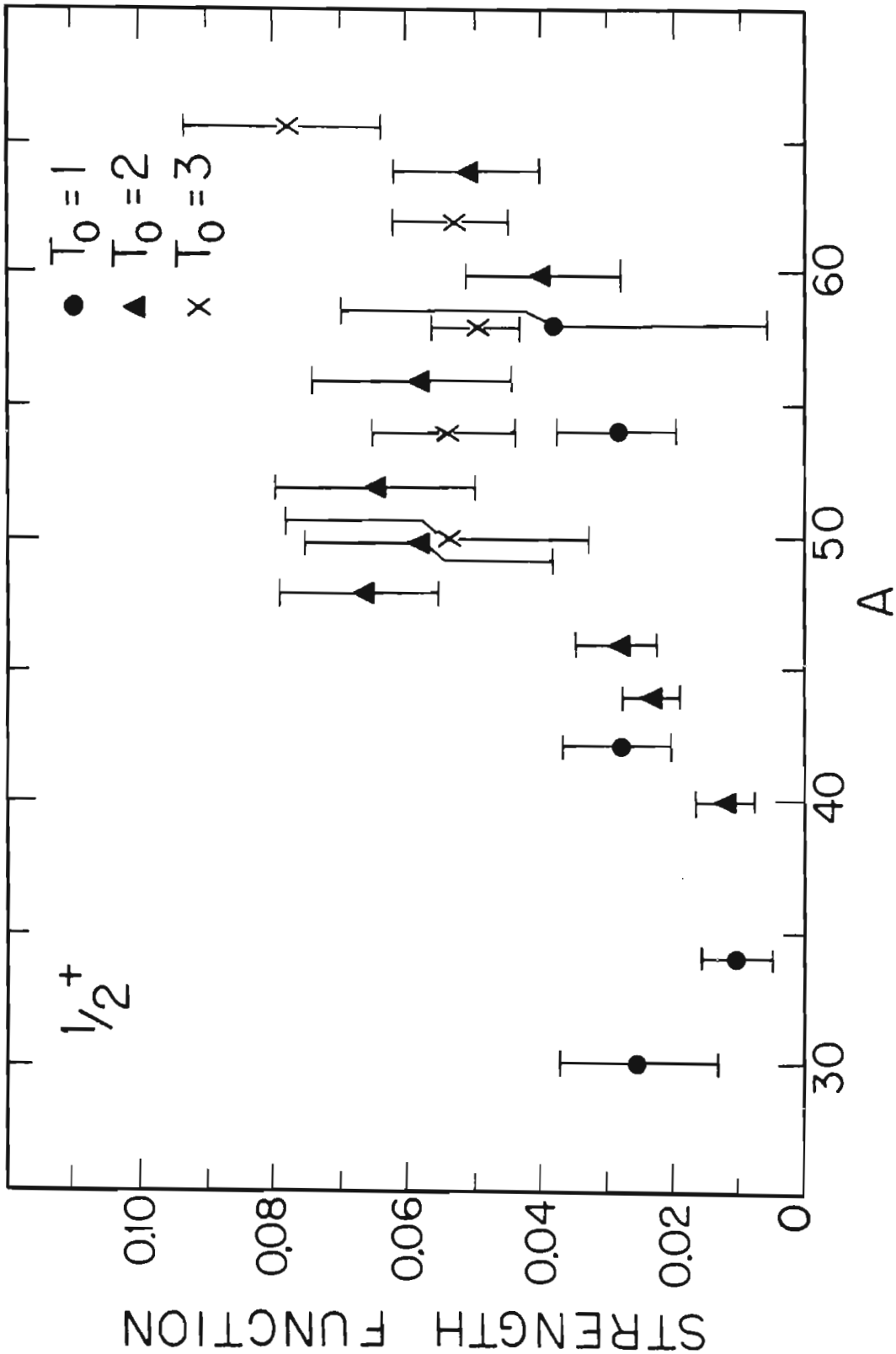
STRENGTH FUNCTION
0.10
0.08
0.06
0.04
0.02
0
30
40
50
60
A
$1/2^+$
$T_0 = 1$
$T_0 = 2$
$T_0 = 3$

3s giant resonance. However, the s-wave strength function has not been measured for A > 66 with these definitive proton elastic scattering experiments. It is interesting to note that the measurement of the neutron s-wave strength function indicates a strong peak for A around A=55 with the peak to background approximately a factor of 10. To clarify the situation experimentally, more measurements of the s-wave strength function are required for A greater than 66. However, these experiments will be extremely difficult to perform due to the higher Coulomb barrier and to increased level densities.

As mentioned previously, the upper 51 s-wave resonances were used to calculate the s-wave strength function. To understand why only the upper half of the resonances were used to determine the s-wave strength function, it is first necessary to consider effects on the s-wave strength function due to systematic experimental error. The major source of experimental error affecting the s-wave strength function arises from missing small levels. In the ^{64}Zn(p,p) experiment, the smallest laboratory width was 25 eV, which corresponds to a reduced width of 0.750 keV. In ^{66}Zn(p,p), the smallest laboratory width was 8 eV, which corresponds to a reduced width of 0.134 keV. Any levels whose laboratory widths were smaller than these "cutoff" widths were not observed in these experiments.

The effect of missing small resonances on the s-wave strength function can best be understood with an equivalent definition of the strength function,

$$S = \sum \gamma^2 \Delta E$$

where ΔE is the energy range of the experiment. If small resonances are missed, then the observed s-wave strength function will be too low. It is crucial to know how many small resonances were missed and the contribution these small resonances have on the sum of the reduced widths.

The differential and cumulative sum of the reduced widths, and the cumulative sum of the number of resonances in ^{65}Ga and ^{67}Ga are examined in order to determine if small resonances were missed. In Figure 4.2 and Figure 4.3, the differential and cumulative sum of the $1/2^+$ reduced widths for ^{65}Ga and ^{67}Ga are shown. The cumulative sum of the reduced widths for ^{65}Ga is approximately a linear and smooth function. This suggests that about the same fraction of resonances was missed in all regions. However, the cumulative sum of the reduced widths for ^{67}Ga shows a slightly steeper slope for the upper half of the data than for the lower half of the data, which may indicate that more resonances were missed in the lower half of the data than in the upper half.

The cumulative sum of the number of resonances for ^{65}Ga and ^{67}Ga are shown in Figure 4.4. The cumulative sum of the number of resonances in ^{65}Ga is approximately

Figure 4.2 Differential and Integral Plots of the 1/2+ Reduced Widths in ^{65}Ga.

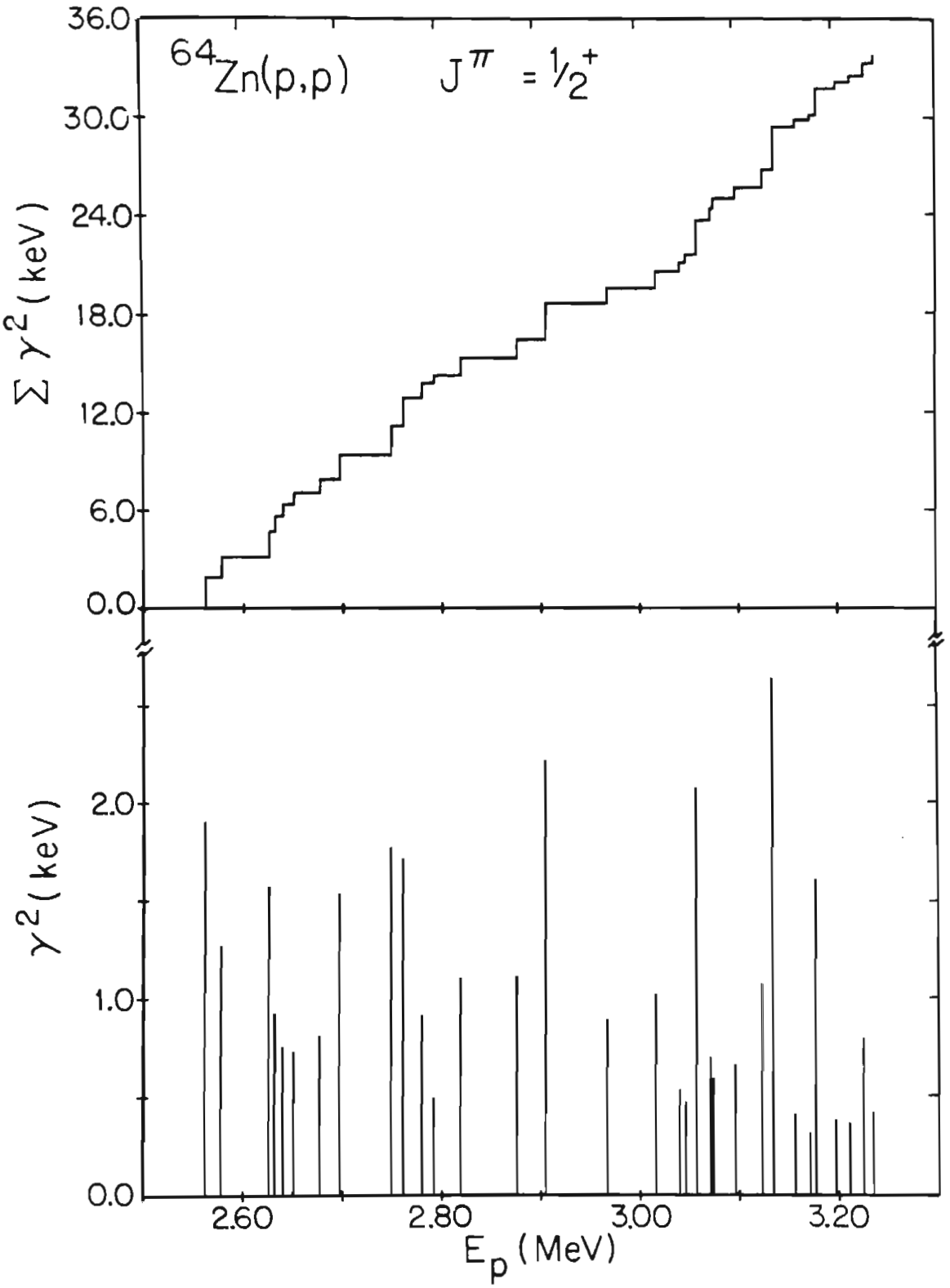
^{64}Zn(p,p)
$J^{\pi} = 1/2^{+}$
$\Sigma \gamma^2$ (keV)
36.0
30.0
24.0
18.0
12.0
6.0
0.0
γ^2 (keV)
2.0
1.0
0.0
2.60
2.80
3.00
3.20
E_p (MeV)

Figure 4.3 Differential and Integral Plots of the $1/2^+$ Reduced Widths in ^{67}Ga.

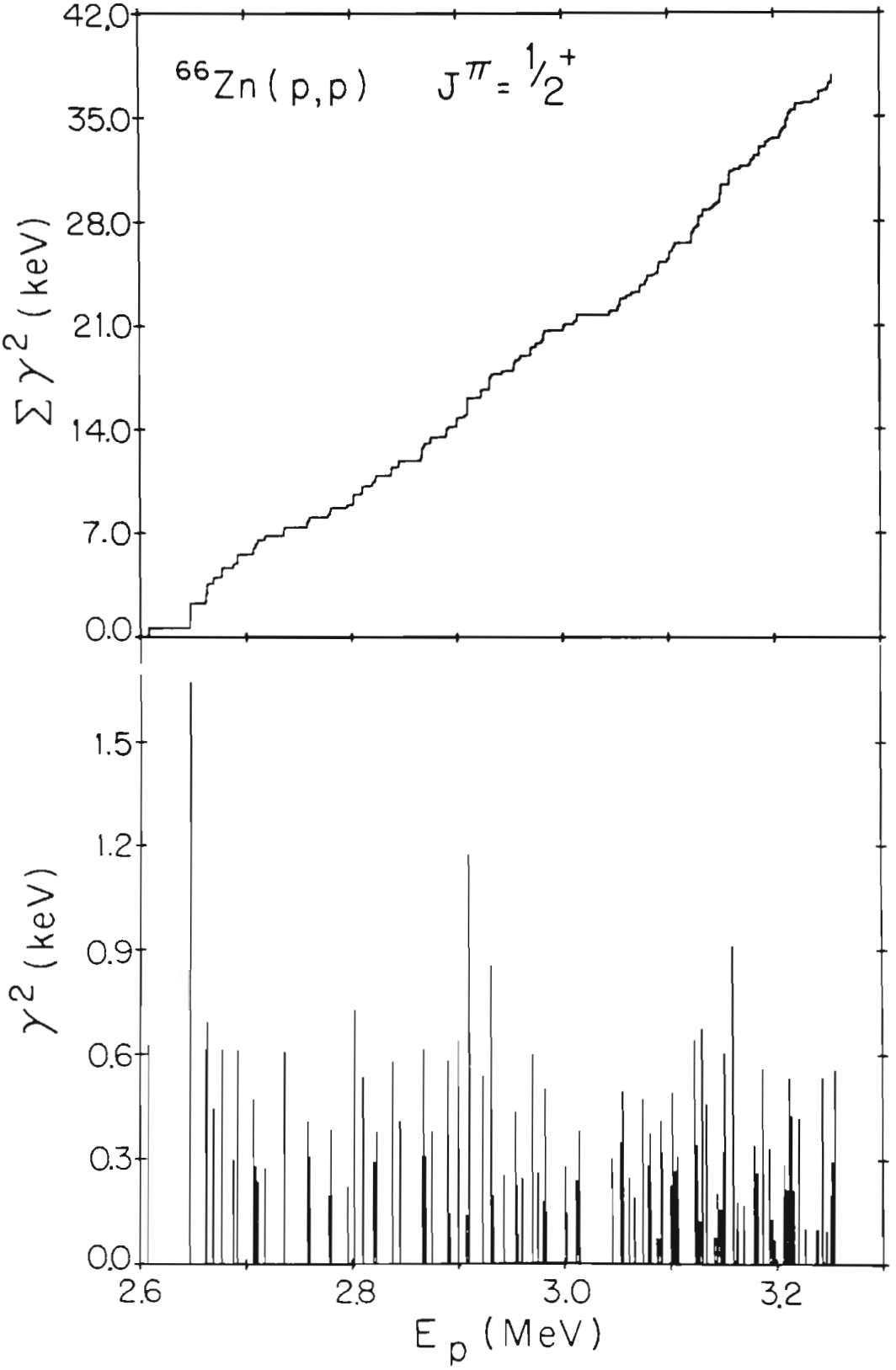
^{66}Zn (p, p)
$J^{\pi} = 1/2^{+}$
$\Sigma \gamma^2$ (keV)
42.0
35.0
28.0
21.0
14.0
7.0
0.0
γ^2 (keV)
1.5
1.2
0.9
0.6
0.3
0.0
2.6
2.8
3.0
3.2
E_p (MeV)

Figure 4.4 Cumulative Sum of the Number of Resonances in ^{65}Ga and ^{67}Ga.

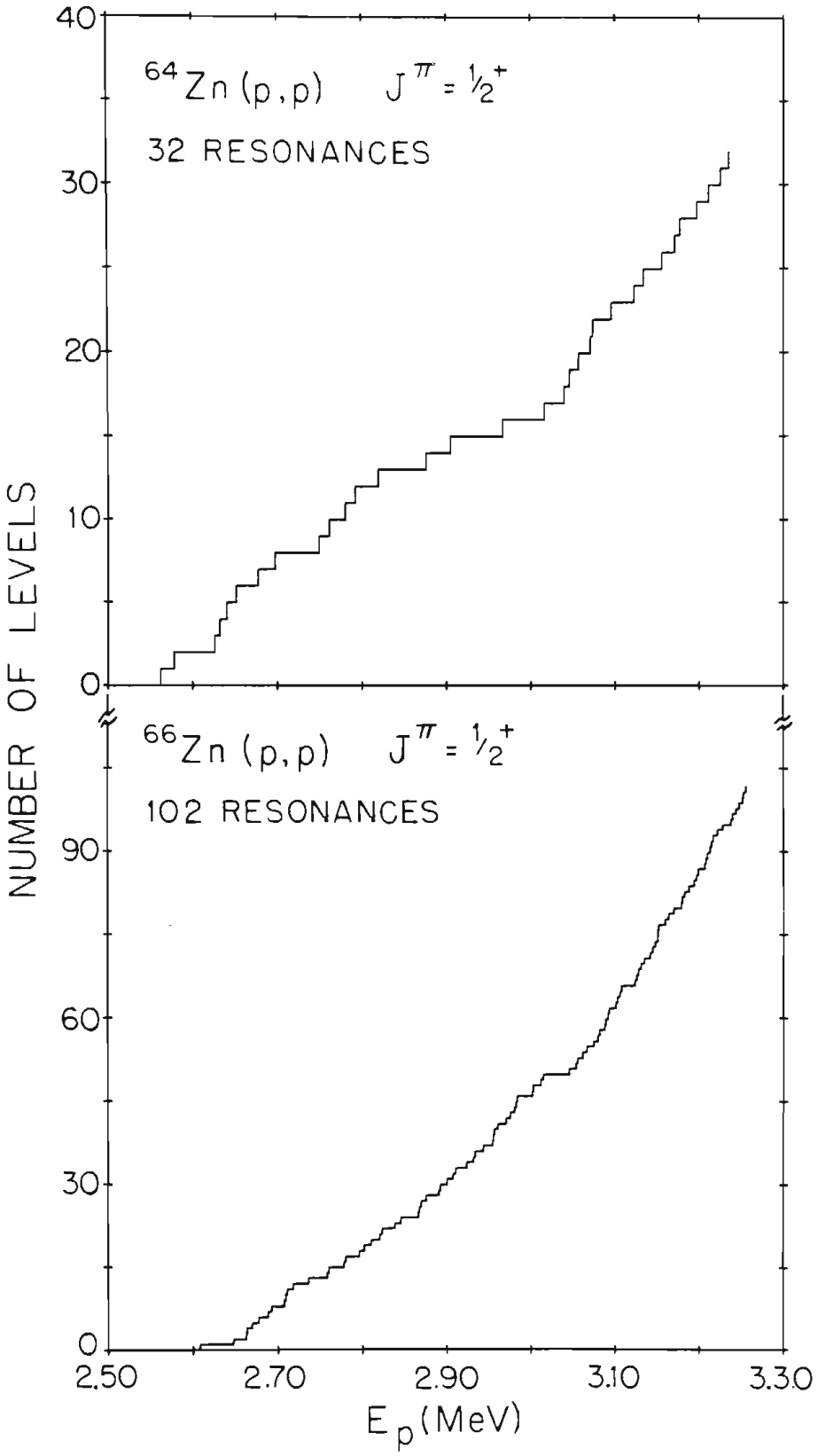
^{64}Zn (p,p) $J^{\pi} = 1/2^+$
32 RESONANCES
^{66}Zn (p,p) $J^{\pi} = 1/2^+$
102 RESONANCES
NUMBER OF LEVELS
0
10
20
30
40
0
30
60
90
2.50
2.70
2.90
3.10
3.30
E_p (MeV)

linear. However, for ^{67}Ga, the cumulative sum is definitely steeper for the upper region of the data than for the lower region. More resonances were probably missed in the lower region of the data than in the upper region for ^{67}Ga, with approximately the same number of resonances missed in all regions for ^{65}Ga.

The number of missing small resonances was obtained by comparing the experimental data to the Wigner and Porter-Thomas distributions. In Section 4.2 and Section 4.3, the Wigner and Porter-Thomas distributions are discussed with particular reference to the utilization of these distributions to determine the number of missing resonances. In this section only the results are needed. Analysis of these data seems to indicate that 50% of the levels were missed in ^{65}Ga, which corresponds to missing 8% of the sum of the reduced widths. In this case, missing 8% of the strength is not significant since the corrected value for the s-wave strength function is still well within the error bar of the uncorrected value. However, in the ^{66}Zn experiment, the indication is that an average of 70% of the levels were missed over the entire energy range, which corresponds to missing 20% of the sum of the reduced widths. The s-wave strength function was 0.058 for the entire energy range. Since only 80% of the sum of the reduced widths was observed, the measured s-wave strength function is 80% of the "true" value of

0.073. If only the upper 51 s-wave resonances are considered in the ^{66}Zn experiment, the indication is that approximately 30% of the levels were missed, which corresponds to missing approximately 2% of the sum of the reduced widths. Since only a small fraction of the sum of the reduced widths is missed, the value for the s-wave strength function using the upper 51 1/2$^+$ resonances is a good estimate of the true value. The corrected value of 0.073 for the s-wave strength function for the entire energy range in ^{67}Ga is in fair agreement with the value of 0.078 calculated from the upper 51 s-wave resonances.

In conclusion, the s-wave strength function for ^{64}Zn was determined to be 0.051. By using the upper 51 s-wave resonances in ^{66}Zn, the value of 0.078 was obtained for the s-wave strength function. This result in ^{66}Zn is larger than values of the s-wave strength function for lower A, and seems consistent with past results from the (p,n) cross section data.

4.2 Spacing Distribution

The distribution of the nearest neighbor level spacings is defined as,

$$P(x)\,dx = (\pi/2)\,x\,\exp(-\pi x^2/4)\,dx$$

where $x=D/\langle D\rangle$, D is the spacing between adjacent levels, and $\langle D\rangle$ is the average spacing. This spacing distribution is referred to as the Wigner distribution. An excellent discussion on the Wigner distribution is given by Lynn(1968).

One normally compares the experimental data to the Wigner distribution to determine if the data does in fact fcllow the distibution. However, in these experiments, many small resonances were not observed. The assumption is therefore made that if all resonances had been observed the data would follow a Wigner distribution. Then the Wigner distribution can be used to infer the number of resonances which were not observed, and this result can be used in other calculations such as the s-wave strength function.

Before the experimental spacing distributions can be compared to the Wigner distribution, the experimental spacings are normally corrected for the energy dependence

of the level density. The equation used to correct for the energy dependence of the spacing between nearest neighbor resonances has the form (Lynn, 1968):

$$\langle D \rangle \sim \exp(-E_X/T),$$

where E_X is the excitation energy of the compound nucleus and T is the "nuclear temperature". This equation is usually rewritten since,

$$E_X = B_p + E_p$$

where B_p is the binding energy of the proton and E_p is the laboratory energy of the incident proton resulting in,

$$\langle D \rangle = \langle D_o \rangle \exp(-E_p/T)$$

The spacing between nearest neighbor resonances as a function of energy is fit (in the least square sense) to the above equation (Bilpuch et al., 1971). Next, corrected spacings are calculated using the results of the fit, and this corrected spacing distribution is compared to the Wigner distribution.

In the ^{64}Zn experiment, the spacing distribution was not corrected since only 32 resonances were observed. The histogram of the uncorrected spacing distribution for the $1/2^+$ resonances in ^{65}Ga is shown in Figure 4.5, with the solid curve a Wigner distribution normalized to 31 spacings. The centroid of the data histogram has shifted to smaller values of X compared to the Wigner distribution. The histogram is below the Wigner distribution for X between 1.0 and 2.0, and for X greater

Figure 4.5 Spacing Distribution for ^{65}Ga. The solid line is the Wigner distribution normalized to 31 spacings.

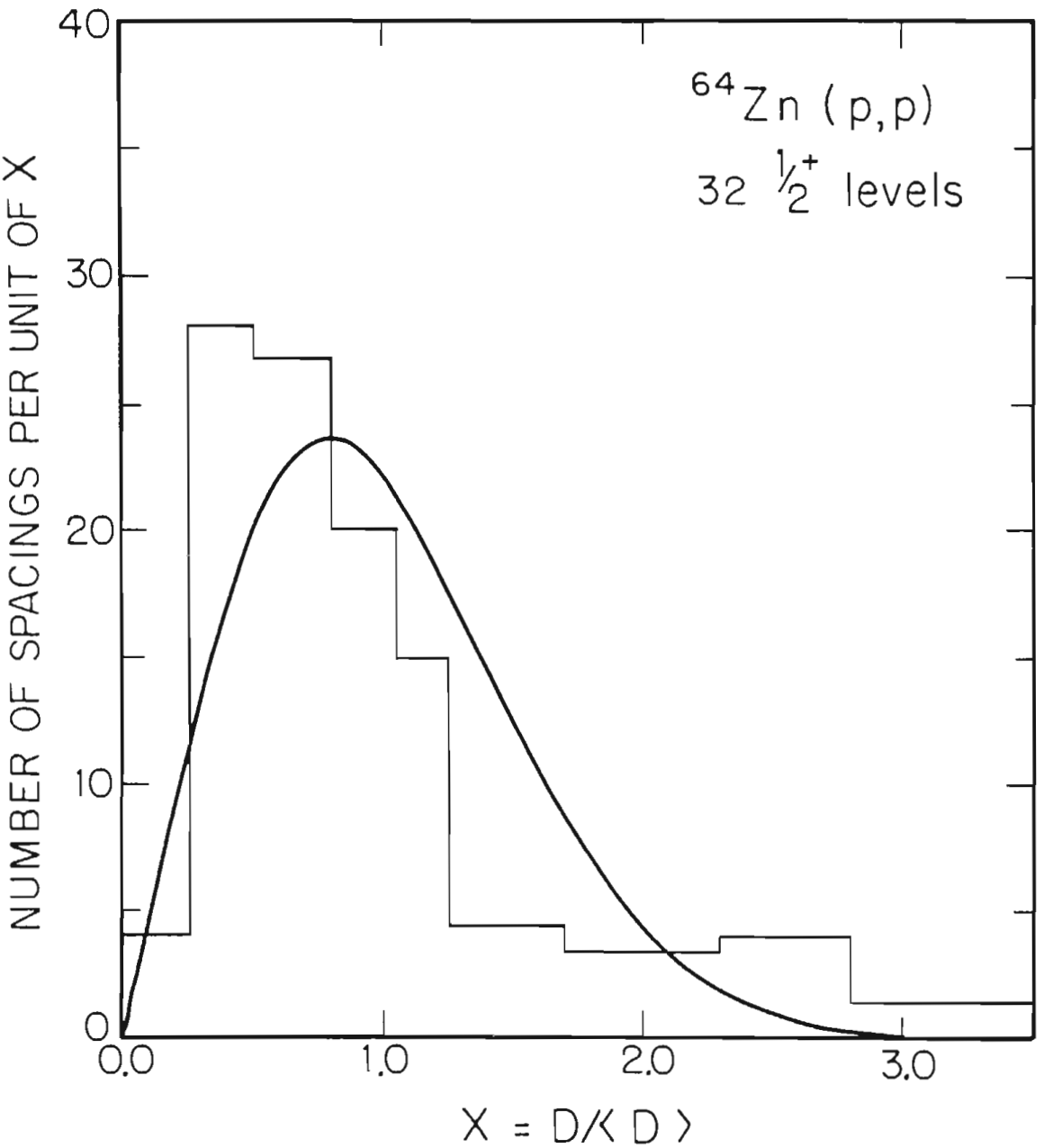
^{64}Zn (p,p)
32 $\frac{1}{2}^+$ levels
NUMBER OF SPACINGS PER UNIT OF X
X = D/⟨D⟩
0
10
20
30
40
0.0
1.0
2.0
3.0

than 2.0, the histogram is above the Wigner distribution.

In the ^{66}Zn experiment, the spacing distribution was corrected since 102 s-wave resonances were observed. However, due to the effects of missing many small resonances, a good fit to the nuclear temperature was not obtained. Therefore, the nuclear temperature (T = 0.89 MeV) given by Gilbert and Cameron(1965) was used to correct the spacing distribution. The uncorrected spacing distribution is shown in Figure 4.6 for ^{67}Ga. The solid curve is the Wigner distribution normalized to 101 spacings since 102 1/2+ resonances were observed. Again, the centroid of the histogram has moved down to smaller values of X, and the histogram is below the solid curve for X between 1.0 and 2.0. However, in this case these effects are more pronounced than for the spacing distribution of the ^{65}Ga resonances. The corrected spacing distribution for ^{67}Ga is shown in Figure 4.7. Although the differences between the corrected spacing distribution and the Wigner distribution are not as pronounced as the differences between the uncorrected spacing distribution and the Wigner distribution, the histogram is still below the Wigner distribution for X between 1.0 and 2.0, and the centroid has shifted to smaller values of X. The uncorrected and corrected spacing distributions for the upper 51 resonances in ^{67}Ga are shown in Figure 4.8. The corrected spacing

Figure 4.6 Uncorrected Spacing Distribution for ^{67}Ga. The solid line is the Wigner distribution normalized to 101 spacings.

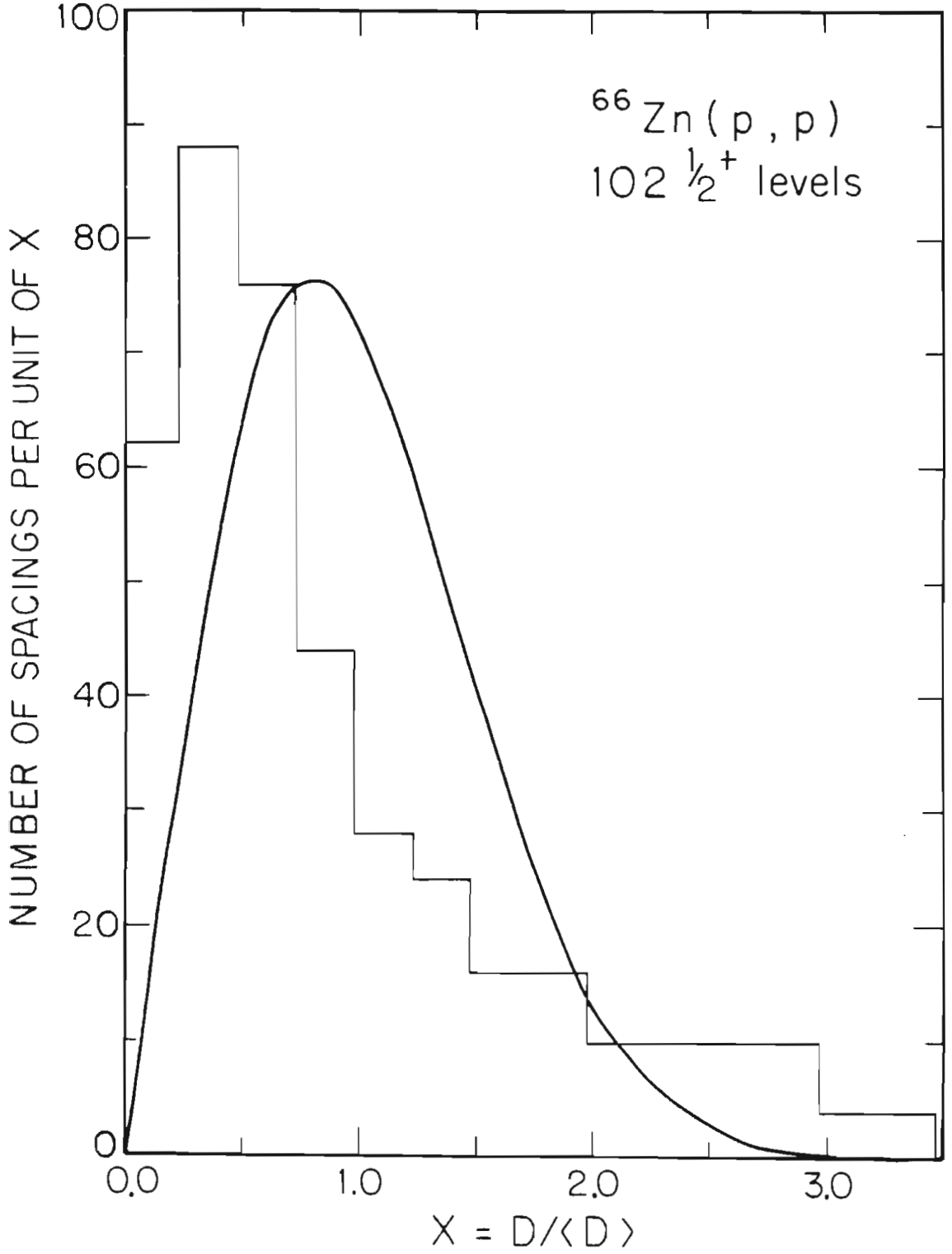
^{66}Zn(p, p)
102 ½$^{+}$ levels
NUMBER OF SPACINGS PER UNIT OF X
100
80
60
40
20
0
0.0
1.0
2.0
3.0
X = D/⟨D⟩

Figure 4.7 Corrected Spacing Distribution for ^{67}Ga. The solid line is the Wigner distribution normalized to 101 spacings.

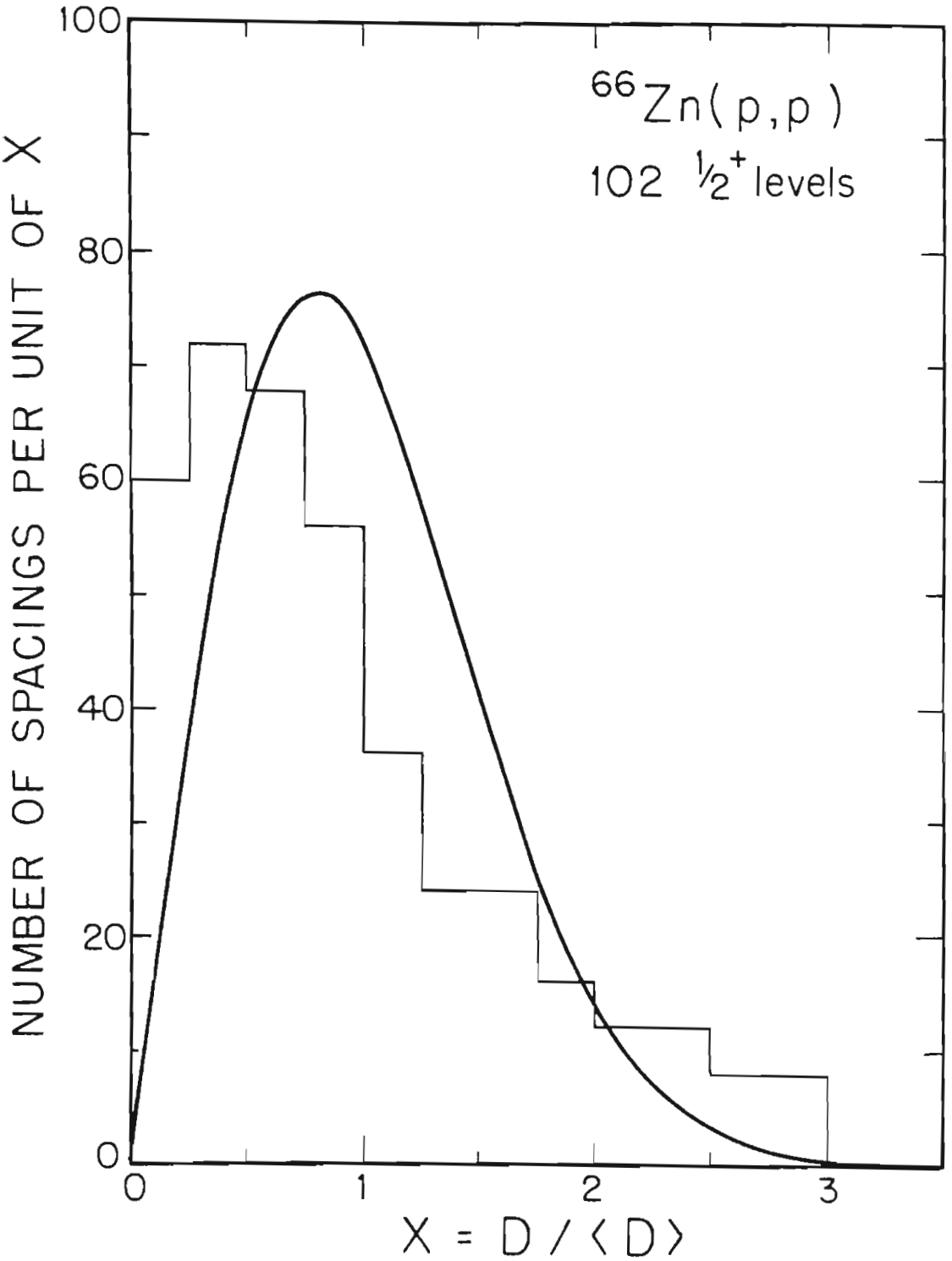
^{66}Zn(p,p)
102 ½$^{+}$ levels
NUMBER OF SPACINGS PER UNIT OF X
X = D / ⟨D⟩
0
20
40
60
80
100
0
1
2
3

Figure 4.8 Uncorrected and Corrected Spacing Distributions for the upper 51 resonances in ^{67}Ga. The solid line is the Wigner distribution normalized to 50 spacings.

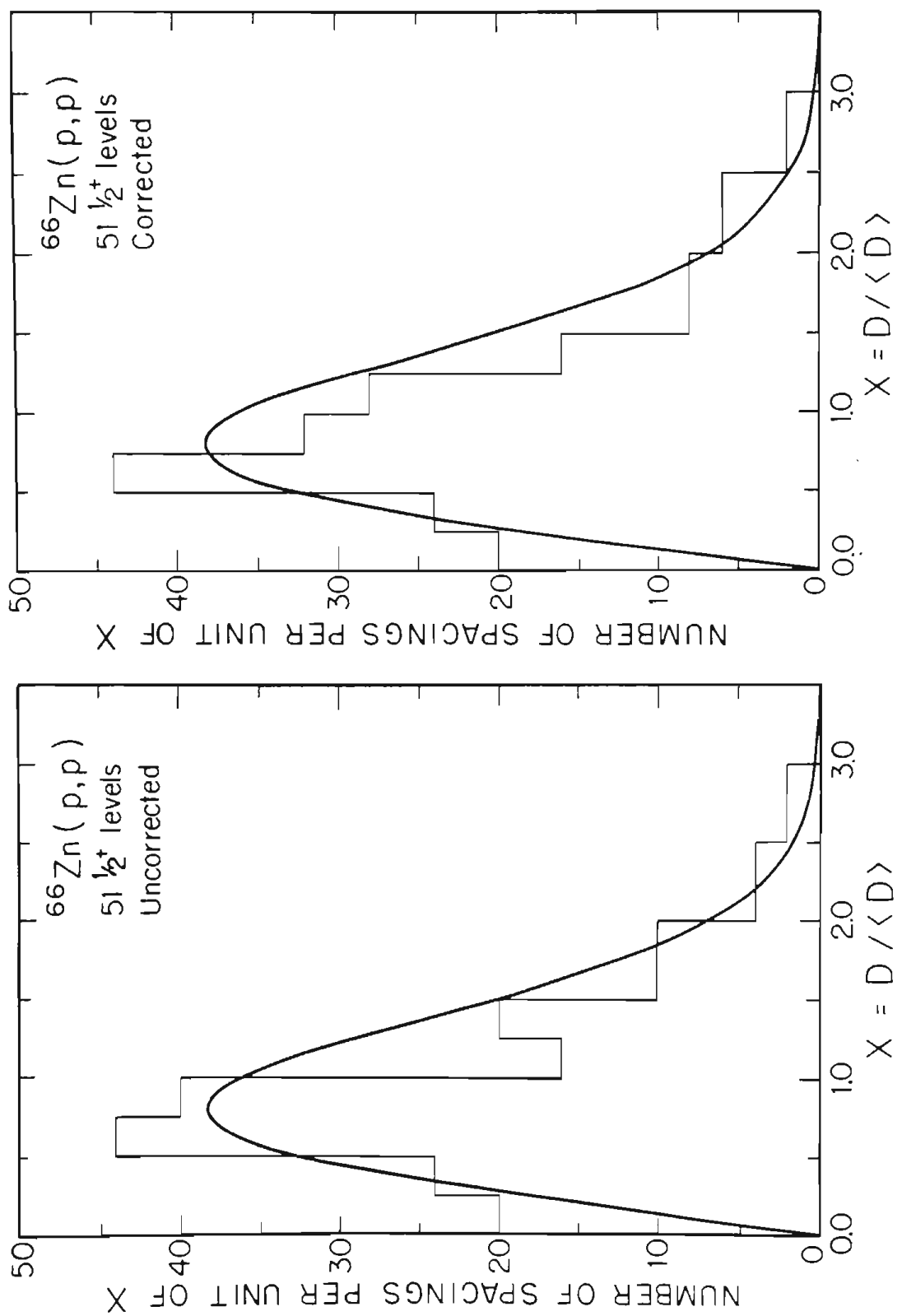
^{66}Zn (p,p)
51 ½$^{+}$ levels
Uncorrected
NUMBER OF SPACINGS PER UNIT OF X
X = D / ⟨D⟩
0.0
1.0
2.0
3.0
0
10
20
30
40
50
^{66}Zn (p,p)
51 ½$^{+}$ levels
Corrected
NUMBER OF SPACINGS PER UNIT OF X
X = D / ⟨D⟩

distribution has the shape or form of the normalized Wigner distribution, unlike the spacing distributions for ^{65}Ga, and for the entire energy range of ^{67}Ga.

As previously mentioned, the difference between the data histogram and the normalized Wigner distribution is assumed to be due to missing small resonances. In order to test this hypothesis, a computer simulation program was written which generated one million spacings from the Wigner distribution and calculated the effects of missing small resonances. The procedure used to generate this set of spacings was as follows: First, a random number is generated between 0 and 1. Second, the random number is set equal to the integral of the Wigner distribution with the limits of the integral being 0 and X. This equation is numerically solved using the Newton-Raphson method giving the value of X. Last, this value of X is then used as a value for one spacing. This procedure was repeated until one million spacings were generated.

The procedure used to simulate the effect of missing levels was to generate a random number, i, between zero and the total number of spacings. Next, the (i) element of the spacing matrix is added to the (i+1) element of the matrix reducing the number of spacing by one. In other words, the level separating the (i) and (i+1) spacing is removed simulating the effect of missing this level. This procedure was followed until 5% of the levels were removed

from the original sequence of spacings. The results for the Wigner distribution simulating the effect of missing 5% of the levels was then plotted . The above procedure is then used to removed an additional 5% of the levels. This procedure was followed until only 5% of the levels remained out of the original one million spacings.

The results of this simulation are shown in Figures 4.9 to 4.13. The histograms and the Wigner distribution are normalized to 101 spacings. These curves demonstrate that the effect of missing small resonances show the same characteristics as the spacing distributions of ^{65}Ga and ^{67}Ga. In other words, as more levels are missed, the centroid of the histogram shifts to smaller values of X. Also, the histogram drops below the Wigner distribution for values of X between 1.0 and 2.0, and the histogram is above the Wigner distribution for X greater than 2.0.

The next step is to determine how many levels were missed by comparing the experimental spacing distributions of ^{65}Ga and ^{67}Ga with the modified distributions of Figures 4.9 to 4.13. The most obvious and easiest method is to visually compare the distributions. However, one would prefer a more quantitative means of analysis. Therefore, the second and third moments of these modified distributions were calculated and compared with the experimental distributions. The second and third moments are used since the first moment is always equal to one by

Figure 4.9 Simulation of the Effects of Missing 0% to 15% of the Resonances on the Wigner Distribution.

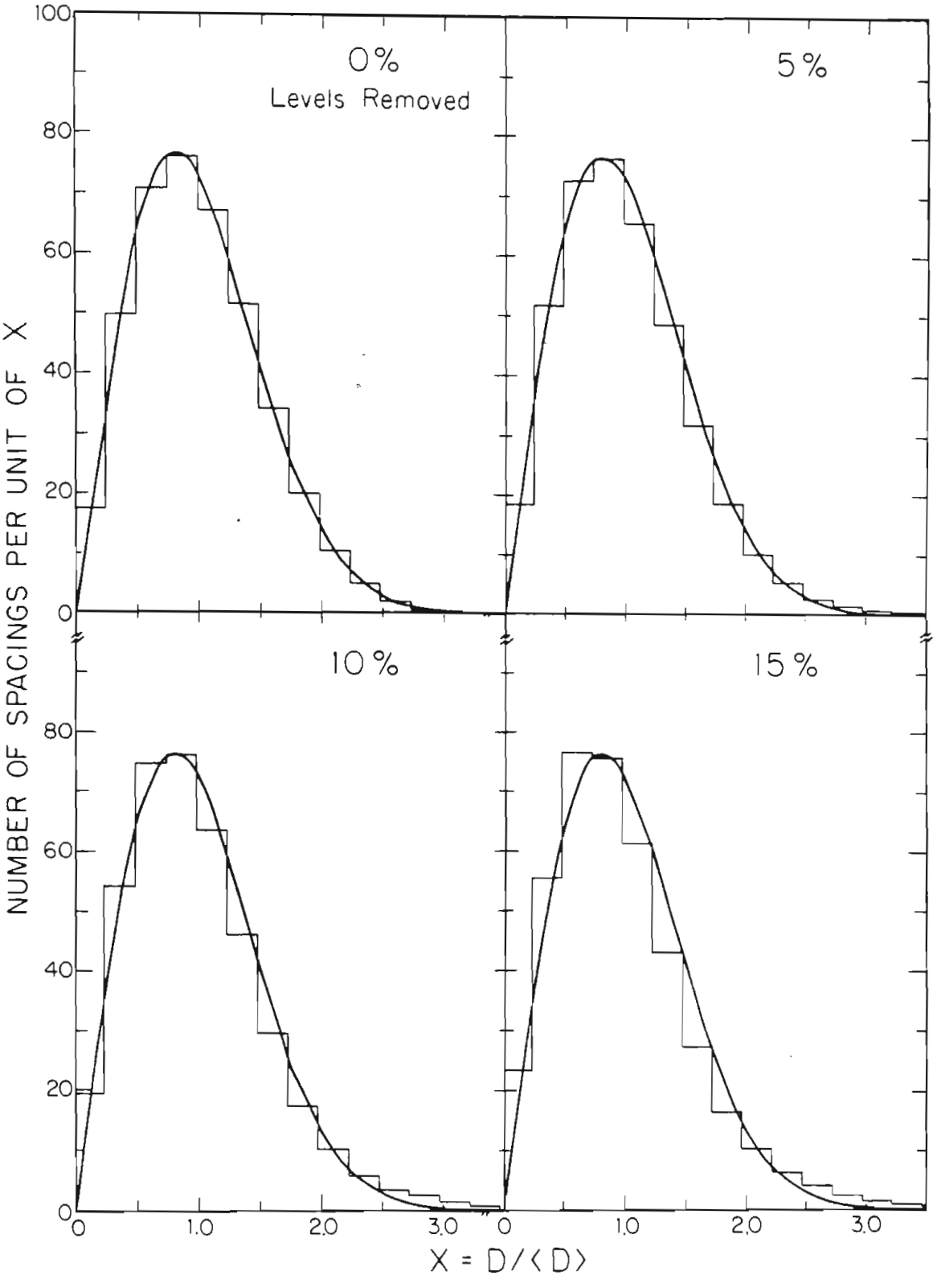
0%
Levels Removed
5%
10%
15%
NUMBER OF SPACINGS PER UNIT OF X
X = D/⟨D⟩
0
20
40
60
80
100
1.0
2.0
3.0

Figure 4.10 Simulation of the Effects of Missing 20% to 35% of the Resonances on the Wigner Distribution.

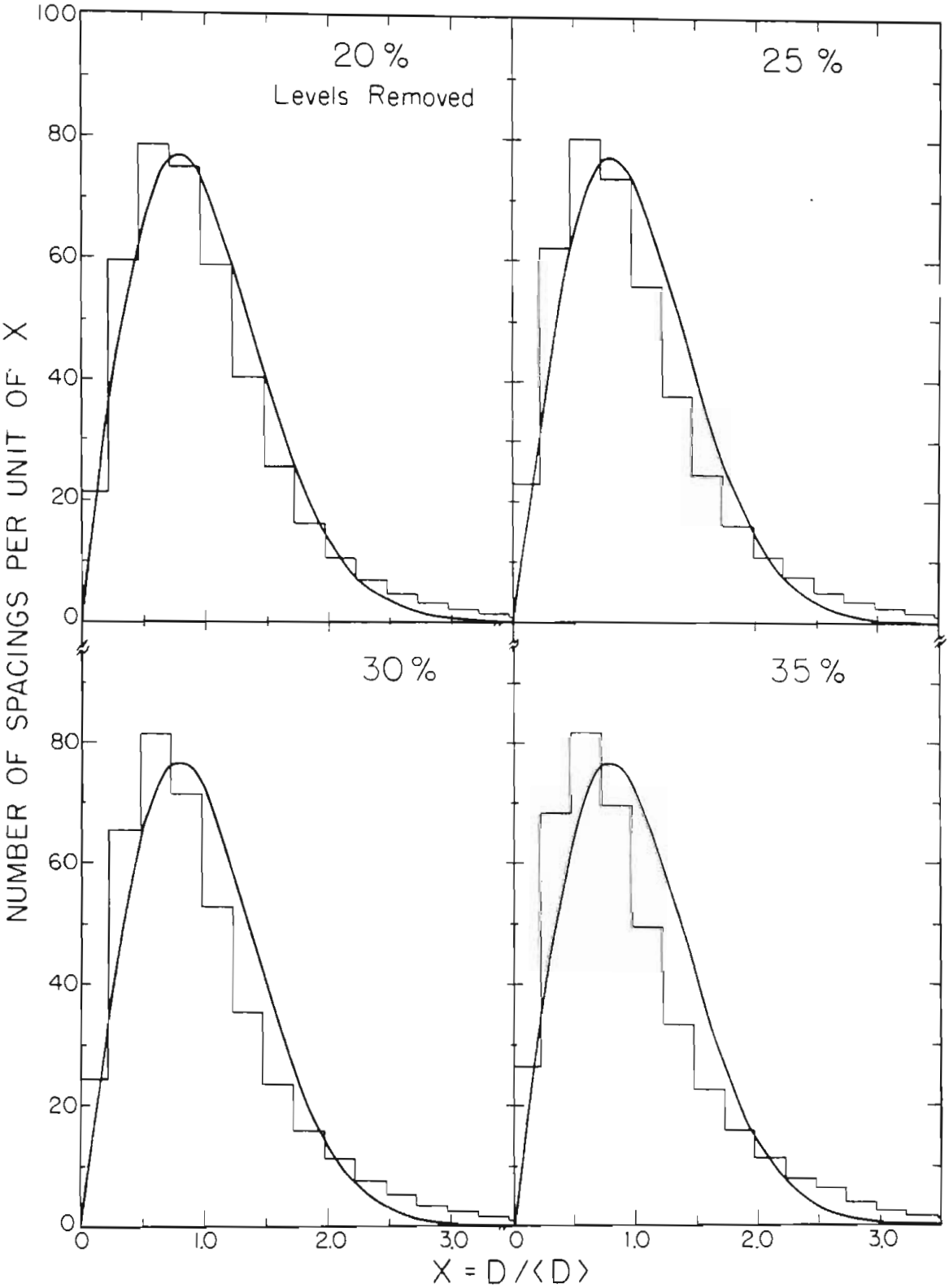
20 %
Levels Removed
25 %
30 %
35 %
NUMBER OF SPACINGS PER UNIT OF X
X = D/⟨D⟩
0
20
40
60
80
100
1.0
2.0
3.0

Figure 4.11 Simulation of the Effects of Missing 40% to 55% of the Resonances on the Wigner Distribution.

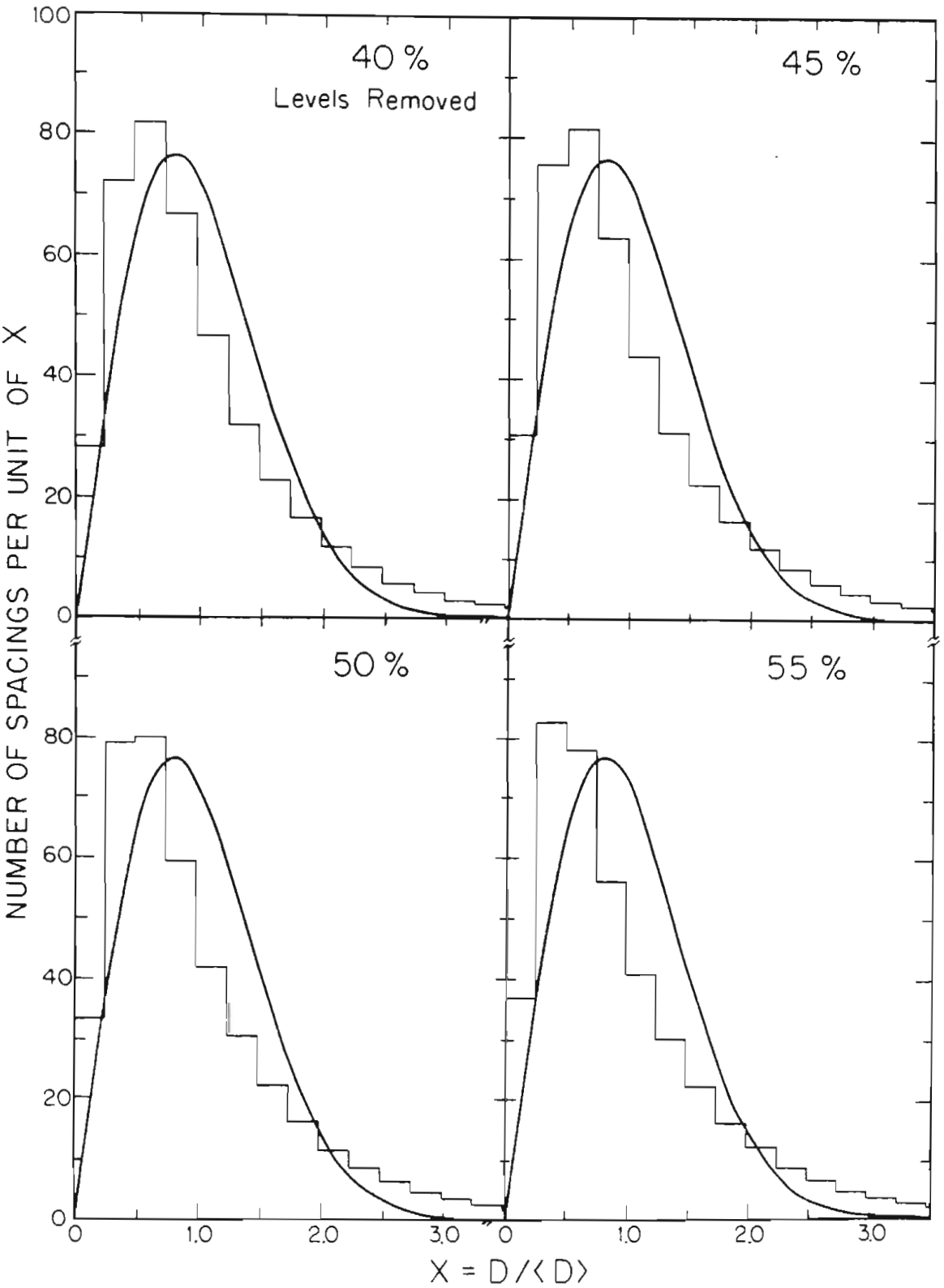
40 %
Levels Removed
45 %
50 %
55 %
NUMBER OF SPACINGS PER UNIT OF X
X = D/⟨D⟩
0
20
40
60
80
100
1.0
2.0
3.0

Figure 4.12 Simulation of the Effects of Missing 60% to 75% of the Resonance on the Wigner Distribution.

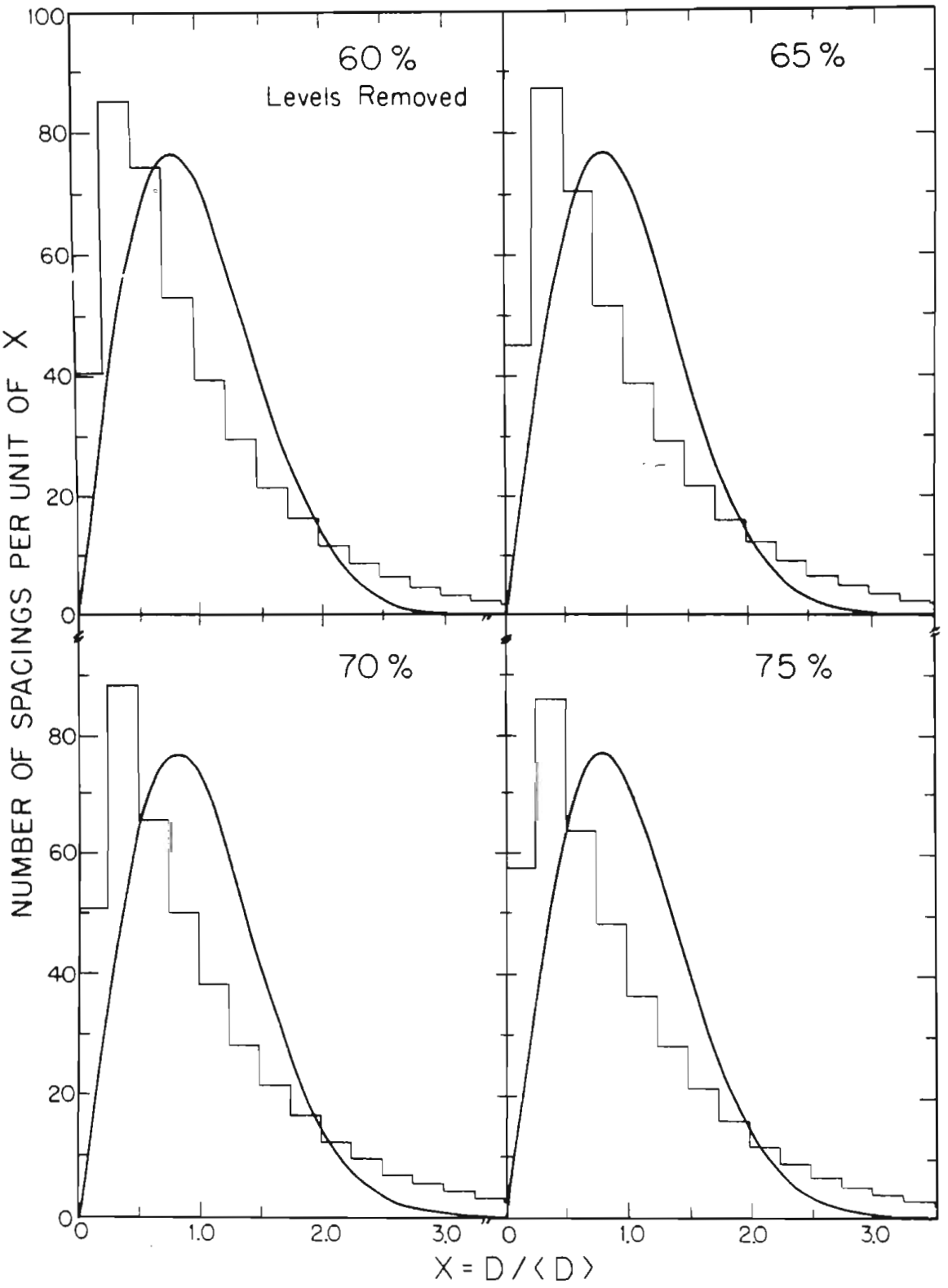
60 %
Levels Removed
65 %
70 %
75 %
NUMBER OF SPACINGS PER UNIT OF X
X = D / ⟨ D ⟩
0
20
40
60
80
100
1.0
2.0
3.0

Figure 4.13 Simulation of the Effects of Missing 80% to 95% of the Resonances on the Wigner Distribution.

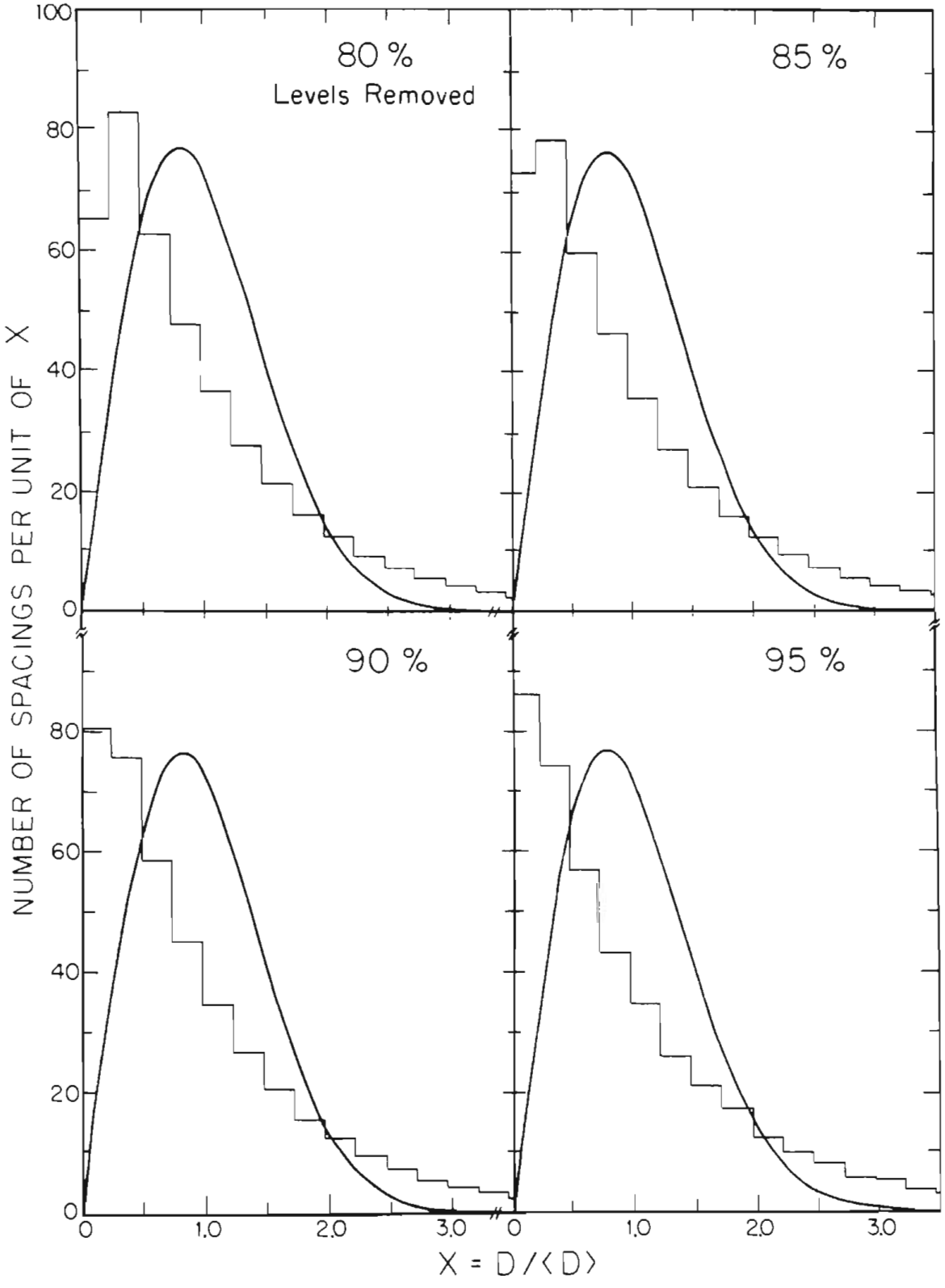
80 %
Levels Removed
85 %
90 %
95 %
NUMBER OF SPACINGS PER UNIT OF X
X = D/⟨D⟩
0
20
40
60
80
100
1.0
2.0
3.0

definition. These calculations and the visual comparisons indicate that 50% of the levels were missed in ^{65}Ga and that an average of 70% of the levels were missed in ^{67}Ga over the entire energy range. The indication for the upper 51 s-wave resonances in ^{67}Ga is that 30% of the resonances were missed. Therefore, the upper half of the s-wave resonances are used for further analysis instead of the entire energy range. The error in the number of missed levels is very difficult to determine. However, the number of missed levels in ^{65}Ga is believed to be between 40% and 60%, and the number of missed levels in ^{67}Ga is believed to be between 60% and 80% over the entire energy range. Also, the number of missed levels in the region of the upper 51 s-wave resonances is believed to be between 20% to 40%. The spacing distributions for the higher angular momenta were not considered, since except for analog states very few p-wave resonances or d-wave resonances were observed in either experiment.

4.3 Reduced Width Distributions

The distribution of reduced widths is expected to be characterized by the Porter-Thomas distribution

$$P(Y)\,dY = 1/(2\pi Y)^{1/2}\ \exp(-Y/2)\,dY$$

where $Y = \gamma^2/\langle\gamma^2\rangle$, γ^2 is the reduced width for a particular level, and $\langle\gamma^2\rangle$ is the average reduced width. This distribution was derived by Porter and Thomas(1956) assuming that the distribution of reduced width amplitudes is Gaussian. Since the reduced width is the square of the reduced width amplitude, the above equation follows immediately. The reduced width distributions for l-values higher than zero are not discussed since very few resonances were observed with l greater than zero excluding analog states.

The reduced width distribution for ^{65}Ga is shown in Figure 4.14. The solid line is the Porter-Thomas distribution normalized to 32 reduced widths. The Porter-Thomas distribution is plotted in this manner in order to emphasize the effect of missing small resonances. No resonances were seen below the cutoff of Y=0.3, and the histogram is above the Porter-Thomas distribution for Y between 0.3 and 3. Also, there are no resonances observed

Figure 4.14 Reduced Width Distribution for ^{65}Ga. The solid line is the Porter-Thomas distribution normalized to 32 reduced widths.

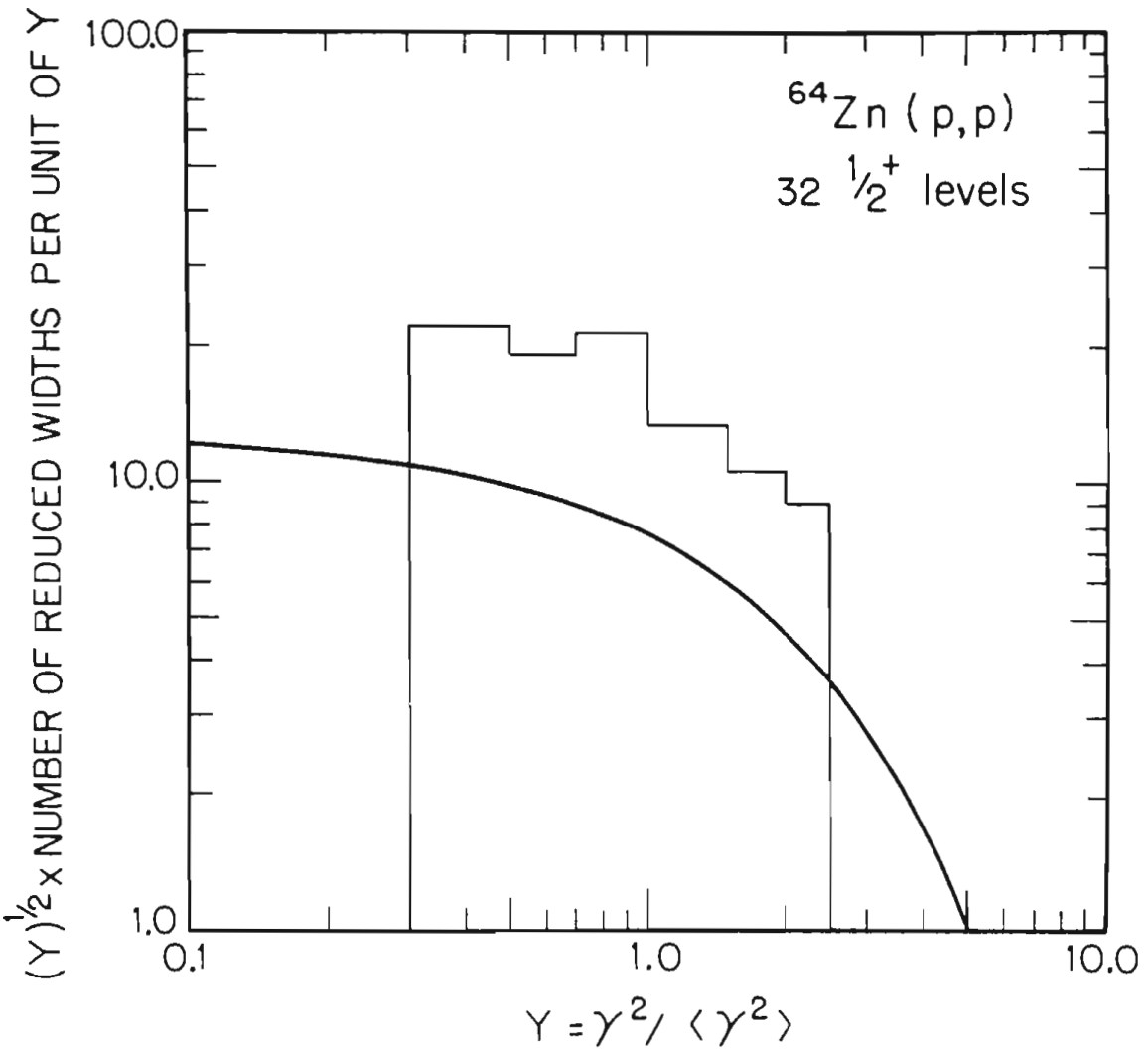
100.0
10.0
1.0
0.1
1.0
10.0
^{64}Zn (p,p)
32 $\frac{1}{2}^+$ levels
$(Y)^{1/2}$ x NUMBER OF REDUCED WIDTHS PER UNIT OF Y
$Y = \gamma^2 / \langle \gamma^2 \rangle$

for Y greater than 3.

For the $^{66}Zn(p,p)$ experiment, the reduced width distribution is shown in Figure 4.15. The solid line is the Porter-Thomas distribution normalized to 102 reduced widths. No resonances were observed whose reduced width was such that the corresponding value of Y is below the cutoff of Y=0.15. The histogram is above the Porter-Thomas distribution for Y between 0.15 and 2.0, and for Y greater than 2.0, the histogram is below the normalized distribution. The reduced width distribution for the upper 51 s-wave resonances in ^{67}Ga is shown in Figure 4.16. The solid line is the Porter-Thomas distribution normalized to 51 reduced widths. Again, no resonances were observed below the cutoff of Y=0.2, and for Y greater than 3.0. For Y between 0.2 and 2.0, the histogram is above the normalized Porter-Thomas distribution.

These differences between the histogram and the Porter-Thomas distribution for ^{65}Ga and ^{67}Ga are also due to the effects of missing small resonances. A computer simulation was written to test this hypothesis. The procedure used to generate random numbers from the Porter-Thomas distribution was the acceptance-rejection method. First, a pair of random numbers, r and s, are generated from a Gaussian distribution. A Gaussian distribution is used since the maximum of the Porter-Thomas distribution is infinity, which meant that the acceptance-rejection

Figure 4.15 Reduced Width Distribution for ^{67}Ga. The solid line is the Porter-Thomas distribution normalized to 102 reduced widths.

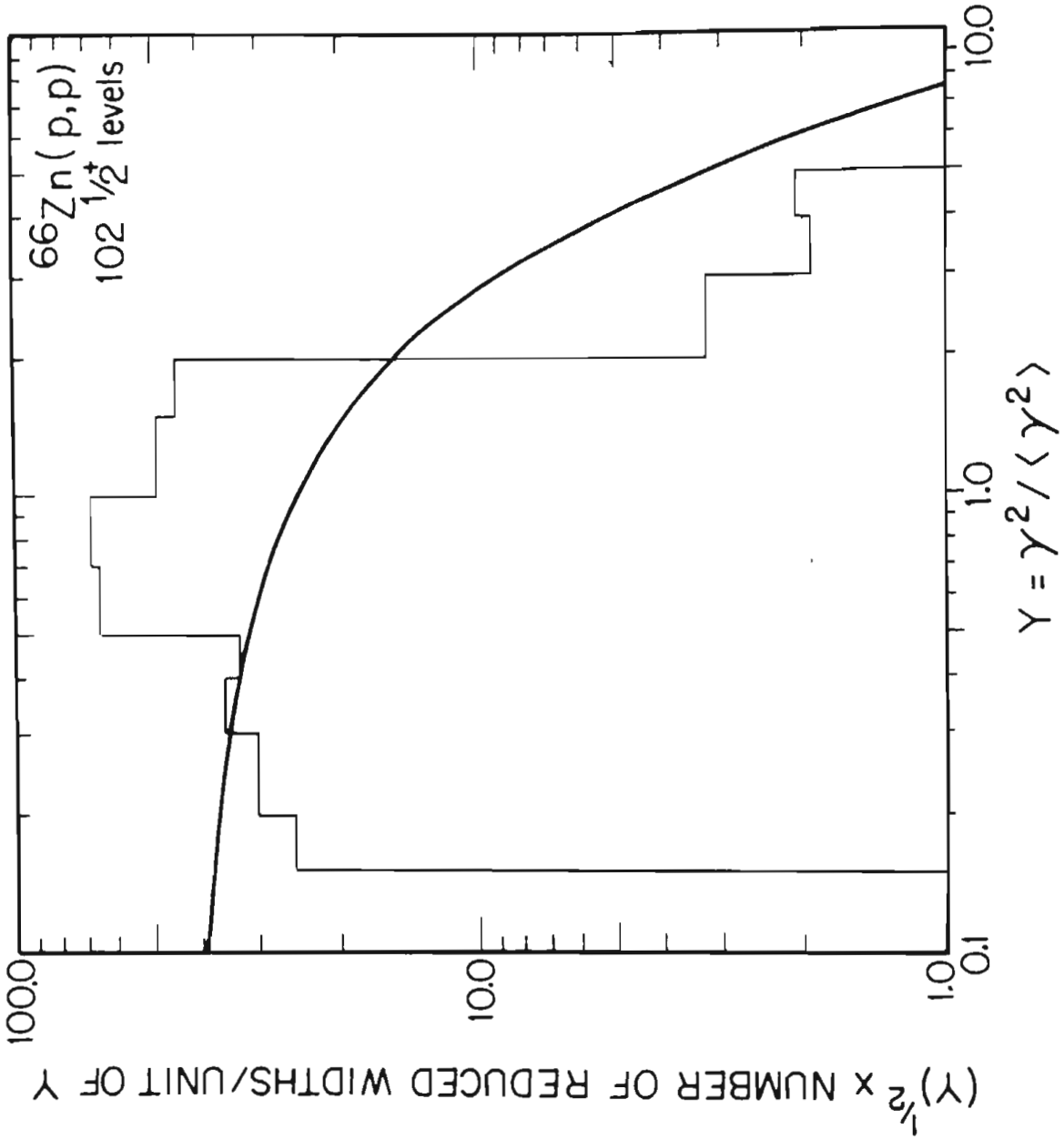
$^{66}Zn(p,p)$
102 $1/2^+$ levels
100.0
10.0
1.0
0.1
10.0
1.0
$(\gamma)^{1/2}$ x NUMBER OF REDUCED WIDTHS/UNIT OF γ
$Y = \gamma^2 / \langle \gamma^2 \rangle$

Figure 4.16 Reduced Width Distribution for the Upper 51 1/2+ Resonances in ^{67}Ga. The solid line is the Porter-Thomas distribution normalized to 51 reduced widths.

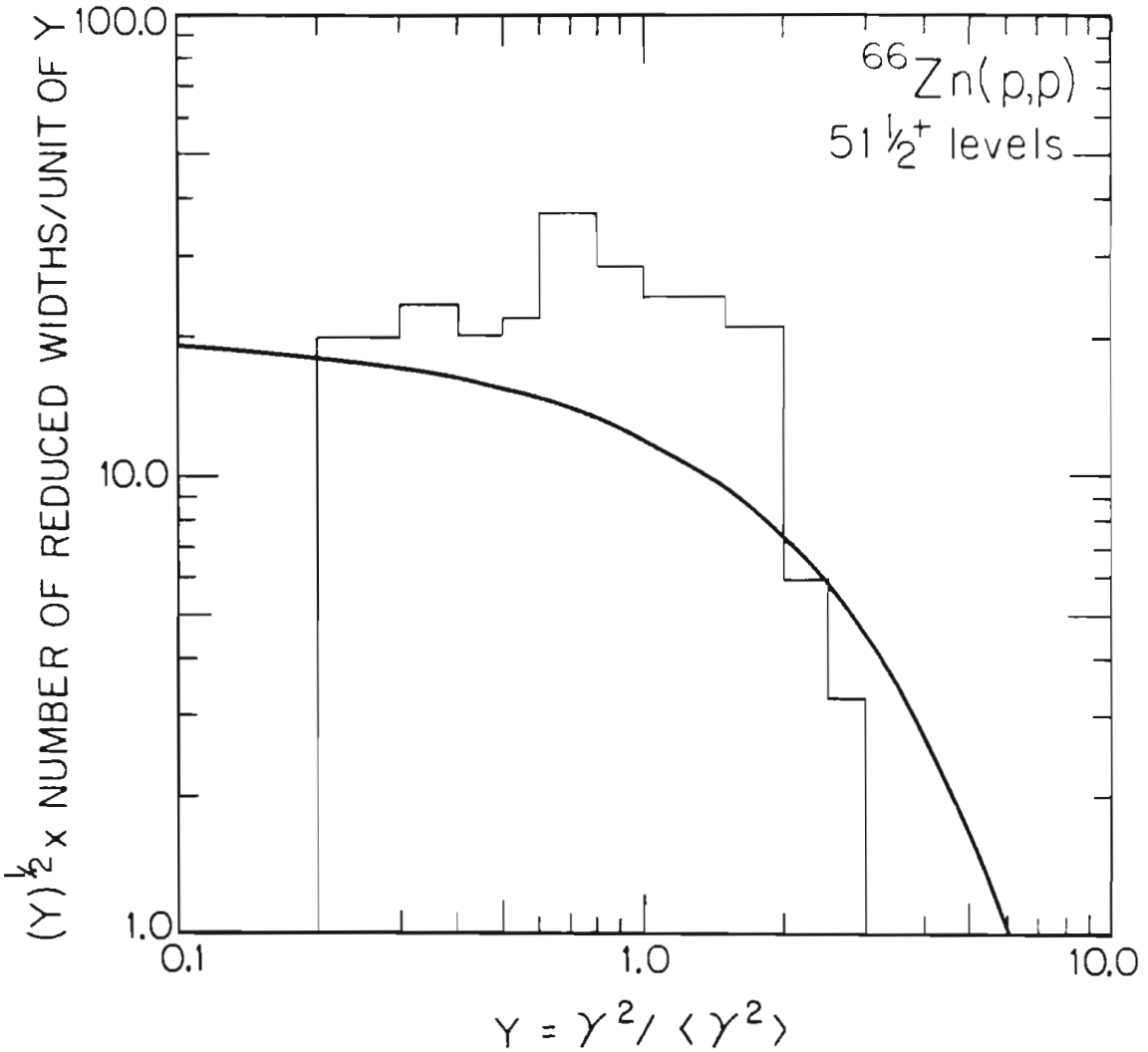
^{66}Zn(p,p)
51 ½$^{+}$ levels
100.0
10.0
1.0
0.1
1.0
10.0
$(Y)^{\frac{1}{2}}$ x NUMBER OF REDUCED WIDTHS/UNIT OF Y
$Y = \gamma^2 / \langle \gamma^2 \rangle$

method could not be used. However, the Porter-Thomas random numbers can be obtained, since the square of the Gaussian random numbers are distributed according to the Porter-Thomas distribution. Second, the finite domain between 0 and 10 is chosen for the distribution since the probability of any values of Y greater than 10 is very small. Third, the probability for X=10*s is divided by the maximum probability of the Gaussian distribution, and this ratio is then compared to r. If r is less than this ratio, then chose X as a reduced width. This procedure was followed until 500,000 widths were generated.

In order to simulate the effect of missing small resonances, the matrix of the reduced widths was sorted into descending order. The average value of the reduced widths is calculated neglecting the last 5% of the reduced width matrix. The dimensionless parameter, Y, is then calculated using this new value for the average of the reduced widths. These results are plotted and represent the effect of missing 5% of the smallest reduced widths. This procedure is repeated neglecting an additional 5% of the smallest reduced widths. These results reflect the effect of missing 10% of the smallest reduced widths. This procedure is followed until only 5% of the largest reduced widths remain. The modified distributions calculated from this procedure are shown in Figures 4.17 to 4.21. The histograms and the Porter-Thomas

Figure 4.17 Simulation of the Effects of Missing 0% to 15% of the Resonances on the Porter-Thomas Distribution.

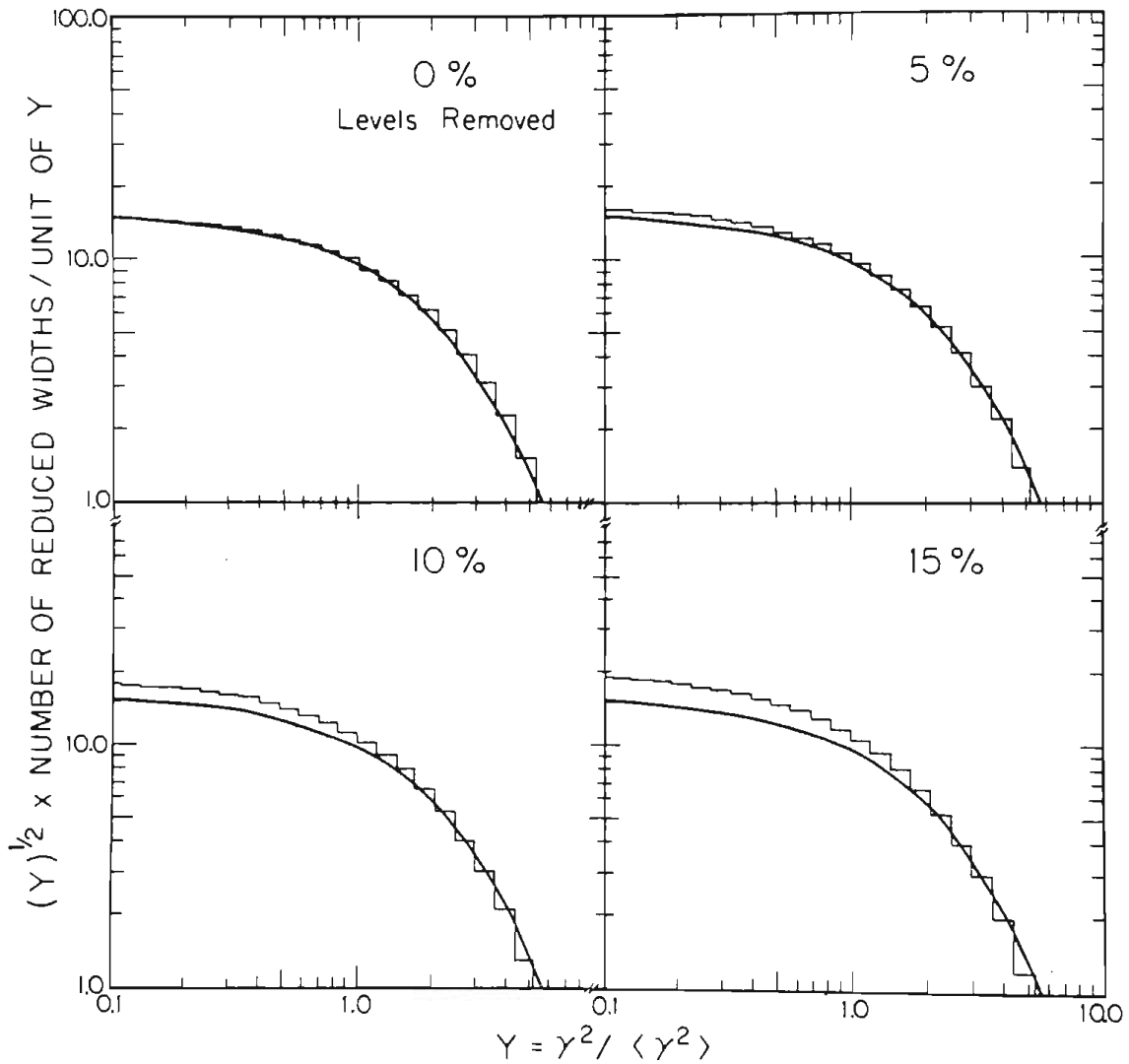
0 %
Levels Removed
5 %
10 %
15 %
100.0
10.0
1.0
10.0
1.0
0.1
1.0
0.1
1.0
10.0
(Y)^1/2 x NUMBER OF REDUCED WIDTHS / UNIT OF Y
Y = γ²/ ⟨γ²⟩

Figure 4.18 Simulation of the Effects of Missing 20% to 35% of the Resonances on the Porter-Thomas Distribution.

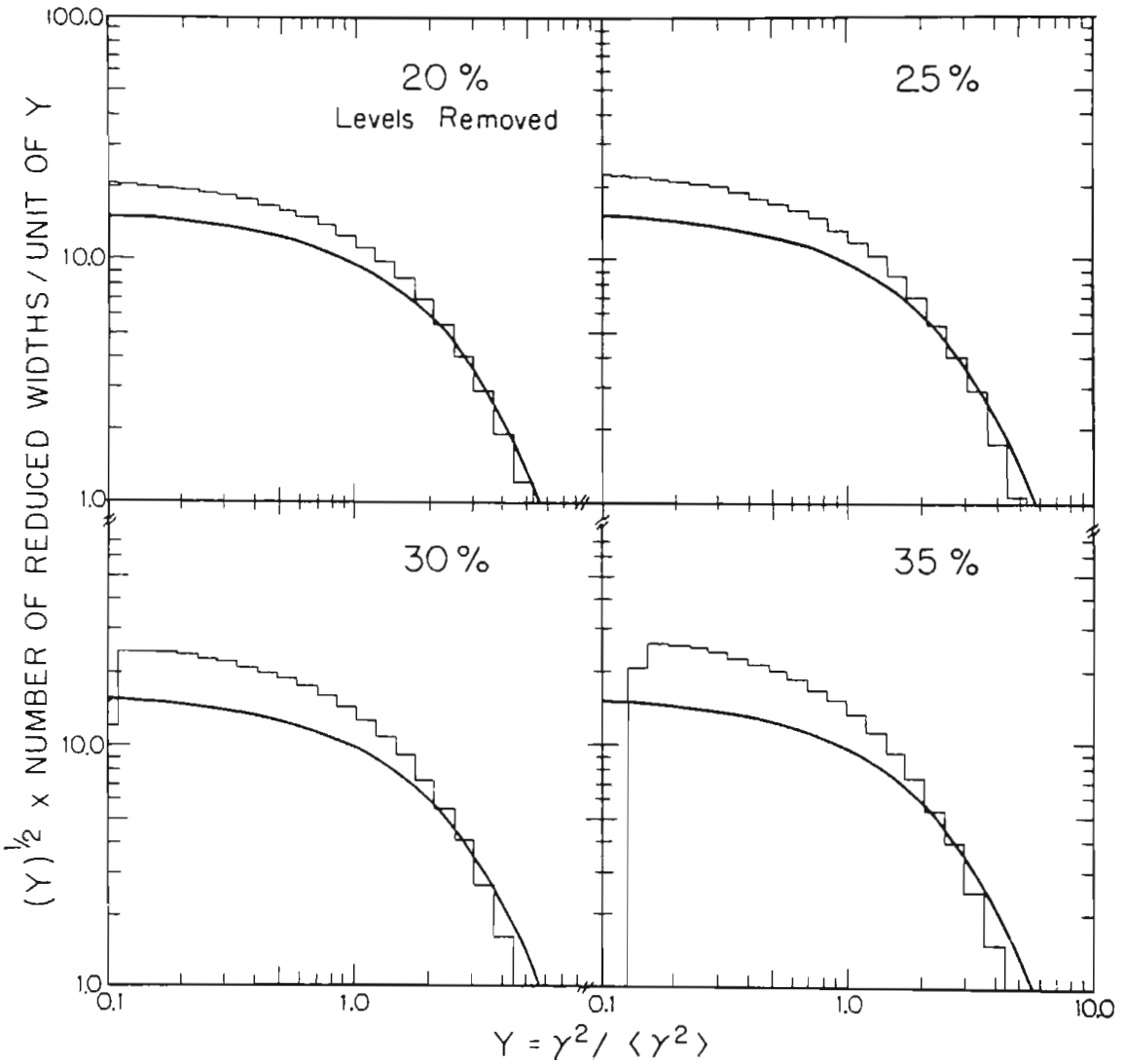
20 %
Levels Removed
25 %
30 %
35 %
100.0
10.0
1.0
0.1
1.0
10.0
(Y)^1/2 x NUMBER OF REDUCED WIDTHS / UNIT OF Y
Y = γ²/ ⟨γ²⟩

Figure 4.19 Simulation of the Effects of Missing 40% to 55% of the Resonances on the Porter-Thomas distribution.

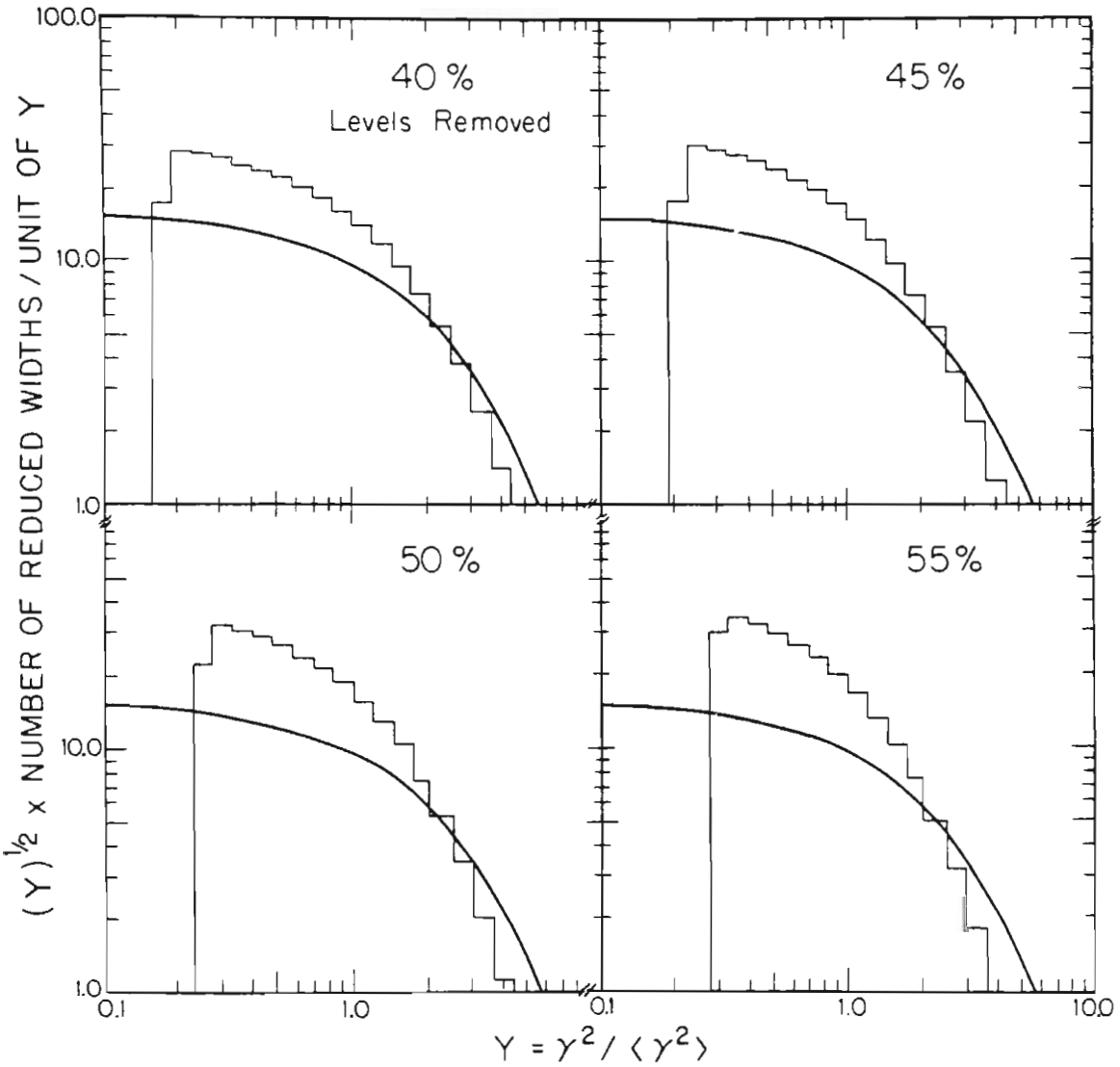
40 %
Levels Removed
45 %
50 %
55 %
100.0
10.0
1.0
0.1
1.0
10.0
$(Y)^{1/2}$ x NUMBER OF REDUCED WIDTHS / UNIT OF Y
$Y = \gamma^2 / \langle \gamma^2 \rangle$

Figure 4.20 Simulation of the Effects of Missing 60% to 75% of the Resonances on the Porter-Thomas Distribution.

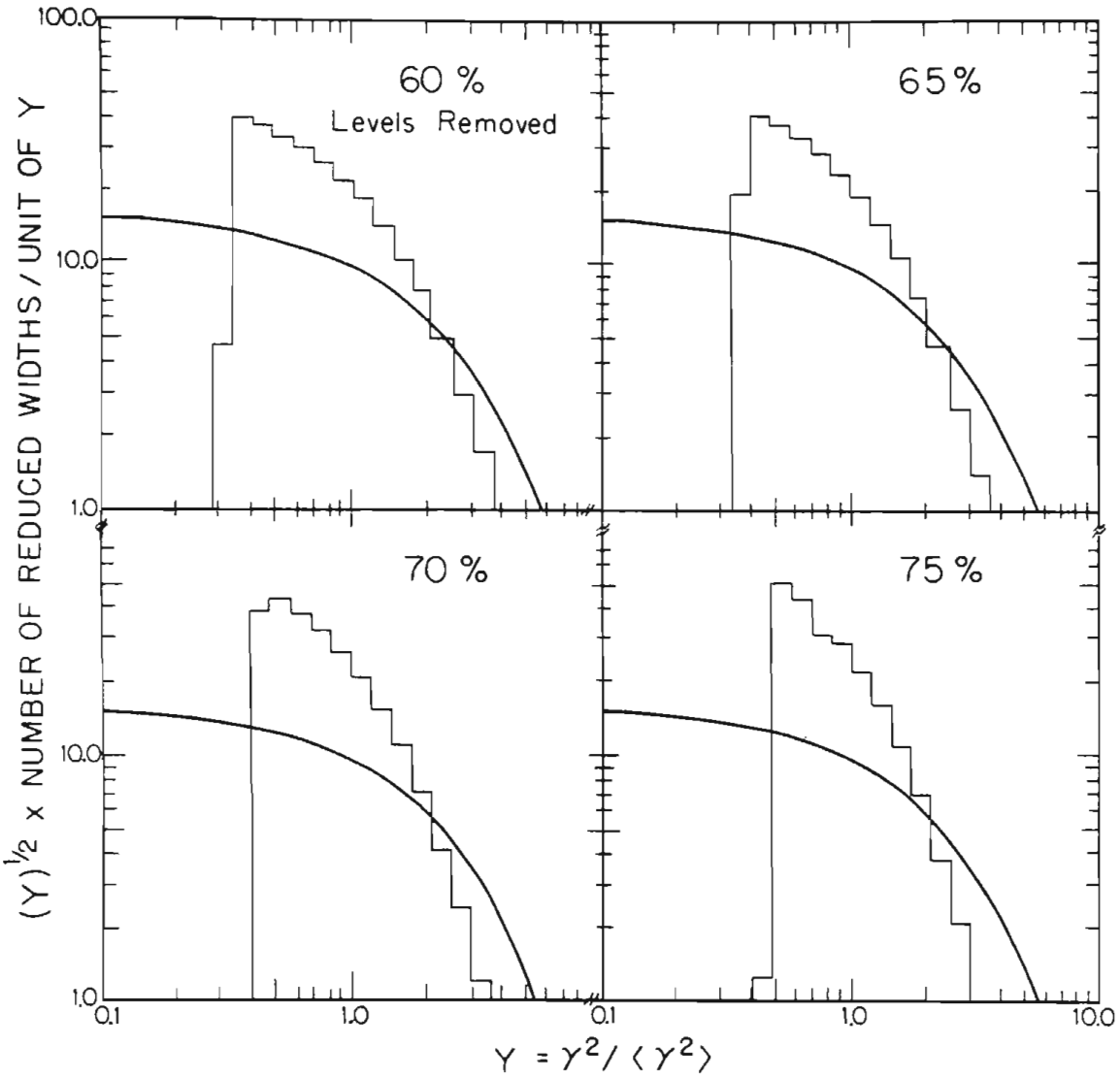
60 %
Levels Removed
65 %
70 %
75 %
100.0
10.0
1.0
0.1
1.0
10.0
(Y)^1/2 x NUMBER OF REDUCED WIDTHS / UNIT OF Y
Y = γ²/⟨γ²⟩

Figure 4.21 Simulation of the Effects of Missing 80% to 95% of the Resonances on the Porter-Thomas Distribution.

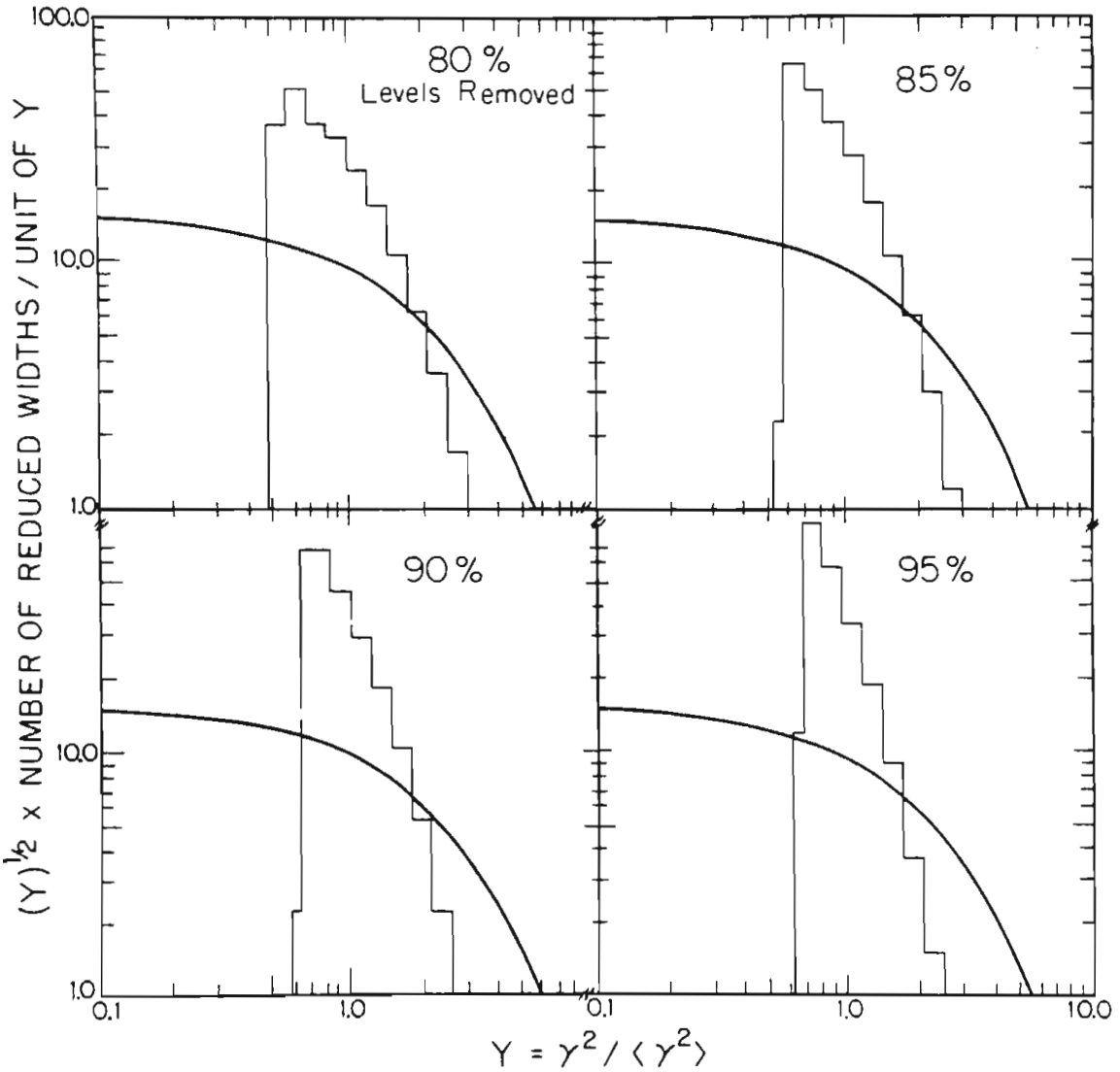
80 %
Levels Removed
85%
90%
95%
100.0
10.0
1.0
0.1
1.0
10.0
(Y)^½ x NUMBER OF REDUCED WIDTHS / UNIT OF Y
Y = γ² / ⟨γ²⟩

distribution are normalized to 40 reduced widths.

The comparison between the modified Porter-Thomas distributions and the reduced width distributions for ^{65}Ga and ^{67}Ga indicate that the data show the effect of missing small resonances. However, it is difficult to make an exact comparison in order to determine the number of missed resonances. A visual comparison indicates that the results for the reduced width distributions agree with the results obtained from Section 4.2 for the spacing distributions. That is, 50% of the resonances were missed in ^{65}Ga, and that 70% of the resonances were missed in ^{67}Ga over the entire energy range. For the upper 51 s-wave resonances in ^{67}Ga, the comparison indicates that approximately 30% to 40% of the resonances were missed.

A more quantitative check is to compare the lowest observed value of Y for the modified Porter-Thomas distributions with the reduced width distributions for ^{65}Ga and ^{67}Ga. For the $^{64}Zn(p,p)$ experiment, the data histogram has a sharp cutoff at Y=0.3. The modified Porter-Thomas distributions for missing 50% to 60% of the levels have a cutoff for Y between 0.28 and 0.33. This result is in good agreement with the value of missing 50% of the levels obtained from a comparison of the spacing distributions.

For the $^{66}Zn(p,p)$ experiment, the data histogram does not have a sharp cutoff for small Y. However, the data

histogram first drops below the normalized Porter-Thomas distribution for Y approximately equal to 0.4. A comparison with the modified Porter-Thomas for cutoff values of Y between 0.33 and 0.48 corresponds to missing between 65% and 75% of the levels. Again, this result is in good agreement with the result of 70% obtained from the comparison with the spacing distributions. The comparison of the reduced width distribution for the upper 51 resonances in ^{67}Ga indicates that approximately 40% of the resonances were missed. This result is slightly higher than the result of 30% obtained from the comparison of the spacing distributions, but the two results are in overall agreement.

In summary, a comparison of the spacing and reduced width distributions of the data with the modified Wigner and Porter-Thomas distributions are useful in determining the number of resonances missed in ^{65}Ga and ^{67}Ga.

4.4 Level Densities

The s-wave level densities for ^{65}Ga and ^{67}Ga were compared with the predictions obtained from a nuclear-level density formula by Gilbert and Cameron(1965). In their method, a "constant nuclear temperature" representation of nuclear level densities is used for low excitation energies. The computer program using this formula was transferred from the TUCC computer to the in-house Prime 300 computer.

For s-wave resonances, Table 4.1 shows the results for ^{65}Ga and ^{67}Ga for energies between E_p = 2.50 and 3.50 MeV. The values of the level density or equivalently the level spacing change by a factor of two over this energy range.

The observed level spacing for ^{65}Ga was 23.1 keV. If this value is corrected for missing approximately 50% of the resonances, then the corrected level spacing is approximately 12 keV. Referring to Table 4.1, the uncorrected level spacing is approximately 26% greater than the predicted level spacing for E_p= 3.00 MeV, while the corrected level spacing is approximately 34% smaller than the level spacing at E_p = 3.00 MeV. Therefore, the

Table 4.1 $1/2^+$ Level Densities for ^{65}Ga and ^{67}Ga

Energy of Incident Proton	Level Density Per MeV	Energy Spacing In keV
^{65}Ga		
2.50	34.99	28.58
2.75	43.80	22.83
3.00	54.65	18.30
3.25	67.99	14.71
3.50	84.35	11.86
^{67}Ga		
2.50	205.48	4.87
2.75	257.67	3.88
3.00	322.19	3.11
3.25	401.73	2.49
3.50	499.60	2.00

level spacing for ^{65}Ga seems in qualitative agreement with the predicted value.

For the ^{66}Zn(p,p) experiment, the observed level spacing for s-wave resonances is 6.5 keV. The corrected level spacing is approximately 2.2 keV, assuming that 70% of the resonances were missed. Again, by referring to Table 4.1, the corrected level spacing is in qualitative agreement with the expected value.

The predictions of the level density code are also of value in understanding the relative number of resonances missed in ^{65}Ga and ^{67}Ga. More small resonances were missed in ^{67}Ga than in ^{65}Ga, even though the ^{67}Ga experiment was performed with better overall energy resolution than was the ^{65}Ga experiment. This is reasonable since approximately the same amount of s-wave strength is divided into many more levels in ^{67}Ga than in ^{65}Ga. Table 4.1 indicates that the level spacing in ^{67}Ga is approximately 3.11 keV at E_p=3.00, which is six times smaller than the level spacing in ^{65}Ga. The average reduced width in ^{67}Ga is therefore six times smaller than in ^{65}Ga.

If one assumes the value of 0.05 for the s-wave strength function for ^{64}Zn over the energy range of 2.50 to 3.24 MeV and the value of 18.3 keV for the average level spacing for s-wave resonances, then the average reduced width is 0.915 keV. The penetrability for a

laboratory energy of 3.0 MeV is 0.045, which from the expression $\Gamma = 2P\gamma^2$, corresponds to an average laboratory width of 82 eV for 1/2+ resonances. The smallest observed laboratory width in ^{65}Ga was 25 eV which is at least a factor of three smaller than the "theoretical prediction" for the average laboratory width. The ratio of the smallest observed laboratory width and the predicted average laboratory width is approximately 0.3. By integrating the Porter-Thomas distribution from Y=0 to Y=0.3, the value of 40% is obtained for the number of resonances which are expected to be missed. This "predicted value" is in good agreement with the result of 50% obtained by an examination of the spacing and reduced width distributions.

For ^{67}Ga, the value of 0.05 for the s-wave strength function and the value of 3.11 keV for the average level spacing together yield 0.156 keV for the average reduced width, and 14.0 eV for the average laboratory width. The smallest observed laboratory width in ^{67}Ga was 8 eV. The smallest observed laboratory widths have close to the same value as the "theoretical prediction" for the average laboratory width. With these values for the predicted average laboratory width and the smallest observed laboratory width, the integral of the Porter-Thomas distribution indicates that approximately 60% of the resonances are expected to be missed. Again, this

"predicted value" is in good agreement with the value of 70% obtained from a comparison of the spacing and reduced width distributions.

These considerations explain why a higher precentage of the resonances were observed in ^{65}Ga than in ^{67}Ga. For ^{65}Ga, the smallest observed laboratory width is a factor of three smaller than the predicted average laboratory width, so that many resonances were observed below this average value. However, for ^{67}Ga, the smallest observed laboratory widths have nearly the same value as the predicted average laboratory width, almost all the resonances below this average value were missed.

4.5 Analog States

4.5.1 Theory of Analog States

Fragmented analog states are single, special resonances which have been mixed with nearby background states enhancing the widths of these background states. Analog states are generally observed as anomalies in the elastic cross section. These special states in the daughter nucleus with (Z+1) protons and N neutrons are

related to the low-lying bound states of a parent nucleus with Z protons and (N+1) neutrons. Both the daughter and parent nucleus have A nucleons. In other words, as compared to the parent state, the analog state has one neutron transformed into a proton. If the nuclear force is charge independent, then the major difference between the daughter and parent state is the energy difference due to the Coulomb energy of the extra proton, and the neutron-proton mass difference. This energy relationship between parent state and analog state is shown in Figure 4.22, where ΔE_c is the Coulomb energy of the extra proton, δ is the neutron-proton mass difference, B_n is the binding energy of the last neutron in the parent nucleus, E_x is the parent state excitation energy. and E_p^{cm} is the center of mass energy of the incident proton required to form the analog of the excited state in the parent nucleus.

The relation between these quantities is obtained from inspection of Figure 4.14

$$E_p^{cm} = \Delta E_c - B_n + E_x$$

The binding energy of the last neutron in the parent nucleus and the excitation energy are experimentaly known quantities. The Coulomb energy difference can be estimated from a semi-empirical formula by Janecke(1969)

$$\Delta E_c = [C_1 Z - C_2]/A^{1/3} \text{ keV}$$

where A is the mass of the parent or analog system, Z is the number of protons of the target, C_1 = 1389, and C_2 =

Figure 4.22 Energy Level Diagram Showing the Relationship Between the Analog State and the Parent State.

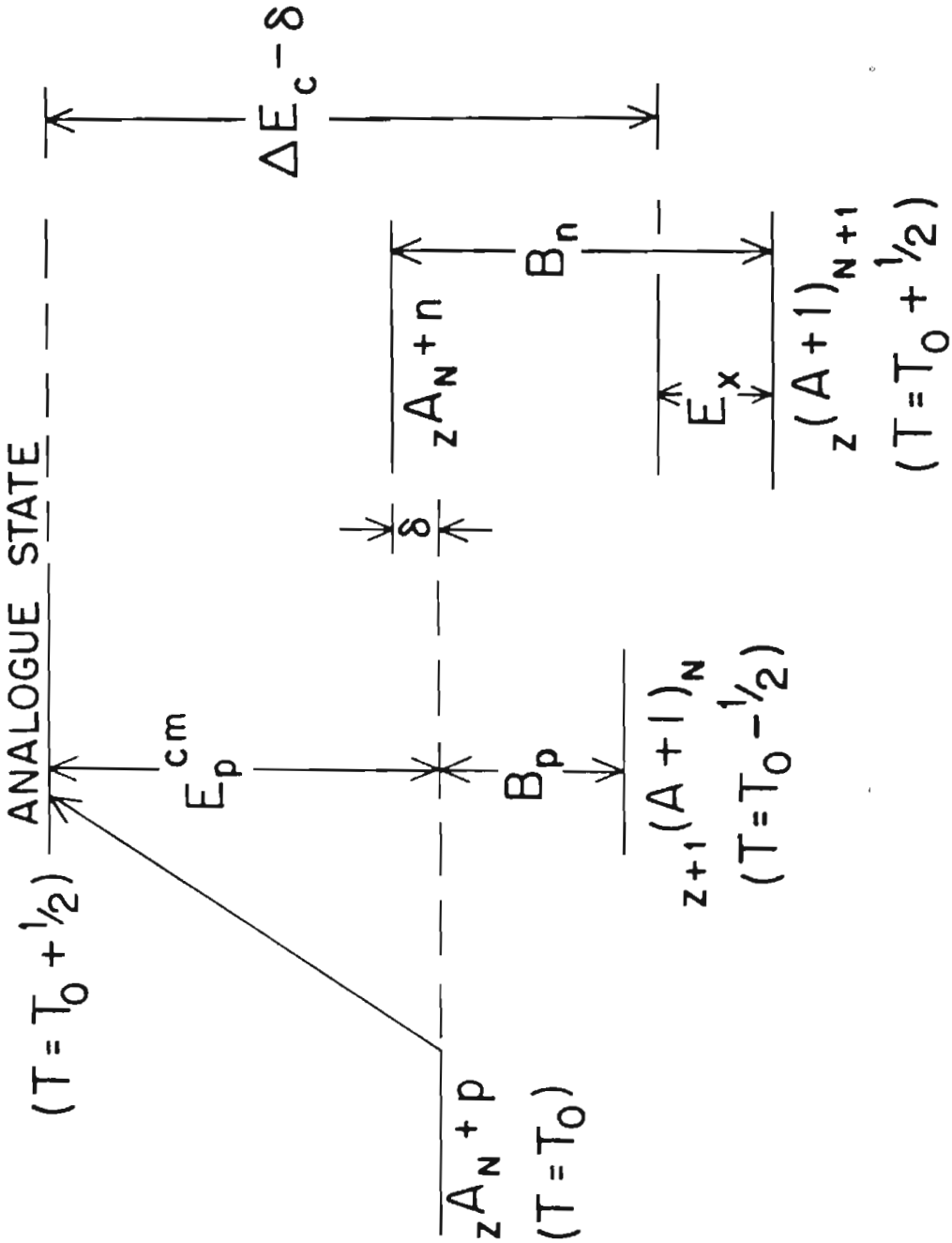

δ = neutron proton mass difference

2041. These values for C_1 and C_2 give reasonable agreement for the Ti, Cr, Fe, and Ni isotopes(Bilpuch et al, 1976). The error between the Coulomb energies estimated from the Jänecke formula and the experimentally determined Coulomb energies is about 35 keV for these isotopes.

Several theories have been presented for analog states. The first explanation was given by Robson(1965), where he assumed that the mixing due to the Coulomb force between the analog state and the background states for elastic scattering took place outside of the nucleus. This work by Robson was later extended by Mello(1967). Other theories by Fallieros(1966), Mekjian and MacDonald(1968), and Mahaux and Weidenmüller(1969) were based on a shell model theory. Stephen(1967) and De Toledo Piza and Kerman(1967,1968) developed models based on the Feshbach projection operator formalism. Lane(1969) considered the fine structure of analog states as a special case of line broadening. The most complete list of references is given in the compilation by Wilkinson(1969).

The theory developed by Lane was used to analyze the fine structure of the analog states in these experiments. Lane describes the effects on the background states due to the presence of a special state where the special state has a very large reduced width in one or more channels.

This special state or analog state is not an eigenstate of the actual Hamiltonian of the system, but is an eigenstate of the Hamiltonian with the Coulomb force neglected. The effect of the Coulomb force is to mix the analog state with the background states of the same spin and parity. Therefore, one observes a distribution of fragmented resonances instead of a single analog state. Lane describes the effects of strong or weak mixing on the distribution of the analog strength. In the strong mixing case, the analog state is completely dissolved among the background states. In the case of weak mixing, one level contains most of the strength and the background states are not strongly enhanced. The equation describing the fine structure distribution for strong mixing is given by,

$$S(E) = s_o - \frac{(2s_o \Delta)(E_A - E)}{(E_A - E)^2 + W_o^2/4} + \frac{\gamma_A^2 W_o/2\pi}{(E_A - E)^2 + W_o^2/4}$$

where E_A is the analog state energy, Δ is the asymmetry parameter, s_o is the background strength function, γ_A^2 is the reduced width of the analog state, and W_o is the spreading width. A derivation of this result is given by Lane(1969,1974).

For the weak mixing case, the above equation is still used, but S(E) must be reinterpreted(Bilpuch et al,1976). It is also more convenient to use the integral of the above equation and compare the resulting equation with the

cumulative sum of the reduced widths of the fragmented analog state. The result is

$$\int S(E)\,dE = s_o E + s_o \Delta \ln[(E_A - E)^2 + W_o^2/4] + (\gamma_A^2/\pi)\tan^{-1}[(E_A - E)/(W_o/2)]$$

The fine structure distributions of the analog states observed in these experiments were fit with this equation.

4.5.2 Identification of Analog States

The sixth, seventh, and thirteenth excited states in the parent nucleus, ^{65}Zn, were observed as analog states in the daughter nucleus, ^{65}Ga. The energy level diagram for the isobaric pair, ^{65}Zn - ^{65}Ga, is shown in Figure 4.23. The energy levels in the parent nucleus, ^{65}Zn, were translated by an amount, $\Delta E_c - \delta$, to facilitate comparison with the energy levels in the daughter nucleus. This figure also shows that the binding energy of the last proton in ^{65}Zn is 3.938 MeV, and that the analog state corresponding to the ground state in ^{65}Zn would occur at an excitation energy of 5.780 MeV in the daughter nucleus. The (d,p) spectroscopic data are also shown in this figure. Of the four resonances which were observed in the (d,p) studies, only one was not observed as an analog

Figure 4.23 The ^{65}Zn - ^{65}Ga Isobaric Pair. Three of the ten possible analog states were observed in this experiment.

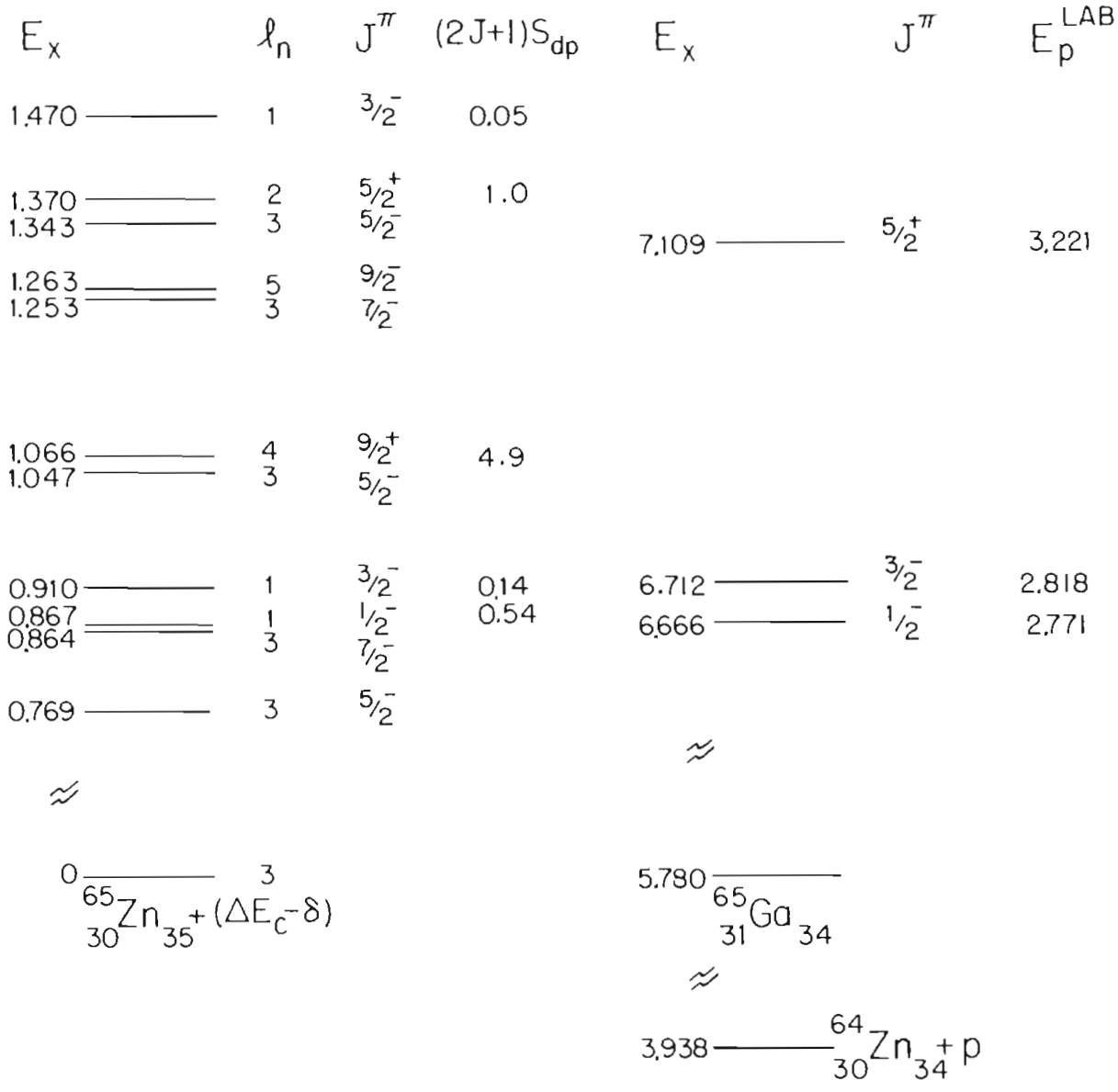
E_x
ℓ_n
J^π
$(2J+1)S_{dp}$
1.470
1
$3/2^-$
0.05
1.370
2
$5/2^+$
1.0
1.343
3
$5/2^-$
1.263
5
$9/2^-$
1.253
3
$7/2^-$
1.066
4
$9/2^+$
4.9
1.047
3
$5/2^-$
0.910
1
$3/2^-$
0.14
0.867
1
$1/2^-$
0.54
0.864
3
$7/2^-$
0.769
3
$5/2^-$
0
3
$^{65}_{30}Zn_{35} + (\Delta E_c - \delta)$
E_x
J^π
E_p^{LAB}
7.109
$5/2^+$
3.221
6.712
$3/2^-$
2.818
6.666
$1/2^-$
2.771
5.780
$^{65}_{31}Ga_{34}$
3.938
$^{64}_{30}Zn_{34} + p$

state. This resonance is the 9/2+ state at 1.066 MeV in the parent nucleus. The penetrability for l=4 was too small for this state to be observed in the present experiment. Calculations indicate that the effect of the 9/2+ state on the elastic cross section would have been comparable to a 5 to 10 eV 1/2+ resonance.

In the ^{66}Zn(p,p) experiment, the first and third excited states in the parent nucleus, ^{67}Zn, were observed as analog states in the daughter nucleus, ^{67}Ga. The energy level diagram for the isobaric pair, ^{67}Zn - ^{67}Ga, is shown in Figure 4.24. As in the case for Figure 4.23, the energy levels in the parent nucleus, ^{67}Zn, were shifted by $\Delta E_c - \delta$ in order to compare with the energy levels in the daughter nucleus, ^{67}Ga. The binding energy of the last proton in the parent nucleus is 5.271 MeV, and the analog state of the ground state in ^{67}Zn occurs at an excitation energy of 7.966 MeV in the daughter nucleus. Two of the three states observed in the (d,p) experiment were observed as analog states. The parent state at 0.185 MeV was too weak to be observed in this experiment. The 9/2+ state in the parent nucleus at 0.604 MeV was not observed since its expected laboratory energy was approximately 3.3 MeV, while the highest laboratory energy in the experiment was 3.26 MeV. In any event, the penetrability is so small that the analog of the 9/2+ resonance would probably have not been observed.

Figure 4.24 The ^{67}Zn - ^{67}Ga Isobaric Pair. Two of the three possible analog states were observed in this experiment.

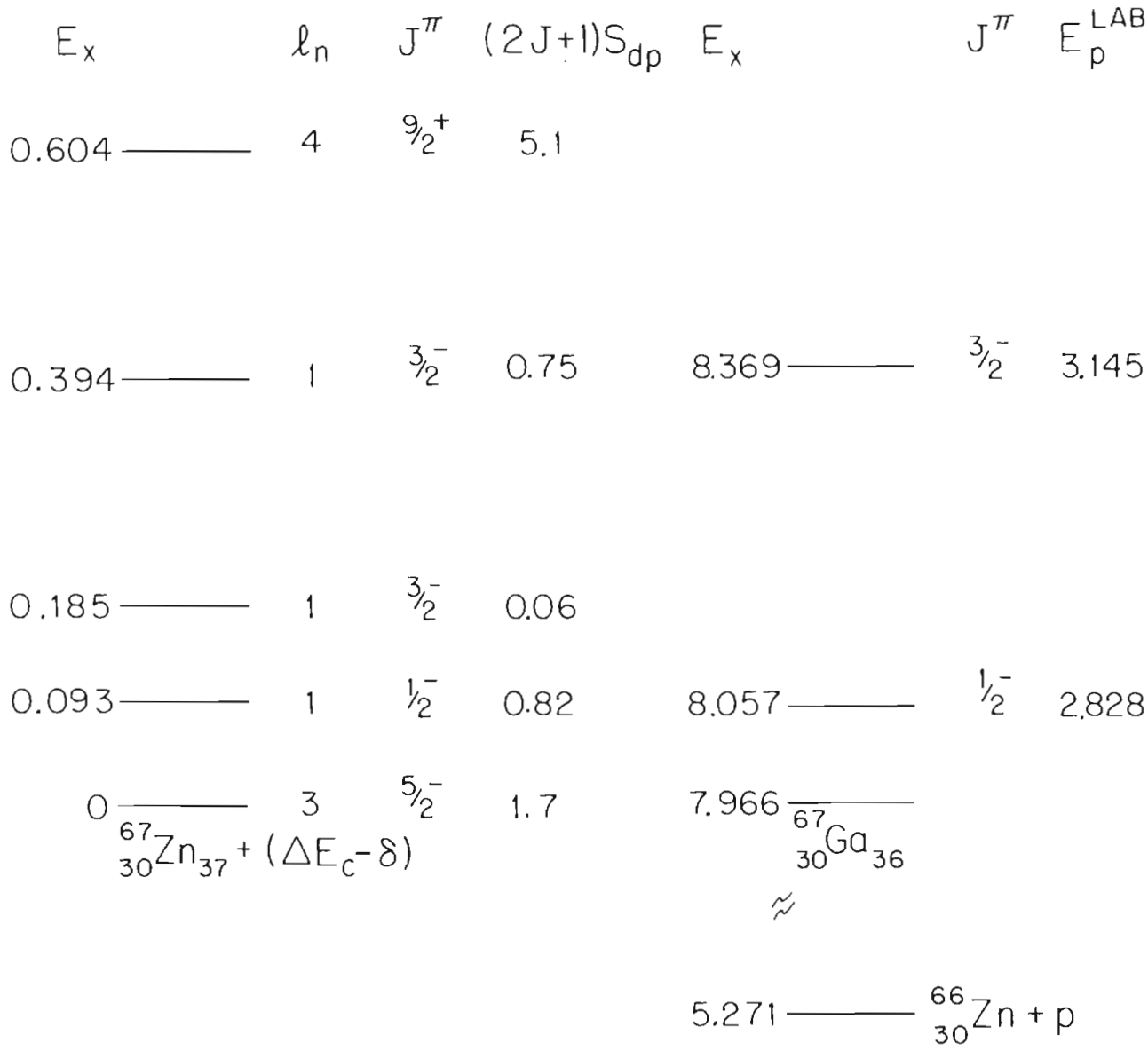
E_x
ℓ_n
J^π
$(2J+1)S_{dp}$
E_x
J^π
E_p^{LAB}
0.604
4
$9/2^+$
5.1
0.394
1
$3/2^-$
0.75
8.369
$3/2^-$
3.145
0.185
1
$3/2^-$
0.06
0.093
1
$1/2^-$
0.82
8.057
$1/2^-$
2.828
0
3
$5/2^-$
1.7
7.966
$^{67}_{30}Zn_{37} + (\Delta E_c - \delta)$
$^{67}_{30}Ga_{36}$
$\approx$
5.271
$^{66}_{30}Zn + p$

4.5.3 Coulomb Energies

The Coulomb energy differences between the parent and daughter states for the $^{64}Zn(p,p)$ reaction and for the $^{66}Zn(p,p)$ reaction are presented in Table 4.2. The Coulomb energy is calculated from

$$\Delta E_C = E_p^{cm} + B_n - E_X$$

where E_p^{cm} is the center of mass energy of the incident proton, B_n is the binding energy of the last neutron in the parent nucleus, and E_X is the excitation energy of the parent state. The error for the Coulomb energies is believed to be approximately 3 keV; since the error in B_n is approximately 1 keV, the error in E_X is less than 1 keV, and the error in E_p^{cm} is 2 to 3 keV. In both ^{65}Ga and ^{67}Ga, the analog states were fragmented. For ^{65}Ga, the $1/2^-$ analog state at 2.777 MeV was fragmented into three resonances. The $3/2^-$ analog state at 2.818 MeV and the $5/2^+$ analog state at 3.221 MeV were fragmented into only two resonances. Obviously, it was impossible to fit these analogs to the fine structure distribution formula in Section 4.5.1. Therefore, the centroid energy of each analog was calculated and used as the analog state energy.

Table 4.2 Coulomb Energy Differences

B_n (MeV)	E_x (MeV)	E_p (MeV)	J^π	ΔE_c (MeV)
^{65}Ga				
7.979	0.867	2.728	1/2−	9.840
	0.910	2.774	3/2−	9.843
	1.370	3.171	5/2+	9.780
^{67}Ga				
7.954	0.093	2.786	1/2−	9.746
	0.394	3.098	3/2−	9.759

The equation used to calculate the centroid energy is

$$\langle E \rangle = [\Sigma \gamma^2 E] / [\Sigma \gamma^2]$$

The average Coulomb energy for these three analogs is 9.821 MeV. This value agrees very well with the Coulomb energy of 9.856 MeV predicted by Jänecke's semi-empirical formula.

The fits to the fine structure distribution for the $1/2^-$ and $3/2^-$ analog states in ^{67}Ga determined the analog state energies. The average Coulomb energy for the two analog states is 9.753 MeV. Again, the experimental value for the Coulomb energy agrees with the value of 9.757 MeV predicted by Jänecke's formula.

4.5.4 Spectroscopic Factors

The spectroscopic factors (S_{pp}) for the analog states are calculated from

$$S_{pp} = [2T_o + 1] \Gamma_{pp} / \Gamma_{sp}$$

where T_o is the z-component of the isospin of the target nucleus, Γ_{pp} is the total observed width of the analog state, and Γ_{sp} is the single particle width of the state in the (proton plus target nucleus) system.

The total observed width of an analog state is the sum of the laboratory widths of the fragmented analog state. The single particle widths were calculated using a computer program, HANS, written by Harney(1969). The program calculates the single particle widths using three different methods: First, the R-Matrix method of Thompson, Adams, and Robson (TAR), second and third are the shell model methods of Zaidi, Darmodjo, and Harney (ZDH), and of Mekjian and McDonald (MM). References for these methods are in the article by Harney and Weidenmüller(1969).

The first step in the procedure is to vary the neutron well depth of an optical model potential until the correct binding energy of the parent state is obtained. The next step is to add to the neutron well depth a symmetry potential for the effect of the Coulomb force on the extra proton. Then the single particle widths are calculated using this new well depth. The radius and diffuseness parameters used in these calculations were $r = 1.25A^{1/3}$ F and a = 0.67 F, respectively. The error in the single particle widths due to uncertainties in the optical model parameters was estimated by Moses(1970) to be approximately 15%.

The spectroscopic factors for ^{65}Ga and ^{67}Ga, along with the (d,p) spectroscopic factors, are given in Table 4.3. The single particle widths used to calculate these

spectroscopic factors are presented in Table 4.4 along with the neutron and proton well depths.

The spectroscopic factor for the $5/2^+$ analog state in ^{65}Ga agrees with the (d,p) spectroscopic factor, while the remaining spectroscopic factors for ^{65}Ga and ^{67}Ga are lower than the (d,p) spectroscopic factors by approximately a factor of two. These results are consistent with past results obtained at this laboratory.

Table 4.3 Spectroscopic Factors

E_x (MeV)	E_p (MeV)	J^π	S_{TAR}	S_{ZDH}	S_{MM}	S_{dp}
^{65}Ga						
0.867	2.771	1/2−	0.17	0.12	0.12	0.27
0.910	2.818	3/2−	0.03	0.02	0.02	0.04
1.370	3.221	5/2+	0.16	0.14	0.14	0.17
^{67}Ga						
0.093	2.828	1/2−	0.24	0.18	0.18	0.41
0.394	3.145	3/2−	0.12	0.10	0.10	0.19

Table 4.4 Single Particle Widths

E_p (MeV)	J^π	U_n (MeV)	U_p (MeV)	$\Gamma_{sp}/(2T_o+1)$ (keV) TAR	ZDH	MM
^{65}Ga						
2.771	1/2−	-47.23	-49.67	2.18	2.93	2.96
2.818	3/2−	-44.18	-46.62	2.70	3.50	3.53
3.221	5/2+	-58.72	-61.16	2.29	2.57	2.60
^{67}Ga						
2.328	1/2−	-46.28	-49.59	2.21	2.90	2.93
3.145	3/2−	-43.19	-46.50	3.18	4.04	4.12

4.5.5 Fine Structure Distributions

The fine structure distributions of the analog states in ^{67}Ga were fit with the Lane fine structure distribution formula (see Section 4.5.1). The fine structure distributions of the analog states in ^{65}Ga were not fit since each of the analog states was fragmented into only two or three resonances. The fit to the cumulative sum of the reduced widths and the plot of the reduced widths for the $3/2^-$ analog state in ^{67}Ga are shown in Figure 4.25. This is a case of weak coupling between the analog state and the background states of the same spin and parity, even though 21 of the $3/2^-$ states were identified as fragments of this analog state. The sum of the reduced widths of these resonances (10.5 keV) agrees very well with the fit to the analog reduced width (10.6 keV). The spreading width, W_o, was compared with the prediction of Robson's model. According to Robson's model,

$$W_o = 2\pi s_o \gamma_A^2 (\Delta L_c)^2$$

where ΔL_c is the Robson level-shift factor. The value of ΔL_c was calculated to be 1.28. Using this value for ΔL_c and the values of s_o and γ_A^2 obtained from the fine structure fit, the value of W_o is 0.76 keV. This result

Figure 4.25 Theoretical Fit to the Fine Structure Distribution of the $3/2^-$ Analog State at 3.1452 MeV in ^{67}Ga. The histogram is the cumulative sum of reduced widths for the $3/2^-$ levels in the region. The solid line is the fit to the integral of the Lane fine structure distribution formula.

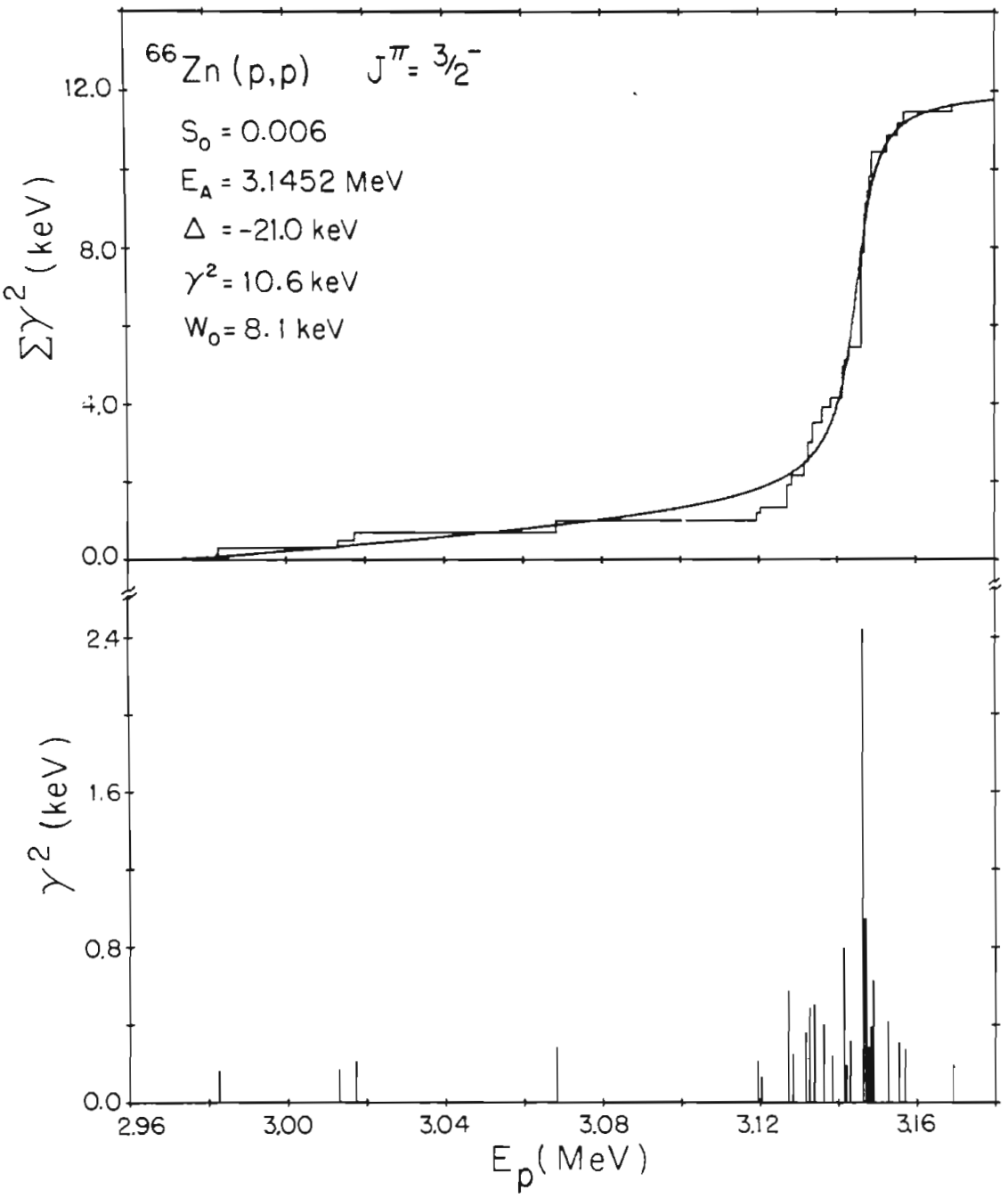
^{66}Zn (p,p) J^{π}= 3/2$^-$
S_0 = 0.006
E_A = 3.1452 MeV
Δ = -21.0 keV
γ^2 = 10.6 keV
W_0 = 8.1 keV
$\Sigma\gamma^2$ (keV)
12.0
8.0
4.0
0.0
γ^2 (keV)
2.4
1.6
0.8
0.0
2.96
3.00
3.04
3.08
3.12
3.16
E_p (MeV)

disgrees with the value of 8.1 keV obtained from the fine structure fit. For weak mixing W_o is probably not well determined by the fitting process.

The value of the asymmetry phase ϕ and the correlation measure r_c were also calculated and compared with Robson's model where,

$$\tan 2\phi = \frac{-\Delta W_o}{\frac{1}{4}(W_c^2 - W_o^2) + \Delta^2}$$

and

$$r_c = \frac{-2\Delta \tan\phi}{W_o}$$

The value of ϕ was calculated to be 0.05 with the value for r_c calculated to be 0.19. Robson's model predicts $r_c = 1$ (implying $\tan\phi = -W_o/2\Delta$ and $w_c = 0$). Past results for other analog states studied at this laboratory indicate that the values of ϕ range from 0.05 to 0.20 and that the value for r_c range from 0.10 to 1.0.

The fit to the cumulative sum of the reduced widths of the 1/2$^-$ analog state in ^{67}Ga is shown in Figure 4.26 along with the plot of the reduced widths. The fine structure distribution was fit with the background strength function (s_o) equal to zero. This value for the background strength function is reasonable since the 1/2$^-$ strength function in this mass region is very small. The asymmetry parameter was also set equal to zero since this parameter can not be determined if s_o is zero.

The analog state energy is believed to be determined to within 1 to 2 keV. The reduced width of the analog

Figure 4.26 Theoretical Fit to the Fine Structure Distribution of the $1/2^-$ Analog State at 2.828 MeV in ^{67}Ga. The histogram is the cumulative sum of reduced widths for the $1/2^-$ levels in the region. The solid line is the fit to the integral of the Lane fine structure distribution formula.

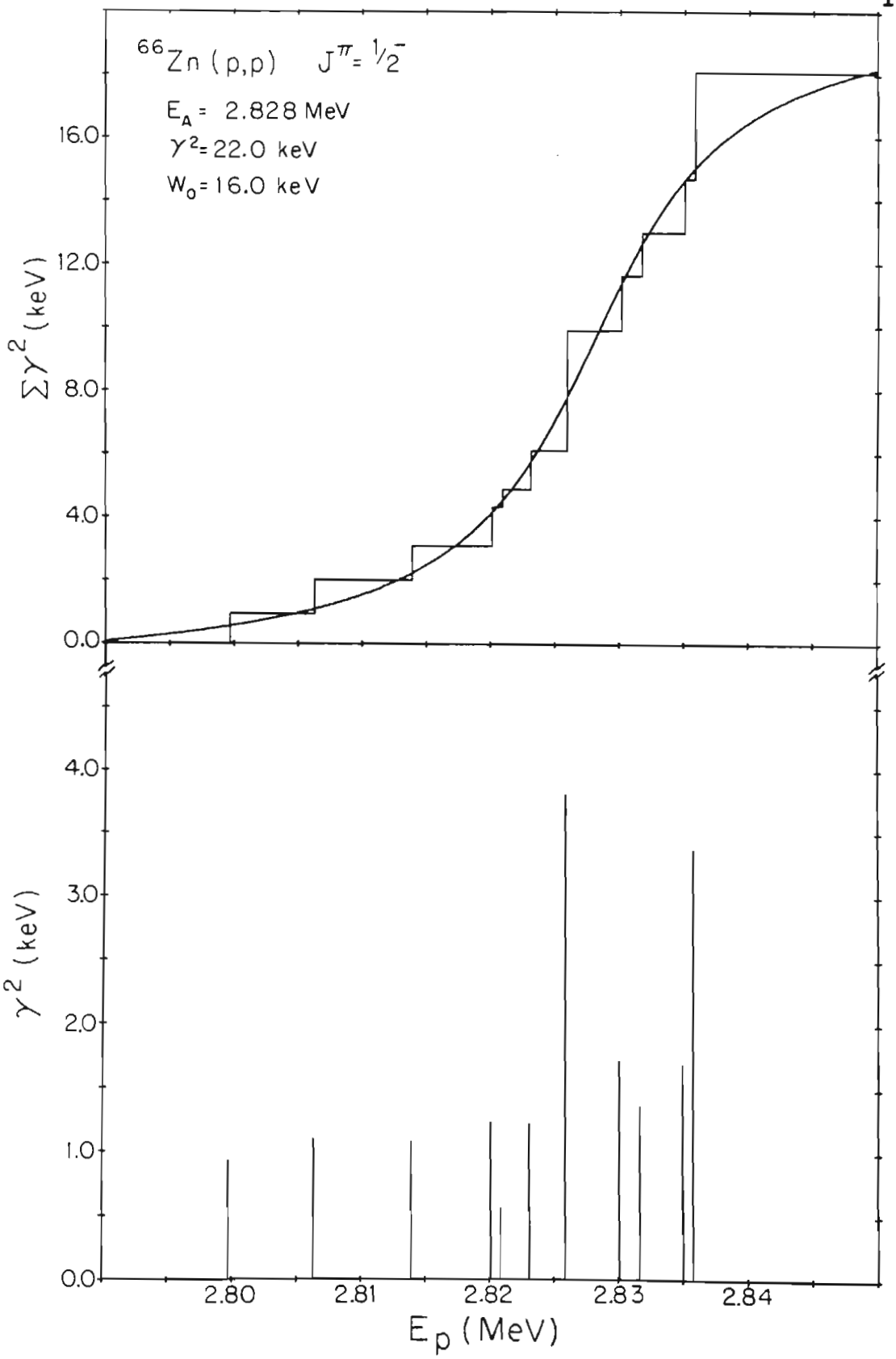
^{66}Zn (p,p) $J^{\pi} = 1/2^-$
E_A = 2.828 MeV
γ^2 = 22.0 keV
W_0 = 16.0 keV
$\Sigma\gamma^2$ (keV)
16.0
12.0
8.0
4.0
0.0
γ^2 (keV)
4.0
3.0
2.0
1.0
0.0
2.80
2.81
2.82
2.83
2.84
E_p (MeV)

state (22.0 keV) agrees fairly well with the sum of the observed reduced widths (18.1 keV). The spreading width, W_o, could not be compared with Robson's model since s_o was assumed to be zero.

Chapter 5

Summary

Excitation functions were measured for proton elastic scattering on ^{64}Zn and ^{66}Zn. The overall energy resolution was 420 to 525 eV for the ^{64}Zn reaction and 360 to 405 eV for the ^{66}Zn reaction. The resonances observed in these excitation functions were analyzed with R-Matrix theory. Spins, parities, elastic widths, and resonance energies were determined for 39 resonances in ^{65}Ga and 148 resonances in ^{67}Ga. The interpretation of these parameters was directed toward three areas: s-wave strength functions, statistical properties, and analog states.

The s-wave strength function was calculated and compared to results from (p,n) studies. The s-wave strength function shows an increase for A=66, which is consistent with earlier results from (p,n) cross section measurements.

The statistical properties of the 1/2$^+$ resonances in ^{65}Ga and ^{67}Ga were examined. The experimental spacing distributions and reduced width distributions of the data were compared with the theoretical distributions. Both

distributions show the effects of missing small resonances. Over the entire energy range, approximately 50% of the resonances were missed in ^{65}Ga, while approximately 70% of the resonances were missed in ^{67}Ga. Level densities of the 1/2$^+$ resonances in ^{65}Ga and ^{67}Ga were compared with predictions from the formula of Gilbert and Cameron. After the experimental level densities were corrected for missing small resonances, the corrected experimental values were in overall agreement with the theoretical values.

Five analog states were identified: three in ^{65}Ga and two in ^{67}Ga. The analog states in ^{67}Ga were highly fragmented, but the analog states in ^{65}Ga were split into only two or three resonances. Coulomb energies were determined for each analog state and were in agreement with Jänecke's semi-empirical formula. Spectroscopic factors were determined for the observed analog states and compared with the (d,p) spectroscopic factors. The analog spectroscopic factors were generally a factor of two smaller than the (d,p) spectroscopic factors.

Appendix 6.1

Resonance Parameters

The resonance parameters for ^{65}Ga and for ^{67}Ga are listed in Table 6.1 and Table 6.2, respectively. The resonance energies are the corrected laboratory energies. It is believed that the absolute energies have errors of no more than 2 or 3 keV, while the relative energies (between neighboring resonances) are believed to be accurate within 200 to 300 eV. The uncertainties in the laboratory widths and therefore the reduced widths are believed to be less than ±20% for resonances with laboratory width greater than 30 eV. The uncertainty for resonances below 30 eV is believed to be less than ±30%.

The resonances with l greater than zero were assigned total angular momentum values in the following manner: If the resonance was identified as a fragment of an analog state, then the resonance was assigned the total angular momentum value of the parent state. Otherwise, the resonance was fit with the higher value of total angular momentum, J = l + 1/2. The spin assignments have been listed following the convention:

1/2−	Definite spin and parity established
(1/2,3/2)−	Definite l-value determined, spin cannot be uniquely determined

Table 6.1 ^{65}Ga Resonance Parameters

	E_p (keV)	J^π	Γ_p (eV)	γ^2 (eV)
		l=0		
1	2561.8	1/2+	50	1907
2	2577.6	1/2+	35	1271
3	2626.2	1/2+	50	1569
4	2631.8	1/2+	30	926
5	2639.8	1/2+	25	754
6	2650.9	1/2+	25	730
7	2677.1	1/2+	30	812
8	2696.7	1/2+	60	1536
10	2749.0	1/2+	80	1772
11	2760.9	1/2+	80	1716
13	2780.4	1/2+	45	916
15	2791.6	1/2+	25	494
17	2818.6	1/2+	60	1105
19	2876.4	1/2+	70	1113
20	2905.4	1/2+	150	2221
21	2966.9	1/2+	70	895
22	3016.2	1/2+	90	1027
23	3039.9	1/2+	50	541
24	3046.3	1/2+	45	480
25	3057.2	1/2+	200	2082

Table 6.1 (continued)

	E_p (keV)	J^π	Γ_p (eV)	γ^2 (eV)
26	3070.9	1/2+	70	707
27	3074.2	1/2+	60	602
28	3095.8	1/2+	70	670
29	3123.4	1/2+	120	1082
30	3134.2	1/2+	300	2645
31	3156.1	1/2+	50	421
32	3170.6	1/2+	40	327
33	3177.1	1/2+	200	1613
34	3196.9	1/2+	50	388
35	3210.5	1/2+	50	377
38	3225.1	1/2+	110	806
39	3235.0	1/2+	60	431
	l=1			
9	2748.1	1/2-	50	2290
12	2772.6	1/2-	240	10260
14	2781.9	1/2-	70	2915
16	2815.4	3/2-	40	1518
18	2820.2	3/2-	40	1498
	l=2			
36	3220.3	5/2+	280	14550
37	3223.1	5/2+	90	4129

Table 6.2 ^{67}Ga Resonance Parameters

	E_p (keV)	J^π	Γ_p (eV)	γ^2 (eV)
		l=0		
1	2609.7	1/2+	20	627
2	2648.8	1/2+	60	1675
3	2663.8	1/2+	23	615
4	2665.4	1/2+	25	665
5	2671.3	1/2+	17	445
6	2679.1	1/2+	25	640
7	2690.5	1/2+	12	297
8	2694.2	1/2+	25	613
9	2709.8	1/2+	20	470
10	2711.5	1/2+	12	280
11	2713.2	1/2+	10	233
12	2720.0	1/2+	12	274
13	2738.5	1/2+	28	607
14	2760.6	1/2+	20	409
15	2762.5	1/2+	15	305
16	2780.7	1/2+	10	194
17	2782.6	1/2+	20	385
18	2799.0	1/2+	12	221
20	2804.8	1/2+	40	727
22	2812.6	1/2+	30	534

Table 6.2 (continued)

	E_p (keV)	J^π	Γ_p (eV)	γ^2 (eV)
24	2822.2	1/2+	17	295
28	2826.1	1/2+	22	378
34	2841.2	1/2+	35	579
35	2848.0	1/2+	25	407
36	2868.5	1/2+	20	309
37	2869.6	1/2+	40	616
38	2871.4	1/2+	20	307
39	2877.4	1/2+	25	378
40	2893.2	1/2+	40	581
41	2894.5	1/2+	10	145
42	2902.6	1/2+	45	639
44	2909.6	1/2+	10	140
45	2913.1	1/2+	85	1177
46	2925.9	1/2+	40	537
47	2934.3	1/2+	65	855
48	2936.5	1/2+	15	196
50	2946.5	1/2+	20	256
53	2957.1	1/2+	35	436
54	2957.6	1/2+	18	224
55	2959.3	1/2+	7	87
56	2963.5	1/2+	20	246

Table 6.2 (continued)

	E_p (keV)	J^π	Γ_p (eV)	γ^2 (eV)
57	2973.5	1/2+	50	600
58	2978.0	1/2+	22	261
59	2982.7	1/2+	15	176
60	2985.1	1/2+	45	525
63	2986.2	1/2+	13	151
64	3004.2	1/2+	25	279
65	3005.1	1/2+	13	145
66	3014.6	1/2+	22	240
68	3017.7	1/2+	35	380
70	3048.2	1/2+	30	304
71	3056.4	1/2+	35	348
72	3058.8	1/2+	50	495
73	3064.0	1/2+	25	245
74	3069.9	1/2+	20	193
76	3077.4	1/2+	50	475
77	3082.3	1/2+	30	282
78	3084.9	1/2+	40	374
79	3091.0	1/2+	8	74
80	3092.0	1/2+	8	74
81	3094.3	1/2+	45	412
82	3095.2	1/2+	35	320

Table 6.2 (continued)

	E_p (keV)	J^π	Γ_p (eV)	γ^2 (eV)
83	3103.2	1/2+	25	225
84	3106.0	1/2+	55	491
85	3109.0	1/2+	30	266
86	3110.9	1/2+	35	309
89	3126.9	1/2+	75	641
90	3128.9	1/2+	40	340
91	3130.3	1/2+	15	127
94	3134.0	1/2+	80	674
98	3137.9	1/2+	55	459
101	3144.3	1/2+	10	82
105	3148.0	1/2+	25	205
109	3151.2	1/2+	20	163
113	3153.6	1/2+	40	324
114	3154.0	1/2+	30	242
115	3154.4	1/2+	75	606
119	3162.7	1/2+	115	913
120	3166.9	1/2+	22	173
121	3172.4	1/2+	22	171
123	3182.0	1/2+	17	130
124	3182.5	1/2+	45	343
125	3186.3	1/2+	35	265

Table 6.2 (continued)

	E_p (keV)	J^π	Γ_p (eV)	γ^2 (eV)
126	3190.9	1/2+	75	562
128	3196.8	1/2+	45	333
130	3200.1	1/2+	18	132
131	3201.4	1/2+	10	73
132	3209.5	1/2+	28	202
133	3210.6	1/2+	40	288
134	3212.8	1/2+	30	215
135	3215.5	1/2+	75	535
136	3217.7	1/2+	60	426
137	3220.3	1/2+	30	212
138	3224.5	1/2+	60	421
140	3230.7	1/2+	15	104
142	3241.0	1/2+	15	102
143	3243.1	1/2+	15	101
144	3247.0	1/2+	80	537
145	3250.7	1/2+	15	100
146	3254.6	1/2+	30	198
147	3255.8	1/2+	45	297
148	3258.9	1/2+	85	557
		l=1		
19	2802.3	1/2−	25	931

Table 6.2 (continued)

	E_p (keV)	J^π	Γ_p (eV)	γ^2 (eV)
21	2809.0	1/2-	30	1097
23	2816.6	1/2-	30	1074
25	2822.8	1/2-	35	1232
26	2823.6	1/2-	16	562
27	2825.8	1/2-	35	1222
29	2828.6	1/2-	110	3812
30	2832.8	1/2-	50	1713
31	2834.4	1/2-	40	1365
32	2837.8	1/2-	50	1690
33	2838.6	1/2-	100	3374
43	2904.1	(1/2,3/2)-	7	199
49	2942.4	(1/2,3/2)-	8	206
51	2949.3	(1/2,3/2)-	10	253
52	2954.2	(1/2,3/2)-	9	225
61	2985.5	(1/2,3/2)-	7	162
62	2986.0	(1/2,3/2)-	7	162
67	3016.2	(1/2,3/2)-	8	172
69	3020.5	(1/2,3/2)-	10	213
75	3071.6	(1/2,3/2)-	15	283
87	3123.1	3/2-	13	218
88	3124.0	3/2-	8	134

Table 6.2 (continued)

	E_p (keV)	J^π	Γ_p (eV)	γ^2 (eV)
92	3130.8	3/2-	35	576
93	3132.1	3/2-	15	246
95	3135.2	3/2-	22	359
96	3136.2	3/2-	30	488
97	3137.4	3/2-	30	487
99	3139.9	3/2-	25	403
100	3142.0	3/2-	15	241
102	3145.0	3/2-	50	797
103	3145.7	3/2-	12	191
104	3146.7	3/2-	20	318
106	3149.9	3/2-	155	2445
107	3150.8	3/2-	60	945
108	3150.9	3/2-	20	315
110	3151.5	3/2-	18	283
111	3152.0	3/2-	25	393
112	3152.6	3/2-	40	627
116	3156.4	3/2-	27	420
117	3159.1	3/2-	20	309
118	3160.7	3/2-	18	277
122	3172.9	(1/2,3/2)-	13	195
127	3193.2	(1/2,3/2)-	8	115

Table 6.2 (continued)

	E_p (keV)	J^π	Γ_p (eV)	γ^2 (eV)
129	3198.5	(1/2,3/2)−	13	184
139	3229.7	(1/2,3/2)−	8	106
141	3238.9	(1/2,3/2)−	10	130

Appendix 6.2

Glow Discharge System

A glow discharge system was designed and built in order to clean the carbon backing used in the preparation of the ^{66}Zn targets. By cleaning the carbon backings before evaporation, the ^{66}Zn condensed onto the carbon without the carbon being cooled to very low temperatures. The targets prepared with the glow discharge technique exhibited less energy straggling and less point scatter than did the ^{66}Zn targets prepared with cooled carbon backings. As mentioned in Section 2.4, a possible explanation for the decreased energy straggling is that with the cleaner carbon backings, the ^{66}Zn made a stronger bond to the carbon, and reduced migration of the zinc into the carbon backings.

It is useful to review the basic properties of a glow discharge in order to understand the many factors involved in the design and construction of the system. A detailed description of glow discharge techniques is given by Holland(1966). The characteristics of a glow discharge at low pressure depends on several factors; the value of the gas pressure, the discharge path length and electrode

geometry, and the value of the applied voltage. If the pressure is in the region of 5 to 10 microns and the applied voltage is a few kilovolts, a glow discharge is obtained. In front of the cathode is a glow termed the cathode glow, followed by a dark space called the cathode dark space. The cathode dark space is followed by the negative glow, the Faraday dark space, and the positive column. In the cathode dark space, the gas in the system is ionized and therefore this region is essential for the maintenance of the discharge. The size of the cathode dark space can be controlled by the pressure and the applied voltage.

In the positive column, recombination is taking place which accounts for the brightness of this region. Since the ionized electrons and positive ions attain their highest velocity in the cathode dark space, this region is used for ionic bombardment cleaning. If the size of the cathode dark space is allowed to expand and contact the anode, the glow discharge will cease. This characteristic of a glow discharge can be used as an advantage for the design of the discharge electrodes. If the gap between two discharge electrodes is too small for sustained ionization, then the glow discharge may not cease if an alternative longer path is available. By using this phenomenon, one can easily fix the geometry of the electrodes such that the carbon backings are in the

cathode dark space.

Another criterion for the design of the discharge electrodes is the choice of material for the electrodes. Since aluminum has a lower sputtering rate than any other metal, aluminum is used for the discharge electrodes. Other materials may sputter and contaminate the carbon backings before evaporation.

The glow discharge system is shown schematically in Figure 6.1. The anode and cathode electrodes are aluminum rings 7.5" in diameter. The separation between the rings is approximately 1" with the separation between the bottom ring and the base of the bell jar approximately 6.75". The lower aluminum ring is the anode and is grounded to the base of the bell jar. The upper aluminum ring is the cathode and is connected to a power supply. The work holder containing the carbon backings was placed 1" to 2" above the upper ring and was not grounded. By having the two electrodes separated by only 1", a glow discharge could not be sustained in the region between the two rings. Therefore, the glow discharge followed the longer alternative path with the cathode dark space above the upper electrode and the positive column under the lower electrode. By using this geometry, the work holder is located in the cathode dark space. The power supply was manufactured by Universal Voltronics Corp. and has an output of 0 - 10 kV and 0 - 30 mA. A current limiting

Figure 6.1 Schematic of Glow Discharge System.

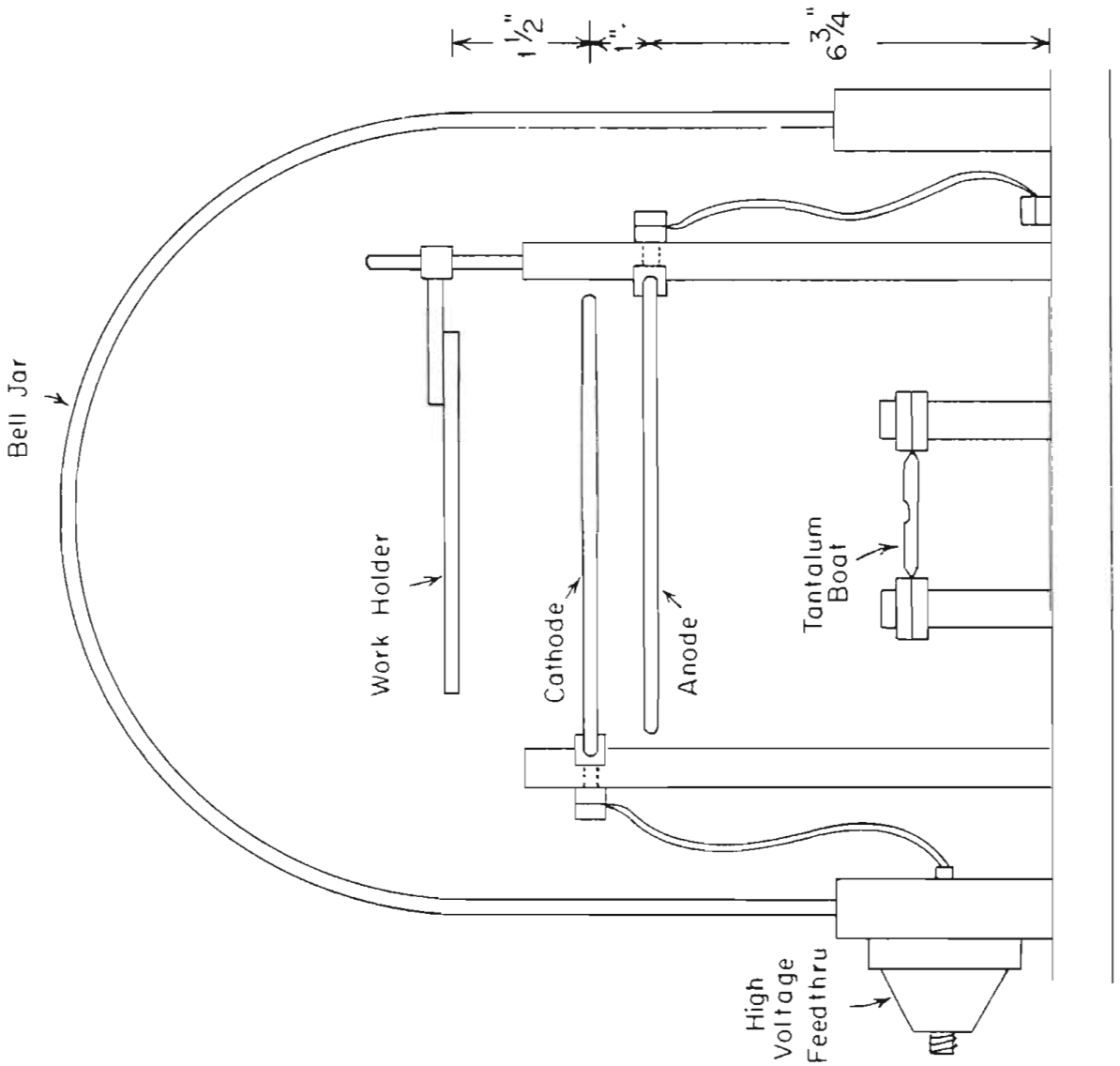
1 1/2"
1"
3/4"
Bell Jar
Work Holder
Cathode
Anode
Tantalum Boat
High Voltage Feedthru

resistor was placed in series with the power supply and the cathode electrode. The power supply was also grounded to the bell jar.

Under normal operating conditions, the power supply voltage was 7 to 8 kV and the output current was 15 to 20 mA. The voltage drop across the electrodes was usually 2 to 3 kV. Therefore, the voltage across the resistor was between 4 and 6 kV. The value of the resistor was 300,000 ohms and was rated for 120 watts. Therefore, it was necessary to limit the voltage drop across the resistor to below 6 kV. A pressure of 5 to 10 microns was maintained in the bell jar during operation by using a needle value to bleed in air. The glow discharge displayed the characteristic reddish color of a glow discharge operated in a partial vacuum.

A liquid nitrogen trap between the diffusion pump and the bell jar was filled before glow discharging in order to obtain a good vacuum upon completion of the glow discharge. Normally, the evaporation process should occur immediately after cleaning the carbon backings since the carbon backing will very quickly become contaminated from pump oil vapors. This contamination is an additional reason for filling the liquid nitrogen trap since a large fraction of the pump oil vapors are removed by the cold trap. However, for the fabrication of the ^{66}Zn targets, the carbon backings were very warm after the glow

discharge and the evaporation was delayed for a few minutes in order for some of the heat to radiate from the backings.

With this glow discharge system, much better targets were obtained for the ^{66}Zn experiment than for the ^{64}Zn experiment. The targets also led to better energy resolution, as is described in Section 2.4. This process can easily be used for the preparation of targets in future experiments in which a clean backing is desired.

BIBLIOGRAPHY

Anderson, J.D. and C. Wong, "Evidence for Charge Independence in Medium Weight Nuclei," Phys. Rev. Letters, Vol. 7, (1961), p. 250.

Barschall, H.H., "Regularities in the Total Cross Section for Fast Neutrons," Phys. Rev., Vol. 86, No. 3, (1952), p. 431.

Bethe, H.A., "Theory of Disintegration of Nuclei by Neutrons," Phys. Rev., Vol. 47, (1935), p. 747.

Bilpuch, E.G., Proceeding of the Conference on Isobaric Spin in Nuclear Physics, Tallahassee, Florida, March 17-19, 1966, (Academic, New York, 1966), p. 235.

Bilpuch, E.G., A.M. Lane, G.E. Mitchell, and J.D. Moses, "Fine Structure of Analogue States," Phys. Reports, Vol. 28c, (1976), p. 145.

Bilpuch, E.G., N.H. Prochnow, R.Y. Cusson, H.W. Newson, and G.E. Mitchell, "Statistical Properties of ^{49}V via Proton Resonance Reactions," Phys. Lett., Vol. 35B, No. 4, (1971), p. 303.

Blatt, J.M. and L.C. Biedenharn, "The Angular Distribution of Scattering and Reaction Cross Sections," Rev. Mod. Phys., Vol. 24, No. 4, (1952), p. 258.

Blatt, John M. and Victor F. Weiskopf, Theoretical Nuclear Physics (John Wiley and Sons, New York, 1952).

Block, R., R.E. Pixley, W. Reichart, and F. Zamboni,

"Improved Energy Resolution of Van de Graaff Accelerators," Nucl. Instr. and Meth., Vol. 59, (1968), p. 325.

Browne, J.C., Fine Structure of Analogue States in ^{61}Cu, ^{63}Cu and ^{65}Cu (Unpublished Ph.D. dissertation, 1969, Duke University, Durham, N.C., Department of Physics; University Microfilms, Ann Arbor, Michigan).

Chandler, John R., Channel Spin Mixing Ratios in High Resolution Proton - Inelastic Scattering on ^{46}Ti (Unpublished Ph.D. dissertation, 1978, North Carolina State University, Raleigh, N.C., Department of Physics; University Microfilms, Ann Arbor, Michigan).

Fallieros, S.J., "Shell-Model Description of Nuclear Analog States," Franklin Inst., Vol. 281, No. 3, (1966), p. 179.

Feshbach, H., C.E. Porter, and V.F. Weisskopf, "Model for Nuclear Reactions with Neutrons," Phys. Rev., Vol. 96, No. 2, (1954), p. 448.

Fox, J.D., C.F. Moore, and D. Robson, "Excitation of Isobaric Analog States in ^{89}Y and ^{90}Zr," Phys. Rev. Letters, Vol. 12, (1964), p. 198.

Gilbert, A., and A.G.W. Cameron, "A Composite Nuclear-Level Density Formula with Shell Corrections," Can. J. Phys., Vol. 43, (1965), p. 1446.

Harney, H. and H.A. Weidenmuller, "Spectroscopic Factors from Analogue Resonances," Nucl. Phys., Vol. A139, (1969), p. 241.

Harney, H.L., unpublished computer code (1969).

Holland, L., Vacuum Deposition of Thin Films (Chapman and Hall Ltd., London, 1966).

Jänecke, J. Isospin in Nuclear Physics, ed. D.H. Wilkinson (North-Holland, Amsterdam, 1967), p. 297.

Johnson, C.H., A. Galonsky, and J.P. Ulrich, "Proton Strength Functions from (p,n) Cross Sections," Phys. Rev., Vol. 109, No. 4, (1958), p. 1243.

Jones, G.A., "Energy Dependence of the (p,n) Reaction Near A = 70," Nucl. Phys., Vol. 12, (1959), p. 167.

Keyworth, G.A., A High Resolution Study of Isobaric Analogue States in ^{41}K and ^{23}Na (Unpublished Ph.D. dissertation, 1968, Duke University, Durham, N.C., Department of Physics; University Microfilms, Ann Arbor, Michigan).

Keyworth, G.A., G.C. Kyker Jr., E.G. Bilpuch, and H.W. Newson, "Fine Structure of Isobaric Analogue Resonances in ^{41}K," Phys. Letters, Vol. 20, No. 3, (1966) p. 281.

Keyworth, G.A., G.C. Kyker, Jr., E.G. Bilpuch and H.W. Newson, "A High-Resolution Study of Isobaric Analogue Resonances in ^{41}K," Nucl. Phys., Vol. 8, (1966), p. 590.

Lane, A.M. Isospin in Nuclear Physics, ed. D.H. Wilkinson, (North-Holland, Amsterdam, 1969) p. 509.

Lane, A.M., J.E. Lynn, and J.D. Moses, "Line Shape in Weak and Intermediate Coupling: Theory and Practical Fitting Procedures," Nucl. Phys., Vol. A232, (1974), p. 189.

Lane, A.M. and R.G. Thomas, "R-Matrix Theory of Nuclear Reactions," Rev. Mod. Phys., Vol. 30, No. 2, (1958), p. 257.

Lane, A.M., R.G. Thomas, and E.P. Wigner, "Giant Resonance Interpretation of the Nucleon-Nucleus Interaction," Phys. Rev., Vol. 98, (1955), p. 693.

Lynn, J.E. The Theory of Neutron Resonance Reactions, (Oxford, London, 1968).

Mahaux, C., and H.A. Weidenmüller, Shell Model Approach to Nuclear Reactions (North-Holland, Amsterdam, 1969).

Margolis, B. and V.F. Weisskopf, "Proton-Width Strength Function," Phys. Rev., Vol. 107, (1957), p. 641.

Mekjian, A. and W.M. MacDonald, "Analog State Resonances," Nucl. Phys., Vol. A121, (1968), p. 385.

Mello, P.A., "The Problem of External Mixing in Isobaric Analog Resonances," Ann. Phys., Vol. 45, (1967), p. 240.

Miller, D.W., R.E.Fields, and C.K. Bockelman, "Total Cross Section of Heavy Nuclei for Fast Neutrons," Phys. Rev., Vol. 85, (1952), p. 704.

Moses, J.D., A High-Resolution Study of Isobaric Analogue Resonances in ^{51}Mn, ^{53}Mn, and ^{55}Mn (Unpublished Ph.D. dissertation, 1969, Duke University, Durham, N.C., Department of Physics; University Microfilms, Ann Arbor, Michigan).

Cutlaw, D.A., A High-Resolution Study of Proton Resonances in ^{31}P, ^{35}Cl, and ^{93}Tc (Unpublished Ph.D. dissertation, 1974, North Carolina State University, Raleigh, N.C., Department of Physics; University Microfilms, Ann Arbor, Michigan).

De Toledo Piza, A.F.R. and A.K.Kerman, "Studies in Isobaric Analog Resonances. I. Gross Properties," Ann. Phys., Vol. 43, (1967), p. 363.

De Toledo Piza, A.F.R. and A.K. Kerman, "Studies in Isobaric Analog Resonances. II. Fine Structure," Ann. Phys., Vol. 48, (1968), p. 173.

Porter, C.E. and R.G. Thomas, "Fluctuations of Nuclear Reaction Widths," Phys. Rev., Vol. 104, No. 2, (1956), p. 483.

Richard, P., C.F. Moore, D. Robson, and J.D. Fox, "Observations of Fine Structure in Isobaric Analog Resonances," Phys. Rev. Letters, Vol. 13, No. 11, (1964), p. 343a.

Robson, D., "Theory of Isobaric-Spin Analogue Resonances," Phys. Rev., Vol. 137, No. 3B, (1965), p. B535.

Schiffer, J.P. and L.L. Lee, Jr., "Proton Strength

Functions from (p,n) Reaction Cross Sections," Phys. Rev., Vol. 109, No. 6, (1958), p. 2098.

Stephen, F.O., "A Theory of Isobaric Spin Analogue Resonances," Nucl. Phys., Vol. A94, (1967), p. 192.

Wells, W.K., High Resolution Proton Inelastic Scattering on ^{56}Fe and ^{48}Ti (Unpublished Ph.D. dissertation, 1978, Duke University, Durham, N.C., Department of Physics; University Microfilms, Ann Arbor, Michigan).

Westerfeldt, C.R., A High Resolution Study of Proton Resonances in ^{29}Al (Unpublished Master's thesis, 1977, North Carolina State University, Raleigh, N.C., Department of Physics; University Microfilms, Ann Arbor, Michigan).

Westerfeldt, C.R., unpublished computer code (1977).

Wigner, E.P. and L. Eisenbud, "Higher Angular Momenta and Long Range Interaction in Resonance Reactions," Phys. Rev., Vol. 72, No. 1, (1947), p. 29.

Wilkinson, D.H., Isospin in Nuclear Physics, ed. D.H. Wilkinson, (North-Holland, Amsterdam, 1969).

Wimpey, F.J., Electromagnetic Decay of Fragmented Analogue States in ^{45}Sc and ^{63}Cu (Unpublished Ph.D. dissertation, 1974, North Carolina State University, Raleigh, N.C., Department of Physics; University Microfilms, Ann Arbor, Michigan).